Peer Reviewed

Title:
Diagnosing, Optimizing and Designing Ni & Mn based Layered Oxides as Cathode Materials for Next Generation Li-ion Batteries and Na-ion Batteries

Author:
Liu, Haodong

Acceptance Date:
2016

Series:
UC San Diego Electronic Theses and Dissertations

Degree:
Ph.D., NanoEngineeringUC San Diego

Advisor(s):
Ying Shirley, Meng

Committee:
Liu, Ping, Luo, Jian, Sinha, Sunil K., Chen, Renkun

Permalink:
http://escholarship.org/uc/item/7836h0wg

Abstract:

Copyright Information:

UNIVERSITY OF CALIFORNIA, SAN DIEGO

Diagnosing, Optimizing and Designing Ni & Mn based Layered Oxides as
Cathode Materials for Next Generation Li-ion Batteries and Na-ion Batteries

A dissertation submitted in partial satisfaction of the
requirements for the degree Doctor of Philosophy

in

NanoEngineering

by

Haodong Liu

Committee in charge:

    Professor Ying Shirley Meng, Chair
    Professor Renkun Chen
    Professor Ping Liu
    Professor Jian Luo
    Professor Sunil K. Sinha

2016

The Dissertation of Haodong Liu is approved, and it is acceptable in quality and form for publication on microfilm and electronically:

_____

_____

_____

_____

_____

Chair

University of California, San Diego

2016

DEDICATION

To Zheng Liu, Qi shen and Miao Che

TABLE OF CONTENTS

LIST OF FIGURES

LIST OF TABLES

ACKNOWLEDGEMENTS

For the last but not least, my deepest gratitude goes to my parents Zheng Liu and Qi Shen for their love, patience and never-ending support. I specially thank to my wife, Miao Che, for her endless support and encouragement during my Ph.D.

Chapter 1, in part, is a reprint of the material "Performance and design considerations for lithium excess layered oxide positive electrode materials for lithium ion batteries" as it appears in the Energy & Environmental Science, Sunny Hy, Haodong Liu, Minghao Zhang, Danna Qian, Bing-Joe Hwang and Ying Shirley Meng, 2016, 9, 1931-1954. The dissertation author was the co-author of this paper. The author wrote the challenges for high energy density part. Chapter 1, in part, is a reprint of the material "Lithium and sodium containing cathodes/electrochemical cells" as it appears in the US patent, Ying Shirley Meng, and Haodong Liu, 2015, WO2015035138. The dissertation author was the primary investigator and inventor of this patent. The author wrote the whole patent.

Chapter 3, in part, is a reprint of the material "In-situ neutron diffraction study of the $xLi_2MnO_3 \cdot (1-x)LiMO_2$ (x= 0, 0.5; M= Ni, Mn, Co) layered oxide

compounds during electrochemical cycling" as it appears in the Journal of Power Sources, Haodong Liu, Christopher R. Fell, Ke An, Lu Cai, Ying Shirley Meng, Journal of Power Sources, 2013, 240, 772. The dissertation author was the primary investigator and author of this paper. All experiments and data analysis were performed by the author except for the *ex-situ* neutron powder diffraction data collection.

Chapter 4, in part, is a reprint of the material "Operando Lithium Dynamics in the Li-Rich Layered Oxide Cathode Material via Neutron Diffraction" as it appears in the Advanded Energy Materials, Haodong Liu, Yan Chen, Sunny Hy, Ke An, Subramanian Venkatachalam, Danna Qian, Minghao Zhang, Ying Shirley Meng, Advanded Energy Materials, 2016, 1502143. The dissertation author was the primary investigator and author of this paper. All experiments and data analysis were performed by the author except for the material preparation and cell making.

Chapter 5, in part, is a reprint of the material "Understanding the Role of NH_4F and Al_2O_3 Surface Co-Modification on Lithium-excess Layered Oxide $Li_{1.2}Ni_{0.2}Mn_{0.6}O_2$" as it appears in the ACS Applied Materials & Interfaces, Haodong Liu, Danna Qian, Mike G. Verde, Minghao Zhang, Loïc Baggetto, Ke An, Yan Chen, Kyler J. Carroll, Derek Lau, Miaofang Chi, Gabriel M. Veith, Ying Shirley Meng, ACS Applied Materials & Interfaces, 2015, 7 (44), 24791. The dissertation author was the primary investigator and author of this paper. All experiments and data analysis were performed by the author except for the TEM and STEM-EELS part.

Chapter 6, in full, is a reprint of the material "Enhancing the Electrochemical Performance of Lithium-Excess Layered Oxide $Li_{1.13}Ni_{0.3}Mn_{0.57}O_2$ via a Facile Nanoscale Surface Modification" as it appears in the Journal of the Electrochemical Society, Haodong Liu, Jiajia Huang, Danna Qian, Sunny Hy, Chengcheng Fang, Jian Luo, and Ying Shirley Meng, Journal of the Electrochemical Society, 2016, 163 (6), A971. The dissertation author was the primary investigator and author of this paper. All experiments and data analysis were performed by the author except for the TEM part.

Chapter 7, in part, is a reprint of the material "A new O3-type layered oxide cathode with high energy / power density for rechargeable Na batteries" as it appears in the Chemical Communications, Haodong Liu, Jing Xu, Chuze Ma, Ying Shirley Meng, Chemical Communications, 2015, 51,4693. The dissertation author was the primary investigator and author of this paper. All experiments and data analysis were performed by the author except for the XAS part, SXRD data collection, and SnS_2/rGO anode preparation.

Chapter 8, in full, is a reprint of the material "Exploring Li substituted O3-structured layered oxides $NaLi_xNi_{1/3-x}Mn_{1/3+x}Co_{1/3-x}O_2$ (x= 0.07, 0.13, and 0.2) as promising cathode materials for rechargeable Na batteries" as it appears in the Electrochemistry Communications, Jing Xu, Haodong Liu, and Ying Shirley Meng, Electrochemistry Communications, 2015, 60, 13. The dissertation author was the co-primary investigator and co-author of this paper. All experiments and data analysis were performed by the author except for the XAS part, and SXRD data collection.

VITA

2011	B.S.	Xiamen University, People's Republic of China
2014	M.S.	University of California, San Diego, USA
2016	Ph.D.	University of California, San Diego, USA

PUBLICATIONS

1. S. Hy, **H.D. Liu**, M. Zhang, D. Qian, B.J. Hwang, Y.S. Meng, "Performance and Design Considerations For The lithium Excess Layered Oxide Positive Electrode Materials for Lithium Ion Batteries", Energy & Environmental Science, 2016, 9, 1931.

2. **H.D. Liu**, J. Huang, D. Qian, S. Hy, C. Fang, J. Luo, and Y.S. Meng, "Enhancing the Electrochemical Performance of Lithium-Excess Layered Oxide $Li_{1.13}Ni_{0.3}Mn_{0.57}O_2$ via a Facile Nanoscale Surface Modification", Journal of The Electrochemical Society, 2016, 163 (6), A971.

3. **H.D. Liu**, Y. Chen, S. Hy, K. An, S. Venkatachalam, D. Qian, M. Zhang , and Y. S. Meng, "Operando Lithium Dynamics in the Li-Rich Layered Oxide Cathode Material via Neutron Diffraction", Advanced Energy Materials. 2016, 1502143.

4. **H.D. Liu**, D. Qian, M. G. Verde, M. Zhang, L. Baggetto, K. An, Y. Chen, K. J. Carroll, D. Lau, M. Chi, G. M. Veith, and Y. S. Meng. "Understanding the Role of NH_4F and Al_2O_3 Surface Co-modification on Lithium-Excess Layered Oxide $Li_{1.2}Ni_{0.2}Mn_{0.6}O_2$", ACS Applied Materials & Interfaces, 2015, 7 (34), 19189.

5. J. Xu, **H. D. Liu**, Y. S. Meng, "Exploring Li Substituted O3-structured Layered Oxides $NaLi_xNi_{1/3-x}Mn_{1/3+x}Co_{1-3/x}O_2$ (x = 0.07, 0.13, and 0.2) as Promising Cathode Materials for Rechargeable Na Batteries", Electrochemistry Communications, 2015, 60, 13. **(Equally contributed first authors)**

6. **H. D. Liu**, J. Xu, C. Ma and Y. S. Meng, "A New O3-type Layered Oxide Cathode with High Energy/Power Density for Rechargeable Na Batteries", Chemical Communications, 2015, 51, 4693. **(Equally contributed first authors)**

7. M. G. Verde, **H. D. Liu**, K. J. Carroll, L. Baggetto, G. M. Veith, and Y. S. Meng, "Effect of Morphology and Manganese Valence on the Voltage Fade and Capacity Retention of $Li[Li_{2/12}Ni_{3/12}Mn_{7/12}]O_2$", ACS Applied Materials & Interfaces, 2014, 6, 18868.

8. **H. D. Liu**, C. R. Fell, K. An, L. Cai**,** Y. S. Meng, "In-situ Neutron Diffraction Study of the $xLi_2MnO_3.(1-x)LiMO_2$", Journal of Power Sources, 2013, 240, 772

9. H. Yue, W. Zhang, **H.D. Liu**, Z. Liu, G. Zhong, Y. Yang, "Synthesis and Characterization of Fluorinated Carbon Nanotubes for Lithium Primary Batteries with High Power Density", Nanotechnology, 2013, 24, 424003

10. Y. S. Meng, **H.D. Liu**, "LITHIUM AND SODIUM CONTAINING CATHODES / ELECTROCHEMICAL CELLS", 2015, Patent No. WO2015035138

ABSTRACT OF THE DISSERTATION

Diagnosing, Optimizing and Designing Ni & Mn based Layered Oxides as
Cathode Materials for Next Generation Li-ion Batteries and Na-ion Batteries

by

Haodong Liu

Doctor of Philosophy in NanoEngineering

University of California, San Diego, 2016

Professor Ying Shirley Meng, Chair

The progressive advancements in communication and transportation has changed human daily life to a great extent. While important advancements in battery technology has come since its first demonstration, the high energy demands needed to electrify the automotive industry have not yet been met with the current technology. One considerable bottleneck is the cathode energy density, the Li-rich layered oxide compounds $xLi_2MnO_3.(1-x)LiMO_2$ (M= Ni, Mn, Co) ($0.5 =<x=< 1.0$) are possible cathode material, which exhibit reversible

discharge capacities greater than 280 mAh g^{-1} (almost twice the practical capacity of LiCoO$_2$).

In this work, neutron diffraction under *operando* battery cycling is developed to study the lithium and oxygen dynamics of Li-rich compounds that exhibits oxygen activation at high voltage. The measured lattice parameter changes and oxygen position show movement of oxygen and lattice contractions during the high voltage plateau until the end of charge. Lithium migration kinetics for the Li-rich material is observed under *operando* conditions for the first time to reveal the rate of lithium extraction from the lithium layer and transition metal layer are related to the different charge and discharge characteristics.

In the second part, a combination of multi-modality surface sensitive tools was applied in an attempt to obtain a complete picture to understand the role of NH$_4$F and Al$_2$O$_3$ surface co-modification on Li-rich. The enhanced discharge capacity of the modified material can be primary assigned to three aspects: decreased irreversible oxygen loss, the activation of cathode material was facilitated with pre-activated Mn^{3+} on the surface, and stabilization of the Ni redox pair. These insights will provide guidance for the surface modification in high voltage cathode battery materials of the future.

In the last part, the idea of Li-rich has transferred to the Na-ion battery cathode. A new O3 - Na$_{0.78}$Li$_{0.18}$Ni$_{0.25}$Mn$_{0.583}$O$_w$ is prepared as the cathode material for Na-ion batteries, delivering exceptionally high energy density and superior rate performance. The single-slope voltage profile and ex situ synchrotron X-ray diffraction data demonstrate that no phase transformation

happens through a wide range of sodium concentrations (0.8 Na removed). Further optimization could be realized by tuning the combination and ratio of transition metals.

Chapter 1. Introduction

1.1. The motivation and outline

The role of energy storage is becoming more and more significant as a result of modern civilization. The depletion of fossil fuels and pressure from environmental pollution promote the increasing use of renewable energy sources, such as wind and solar. On the other hand, to develop a battery with much improved energy density or decrease the cost of battery technology is of essential importance to the society. [1]

Li-ion batteries, are the most popular rechargeable batteries, which are installed in almost all portable electronic devices. The major features of Li-ion batteries includes: Li is the lightest metallic element; and Li has a very low redox potential ($E^{\ominus}Li^+/Li$ = -3.04 V versus standard hydrogen electrode). These two factors contribute to cells with high voltage and high energy density.[2] Recently, Li-ion batteries have become the power sources of the next generation electric vehicles and plug-in electric vehicles. Compare to the mobile phones, the electric vehicles could be treated as bigger portable devices. No matter the size of a portable device, the energy density of a battery is one of the key features to master the market. The bottleneck of a Li-ion battery which limits its energy density is the energy density of the cathode material. Therefore, a better cathode material which possesses much higher energy density plays a significant role in increasing the energy density of Li-ion batteries.[3]

In regard of another energy storage application, the large scale stationary storage cares the cost of the battery. Owing to the high abundance of Na (sodium) sources, the Na chemistry could either mitigate the feasible shortage of Li or reduce the cost of. The redox potential of $Na^+/ Na = -2.71$ V , which is only 0.3 V above that of Li. Consequently, rechargeable Na-ion batteries become more promising for large scale stationary energy storage.[4]

Most studies and characterizations in the reported literatures are based on the coin cells, which only look at small amount of materials. Benefits from the deep penetration of neutron, we are able to investigate the behavior of all the components in a real battery without disassemble the cell.[5] The *operando* neutron diffraction technique allows real time observation of the structure evolution of electrode materials, which is also a nondestructive measurement. The *operando* neutron diffraction is relatively new and not widely used in the battery related research.

Therefore, the objective of my Ph.D. thesis is divided into three parts. The first part is to develop the *operando* neutron diffraction technique, which is very powerful to investigate the structural changes and Li dynamics of cathode materials during battery charge/discharge cycling. The objective of the second part focuses on modifying the surface of Li-rich, and understanding the roles of each surface modification strategy on the enhanced performance. In the last part, a series of new layered oxide cathodes are explored for Na-ion batteries, which deliver high energy density and maintain stable structure during electrochemical cycling.

Chapter 1 gives a general introduction of Li-ion batteries, Li-rich (Li-excess) layered oxide cathode materials, and Na-ion batteries. **Chapter 2** briefly introduces advanced characterization tool I use in my research which is *operando* neutron scattering. **Chapter 3** is the first *in-situ* neutron diffraction study of the Li-rich ($Li_{1.2}Ni_{0.18}Mn_{0.53}Co_{0.1}O_2$) layered oxide and NMC ($LiNi_{1/3}Mn_{1/3}Co_{1/3}O_2$) layered oxide compounds during electrochemical cycling. Irreversible structural change of Li-rich during first charge/discharge cycle is indicated by dynamic changes in lattice d-spacing, while the NMC shows completely reversible structural evolution. **Chapter 4** investigates the Li and oxygen dynamics of high Li-rich ($Li(Li_{x/3}Ni_{(3/8-3x/8)}Co_{(1/4-x/4)}Mn_{(3/8+7x/24)}O_2$, x = 0.6) and low Li-rich ($Li(Li_{x/3}Ni_{(1/3-x/3)}Co_{(1/3-x/3)}Mn_{(1/3+x/3)}O_2$, x = 0.24) compounds that exhibit different degrees of oxygen activation at high voltage via neutron diffraction under *operando* battery cycling. It is revealed for the first time that Li migration rates at different sites are highly dependent on the different voltage regions that exhibit different battery characteristics. In **chapter 5**, the surface of Li-rich ($Li_{1.2}Ni_{0.2}Mn_{0.6}O_2$) is modified by NH_4F and Al_2O_3. The changes of surface structure and chemistry of modified Li-rich are discussed. The enhanced discharge capacity after surface modification is explored. **Chapter 6** develops a facile nanoscale surface modification on Li-rich. The nanoscale Li_3PO_4 surface modification can be easily achieved by ballmilling and isothermal annealing. This work provides a facile and scalable surface modification method to improve electrochemical performance of cathode materials for lithium ion batteries. In **Chapter 7,** the idea of high capacity Li-rich is transferred to O3 type Na transition

metal oxide compounds and it is proved that the high capacity Na transition metal oxide compounds without phase transformations could be achieved. In **Chapter 8,** a series of new O3 cathode materials, $NaLi_xNi_{1/3-x}Mn_{1/3+x}Co_{1/3-x}O_2$ (x = 0.07, 0.13, and 0.2), are explored by substituting Li in the layered structure. The optimized composition, $NaLi_{0.07}Ni_{0.26}Mn_{0.4}Co_{0.26}O_2$, demonstrates good capacity retention and excellent rate performance. The structure change and charge compensation mechanism have been studied. **Chapter 9** summarizes the work in this thesis and proposes the research plan for the future study.

1.2. The configuration and working mechanism of the Li-ion battery

Figure 1.1 is the schematic of a Li-ion battery, which contains a cathode, an anode, and a polymer membrane separator between the two electrodes. The cathode has active material on the Al current collector and anode has active material on the Cu current collector. Both electrodes and the separator are immersed in the electrolyte. Both the cathode and anode materials allow Li ions to be inserted or extracted. The electrolyte and separator are Li ions conductors, but insulator to electrons. [6]

The cathode is a thin film consists of the mix of an active material, a conductive additive, and a binder casted on the Al current collector. For Li-ion batteries, olivine $LiFePO_4$, layered $LiCoO_2$, and spinel $LiMn_2O_4$ are the commercialized cathode materials which are most extensively investigated. Figure 1.2 is the schematics of the crystal structures of these typical cathode materials for Li-ion batteries. The structure of $LiFePO_4$ is shown in Figure 1.2 a).

The hcp arrayed oxygen forms octahedral and tetrahedral sites, the octahedral sites are occupied 50% by Fe and 12.5% by Li. The LiO_6 octahedral are edge-shared while the FeO_6 octahedral are corner-shared. Although the material shows excellent cycling performance, its poor rate capability which is limited by the 1 dimensional ion diffusion and poor electronic conductivity. The average voltage of this material is ~3.4 V with a moderate capacity of ~ 160 mAh g^{-1}, which results in an energy density less than 560 Wh kg^{-1}. The structure of $LiCoO_2$ is shown in Figure 1.2 b). The oxygen forms close-packed lattice with Co and Li located in the octahedral sites. The transition metal oxygen slabs and Li layers are stacked alternatively in ABCABC sequence. The Li diffuses within the Li layer, forms a 2 dimensional pathway. Due to the intrinsic structure instability of the $LiCoO_2$, when more than 0.5 Li is extracted from $LiCoO_2$, it only delivers half of the theoretical capacity which is about 140 mAh g^{-1}. With an average operation voltage at ~ 4.0 V, the energy density of $LiCoO_2$ is around 560 Wh kg^{-1}. Figure 1.2 c) shows the structure of $LiMn_2O_4$. The oxygen also forms close-packed lattice. The Mn occupies the 25% octahedral site in the Li layer, and 75% octhedral sites in transition metal layer. The Li occupies the tetrahedral sites in Li layer which share faces with the 25% empty octahedral sites in the transition metal layer. The structure provides a three dimensional Li diffusion pathways, leads to good rate performance. The average voltage of this material is ~4.0 V with a low capacity of ~ 120 mAh g^{-1}, which results in an energy density around 480 Wh kg^{-1}.[7, 8 3]

Since most active materials are semiconductors or insulators, carbon based conductive additives such as acetylene black, is required to enhance the electronic conductivity of the cathode. In addition, polymer binders for example PVDF (poly-vinylidene fluoride) or PTFE (polytetrafluoroethylene) are utilized to hold the active materials, conductive additives, and current collectors together.

The separator is a polymer membrane prevents the direct contact between the cathode and anode, which is an ionic conductor but electron insulator. The separator should be chemically and electrochemically stable to both electrodes and the electrolyte. Commonly used separators are porous films of PE (polyethylene), PP (Polypropylene), or multilayer composite separators such as PP/PE/PP.[9]

The liquid electrolyte is a solution of Li salts and organic solvent. Usually the solvent is a mixture of different carbonates such as EC (ethylene carbonate), DMC (dimethyl carbonate) and DEC (diethyl carbonate). The most common salts which have been extensively used are $LiClO_4$, $LiBF_4$, and $LiPF_6$.[10, 11]

The most widely used anode active materials in commercialized batteries are carbon-based materials, such as graphite or Mesocarbon Microbead (MCMB). The graphite shows hexagonal layered structure, which allows Li ions stays into interlayers. The specific capacity of graphite is 372 mAh g^{-1} which corresponds to the formula LiC_6, the average voltage is 0.1 - 0.2 V versus Li^+/Li.[10]

During the charge and discharge process, the Li travels between the cathode and anode. Here I use the $LiCoO_2$/graphite system as an example.

During the charge, the Li ions are extracted from the cathode, and inserted into anode.

$$LiCoO_2 \leftrightarrow Li_{1-x}TMO_2 + xe^- + xLi^+, x < 0.5 \text{ (eq. 1.1)}$$

$$xLi^+ + 6C + xe^- \leftrightarrow Li_xC_6 , x < 1 \text{ (eq. 1.2)}$$

As shown in Figure 1.1 the Li ions are driven by the electric force from the cathode to the anode through the electrolyte, and the electrons flow through the external circuit. Upon the discharge, the Li ions are moved from the anode and inserted into the cathode.

During the charge and discharge, the electrolyte get either oxidized or reduced, thus forms a protective film on the graphite, which is called the SEI (solid electrolyte interphase). The film on the cathode side is called the CEI (cathode electrolyte interphase).[11]

1.3. The Li-rich layered oxide cathode material

1.3.1. Introduction of Li-rich layered oxide cathode

With the commercialization of lithium ion batteries in the 1990's, the layered oxide materials have dominated as the primary positive electrode materials since the earliest developed layered oxide, $LiCoO_2$.[7, 8] With the continued declining costs in battery pack manufacturing and the costs among market leaders being much lower than previously reported, the resurgence of electric vehicles can be attributed to the development of lithium-ion battery technology as a viable energy storage device with the potential of meeting the future demand to totally electrify transportation or, at the very least, percolate

away from fossil fuels.[12] Despite its achievements in performance and ubiquity in mobile devices, a drastic increase in energy density must be achieved to enable the widespread adoption of electric vehicles. Within the practical operating conditions of today, the current generation of layered oxide materials does not meet the future energy storage demands of 350 Wh kg^{-1} at the cell level which roughly translates to over 800 Wh kg^{-1} at the positive electrode level established by the US Department of Energy.[13] One potential positive electrode material that can meet the high-energy demands is the lithium-rich layered oxide (LLO) or Li-excess materials. Unlike the classical layered oxides, LLO exhibits capacities that go beyond conventional topotactic mechanistic theoretical values[14]. As seen on Figure 1.3, starting with early experiments performed by Thackeray et al.[15] on Mn-based systems, the capacities have been steadily increasing at an average of 5 mAh g^{-1} each year from ~200 mAh g^{-1} close to 350 mAh g^{-1} (326 mAh g^{-1} with a 0.1 C rate at room temperature[16]), while the commercially adopted positive electrode materials such as $LiNi_{0.8}Co_{0.15}Al_{0.05}O_2$ (NCA) have reached a value close to ~200 mAh g^{-1} (the red dashed line is NCA and the black dashed line are the highest capacities exhibited by the LLO material in each respective year).[17] The Ni-Mn-Co systems and its TM (transition metal) derivatives including Mn, Ni-Mn, Mn-Cr, Mn-Fe, Mn-Co, are predominantly studied due to adoptability from the classical layered oxides already established (corresponding colored open circles in Figure 1.3). Relatively, Co-free or low Co-containing materials are favored due to the high cost associated with layered cobaltate materials. Therefore, a large number of studies focus on Ni-Mn-Coand Ni-Mn and most

have shown to exhibit the highest reversible capacities with each respective year in Figure 1.3 (black dashed line). In the perspective of cost and raw materials, the Mn and Mn-Fe metal-based systems would be ideal. However, the electrochemical performance of these systems and stability issues limits their practical application. Furthermore, the process in synthesizing the Mn-Fe based systems to form the ideal structure is, so far, highly complex and involves several steps.

Figure 1.4 shows the Ragone plot of the highest capacities exhibited of each respective year where energy and power density are plotted showing its performance capabilities at the material level.[17] In general, this class of material exhibits the highest energy densities, exceeding 1000 Wh kg^{-1}, in comparison to the spinel ($LiNi_{0.5}Mn_{1.5}O_4$ ~ 620 Wh kg^{-1})[18, 19] and olivine ($LiFePO_4$ ~ 430 Wh kg^{-1})[18, 20] materials. Energy and power density were estimated from 1st cycle discharge capacity versus voltage curves from the respective papers. Despite its high capacities, this material has several challenges (voltage fading, structural instability, sluggish kinetics, etc.) that must be overcome in order to integrate it into commercial use.

1.3.2. The structure of Li-rich layered oxide cathode

The LLO materials, often denoted as $(1-y)Li_2MnO_3 \cdot yLiTMO_2$ (TM=Mn, Co, Ni) have been described as either a composite or solid solution of the rhombohedral $LiMO_2$ ($R\overline{3}m$ space group) and monoclinic Li_2MnO_3 structures (C2/m space group). Alternatively, the Li_2MnO_3 can be

written as $Li[Li_{1/3}Mn_{2/3}]O_2$ to describe both structures as layered α-$NaFeO_2$-type rock salt structures with cation ordering or long-range Li in-plane ordering and a $\sqrt{3}a_{hex}$ x $\sqrt{3}a_{hex}$ superstructure in the TM layer.[21, 22] While there is evidence for both the composite and solid solution structures,[23-32] the debate concerning the pristine structure still has not reached a conclusion. However, there is some evidence that the pristine structure is largely dependent on composition and synthesis conditions.[27, 28, 30, 33-37] Utilizing a solution-based combinatorial approach,[38] Mccalla et al. studied large arrays of compositions within the Gibb's triangle for the Li-Mn-Co-O and Li-Mn-Ni-O under different cooling rates.[33, 35]

For the Li-Mn-Co-O system,[33] a solid solution extending the entire composition line between Li_2MnO_3 and $LiCoO_2$ does shift when samples are heat treated at different temperatures and subsequently quenched or slowly cooled where the identification of multiple phases including the layered-layered phase separation was through peak broadening in X-ray diffraction patterns. Bareño et al. have observed this nanoscale phase segregation in the non-quenched $Li_{1.2}Co_{0.4}Mn_{0.4}O_2$ using extended X-ray absorption fine structure.[26] Similarly, the Li-Mn-Ni-O system nanoscale phase segregation has a strong dependence on cooling rates where the boundaries within the diagram can move dramatically, although key features in the phase diagram remain.[35] Interestingly, a distinct "bump" can be observed near the Li_2MnO_3 region of the diagram suggesting metal-site vacancy (Li and/or TM) within Li-deficient structures. This was confirmed

by Monte Carlo simulation, X-ray diffraction, and redox titration where the presence of vacancies may promote the formation of a solid solution.[34] While the role of the vacancies on the electrochemical behaviour is still not well understood, it has been suggested that it may have a positive impact on lowering the irreversible capacity.[39] The route-dependent phase segregation has also been observed at the atomic level using electron microscopy and X-ray energy dispersive spectroscopy to observe the nanoscale phase separation and selective surface cation segregation in pristine $Li_{1.2}Ni_{0.2}Mn_{0.6}O_2$ after high temperature calcination.[37, 40] Zheng et al. showed that a uniform distribution of TMs could be achieved when they applied a hydrothermal synthesis route that exhibits a solid solution-like C2/m monoclinic symmetry. The hydrothermally synthesized LLO material with uniform TM distribution showed a much improved cycling retention with minimal voltage fade when compared to the phase segregated LLO materials cycled for 200 cycles.[36]

With these recent findings, it is apparent that the different synthesis parameters as well as the materials characterization methods for pristine LLO materials must be heavily scrutinized as they have a large impact on the overall battery performance.

1.3.3. The challenges of Li-rich layered oxide cathode

Within the last ten years, a certain amount of fundamental studies have been carried out aimed at understanding the complex reactions and structural

evolutions of the LLO material upon electrochemical cycling, in particular ones that culminate as irreversible processes.[24, 41-52] In this section we will discuss the irreversible loss of lattice oxygen, its impact on the electrode/electrolyte interphase, and how the Li ion and TM ion migration induces the gradual evolution of surface and bulk structure of the LLO material.

1.3.3.1. Surface-related reactions and mechanisms

The most significant feature of the Li-rich layered oxide is the long oxygen activation plateau, which only appears at its first charge when the cut-off voltage is set to be more than 4.6V for the Ni-Mn-Co systems and its derivatives.[24, 52] This oxygen activation plateau consists of the participation of reversible O_2^{n-}/$2O^{2-}$ redox process and irreversible loss of lattice O^{2-}.[41, 53, 54] The reversible process contribute to the high capacity of Li-rich layered oxide. However, the irreversible loss of lattice O^{2-} is the origin of a series of surface reactions and irreversible structural changes upon electrochemical cycling. In 2002, Lu et al. first proposed the lattice oxygen loss, and attempted to quantify the oxygen deficiency via XRD where they found 13.5% oxygen deficiency in the LLO material ($Li[Ni_xLi_{(1/3-2x/3)}Mn_{(2/3-2x/3)}]O_2$, x= 1/6), which has been charged to 4.8V.[52] Later, in 2006, Armstrong et al. directly observed the generation of O_2 gas during this plateau by *in situ* differential electrochemical mass spectrometry (DEMS) that would subsequently cause cooperative displacement of TM diffusing from the surface to the bulk, observed in neutron powder diffraction.[41] With help from the advancement of powerful characterization techniques, researchers have gained

more insights into the irreversible loss of lattice O^{2-} and its role within the surface structure/chemistry transformations. Yabuuchi et al. performed detailed studies using synchrotron XRD, X-ray absorption spectroscopy (XAS), X-ray photoelectron spectroscopy (XPS), and time-of-flight secondary ion mass spectroscopy (TOF-SIMs) showing the formation and deposition of Li_2CO_3 and oxygen-related species, which they believe is a byproduct of the oxygen reduction reaction to form a superoxide upon discharge below 3 V.[44] Zheng et al., performing *in situ* DEMS, not only observed O_2 evolution but a greater formation of CO_2 during the high voltage plateau for $Li[Li_{0.2}Mn_{0.54}Ni_{0.13}Co_{0.13}]O_2$.[46] Hong et al. observed similar gas formation with the evolution of O_2, CO_2 and CO for the first cycle and CO_2 and CO for subsequent cycles with *in situ* DEMS for the $Li_{1.2}Ni_{0.2}Mn_{0.6}O_2$ positive electrode. They also observed the continuous decomposition and formation of Li_2CO_3 upon charging to 4.8 V and discharging to 2 V using FTIR for multiple cycles.[55] They attribute the loss of lattice oxygen and formation of CO_2, CO and Li_2CO_3 to the formation of oxygen radicals from oxygen gas reduced at the conductive surface of the electrode. In addition, the formation of these oxygen radicals would then react with the electrolyte (ethylene carbonate solvent and $LiPF_6$ salt) to form H_2O byproducts. These byproducts subsequently react to form acidic species (HF) that corrodes the surface of the positive electrode and leads to dissolution of Mn.

Hy et al. performed *in situ* surfaced-enhanced Raman spectroscopy (SERS) on Li_2MnO_3, $LiNi_{0.5}Mn_{0.5}O_2$, and $Li_{1.2}Ni_{0.2}Mn_{0.6}O_2$ positive electrodes and observed the generation of Li_2CO_3 and Li_2O for the oxygen evolving materials

($L_{1.2}Ni_{0.2}Mn_{0.6}O_2$ and Li_2MnO_3).[42] For $Li_{1.2}Ni_{0.2}Mn_{0.6}O_2$, the formation of Li_2O was observed to occur during the oxygen activation plateau that subsequently is consumed towards end of charge. Li_2O subsequently reacts with acidic species (HF) to form H_2O that subsequently solvates to the negative electrode (C_6) to form LiOH at the negative electrode changing its SEI. Changes within the electrolyte pH environment as a result of lattice O^{2-} loss were also observed.[42] These side products are formed from the complex reactions taking place between oxygen-related species, the organic electrolyte, and the electrode surfaces, which is driven by the high charge potential. Strategies for suppression of the irreversible oxygen evolution or a means to protect the surface of the electrodes while promoting the participation of the anion redox pair will likely be key to increasing the cycle stability for the LLO material. Further studies of the complex mechanism that occurs at the electrode/electrolyte interphase as well as quantification of the contribution made by each process to the reversible and irreversible capacity will undoubtedly spur the development of the LLO as a positive electrode material. However, while the reactions related to the surface chemistry are important, equally important are the structural changes occurring at the surface and bulk that are also tied to the dynamic changes in oxygen within the lattice.

1.3.3.2. Subsurface structural changes and correlation with performance issues

Electron microscopic techniques have further pushed our understanding of the surface phenomena for the LLO materials. The combination of scanning transmission electron microscopy and electron energy loss spectroscopy (STEM/EELS) has proven to be a powerful tool to obtain structural and chemical information at the atomic scale.[47, 48, 56] Qian et al. performed DFT calculations and STEM/EELS on the positive electrode material $Li[Li_{2/12}Ni_{3-x/12}Co_{2x/12}Mn_{7-x/12}]O_2$ (x=0, 1) to understand the role of oxygen vacancies in cation migration during charging and discharging. EELS spectra shows the O K edge of Li-rich layered oxide after 1 cycle, from bulk to surface.[48] Their results indicate the formation of oxygen vacancies near the material surfaces and sub-surfaces at 5-6 atomic layers where TM ion migration only occurs near these vacancies. Bulk theoretical calculations on the formation of oxygen vacancies in different atomic configurations indicate a strong preference for the Li-Ni-Mn local environment in the transition metal layer. A transition state theory was subsequently used to describe the migration mechanism for Ni and Mn ions where the diffusion barrier in the presence of vacancies is lower relative to no vacancies and the specific location of the oxygen vacancies having a significant impact on the diffusion barrier. The alteration of the O-coordination in the presence of oxygen vacancies for the Ni or TM ions are unstable and spontaneously migrate to a fully-coordinated site near the lithium layer.[48] On the contrary, Delmas proposed a densification model, in which there is TM ion migration from the surface to the bulk with the elimination of oxygen vacancies.[41, 45] Whether or not oxygen vacancies are eliminated during cycling is still under debate. The rearrangement

of cations on the surface is another consequence of lattice O^{2-} loss with the reduction of surface TM ions, including those seen in the Ni-Co-Mn systems. XPS and soft-XAS, which are surface sensitive tools have been used to capture the reduced TM ions on the surface and subsurface at highly charged states.[57-59] As a consequence, the diffusion rates of the surface TM ions would likely be higher than their high oxidation state counterpart. The loss of lattice oxygen would likely form vacancy sites and induce the reduction of surface TM ions, both factors facilitate the migration of TM ions to the Li layer.

More STEM related studies have been carried out on the LLO material after electrochemical cycling. Yan et al.[60] using STEM-EELS, studied the $Li_{1.2}Ni_{0.2}Mn_{0.6}O_2$ positive electrode material and determined chemical and structural changes within two distinct layers that consists of 1) Ni-rich and lithium deficient layers and 2) layers that are prone to surface structural change. They found a sequential surface structural change from C2/m → I41 → Mn_3O_4-Spinel due to a progressive TM enrichment and Li depletion with increasing cycles up to 100 cycles. In addition, the chemical composition change between Ni-rich and surface structural layers was distinguished in which the Ni-rich layers tend to maintain a relatively constant thickness while the surface structural layer tends to increase with increasing cycles. Other researchers reported the observation of rock-salt and spinel phases with electrochemical cycling where the spinel phase has been observed even in the bulk.[60-63] In contrast, Carroll showed no increase of the spinel-like phase up to 10 cycles for the LLO material,[58] and

Boulineau reported growth of the surface spinel phase starting after the 1st cycle and remaining 2-3 nm in thickness after 50 cycles and beyond.[64]

Using STEM with a high angle annular dark field (HAADF) detector and EELS on the LLO $Li_xMn_{0.61}Ni_{0.18}Mg_{0.01}O_2$ positive electrode material, Boulineau observed a surface Ni gradient that is progressive with increasing cycling due to the migration of Mn from surface to bulk and ascribe this phenomenon to the partial structural densification with Mn progressively occupying the vacant lithium sites of the slabs without excluding the possibility of surface Mn dissolution.[64] The resulting surface transformation and positive electrode/electrolyte interphase of LLO may also impede Li diffusion between the electrode/electrolyte interface and surface/bulk interfaces.[58, 65, 42, 44, 55] Additionally, the increased impedance of the cell and deteriorated electrode/electrolyte interface can cause capacity and voltage fading. The dissolution of low oxidation state Mn ions should also be considered as a source of capacity loss.[55]

There has been great progression towards understanding and determining the surface structural transformation that is generally considered irreversible. However, continued efforts at elucidating the complexities and subtle nuances at different length scale will be necessary in order to formulate strategies to mitigate these surface and subsurface structural changes. A better understanding of the specific composition of the subsurface phases would be beneficial. Also, extending the observation of the bare materials with ones that have been modified either

with coatings, surface treatments, additives, or dopants would also shed more light onto their specific role. It will also be necessary to distinguish, ideally quantitatively, the contribution of surface changes from ones that are related to bulk changes that propagate outwards to the surface and ones that are related to surface/electrolyte interphase interactions. It is necessary then to elucidate the phenomenon that encompasses the bulk structure of the LLO materials.

1.3.3.3. Bulk structural changes and correlation with performance issues

As mentioned within the previous section, one of the most serious problems within the LLO materials is the capacity and voltage fading that occurs upon long cycling that continuously decreases the energy density and limits the practical application of this material despite its high energy density at the first cycle.[42, 66, 67] Performance can be easily misinterpreted due to the nonlinear relation between capacity and voltage loss (e.g. high capacities are still possible with voltage decay).

Gu et al. have correlated the layer to spinel phase transformation with voltage fading where the transition is accomplished through the migration of TM ions to the Li layer sites without lattice breakdown.[68] The onset of the voltage fading and hysteresis are intrinsic processes linked to the activation of the Li_2MnO_3 component, which has been correlated to the Li-Mn ordering.[26, 51, 69-75] For hysteresis, cations that have migrated to tetrahedral sites from

octahedral ones during the plateau now migrate back to octahedral sites once sufficient Li insertion has occurred during discharge. For voltage fade, changes in the local structure are induced by the tetrahedral cations (Li-layer octahedral sites) migrating and occupying new sites that are not easily extracted.

DFT calculations,[47] solid state NMR,[76] and neutron diffraction analysis[77, 78] have identified the extraction of Li ions from the TM layer, the formation of tetrahedral Li, and the migration of TM from the octahedral site of TM layers to tetrahedral/octahedral sites in the Li layer during the plateau.[51, 71, 78, 79] Dogan et al. identified the $LiMn_6$-TM_{tet} feature in solid state NMR, which suggests the TM ion migration into the tetrahedral sites in the Li layer and formation of defect sites during the voltage fade process.[51]

Figure 1.5 is a schematic diagram, which summarizes several recent key findings related to phenomena that occur at the surface of the material and the related structural changes. For simplicity, the Ni- containing LLO materials are represented, but the overall reactions and structural changes may be extended to most of the other metal systems with variations of the potentials in which specific changes occur. In the pristine state, the different metals are at the initial oxidation state of M^{m+}, i.e. Ni^{2+}, Mn^{4+}, Co^{3+}, and oxygen at O^{2-}. A degree of Li/Ni mixing is present within the pristine material that is dependent on the synthesis condition and composition. A homogenous distribution of cations is also assumed relative to the different charge/discharged states. As the potential increases to < 4.5 V and Li is

extracted, an increase in oxidation of M^{m+} to $M^{(m+p)+}$ occurs. As the potential increases to >4.5 V, a characteristic long plateau in the charging curve is often observed, signalling the participation of oxygen O_2^{n-} to compensate Li extraction. In the presence of O_2^{n-} a reductive coupling of $M^{(m+p)+}$ to $M^{(m+p-\sigma)+}$ occurs. Within the same region, loss of oxygen ions and formation of oxygen vacancies drive a migration of Li/M ions to tetrahedral/octahedral sites and a segregation of metals. In the case of Ni, Ni-rich surfaces form. In addition, there is a formation of Li_2O on the surface and O_2, CO, and CO_2 gas evolution during and near the end of the plateau. The formation of Li_2O and gases leads to the formation of Li_2CO_3 and other surface species on the positive electrode after discharging to < 2.5 V. Changes within the electrolyte after charging also lead to surface structural changes upon discharging. Due to the redistribution of ions and metal dissolution that may occur, in the discharged state of < 2.5 V some metal ions such as Mn may reduce below their pristine oxidation state to $M^{(m-\omega)+}$. In addition, cycling will increase Li/Ni mixing, making it more difficult to remove migrated M/Li in the tetrahedral sites. After the nth cycle, further segregation may occur as well as fragmentation and corrosion.

1.4. The background of Na-ion batteries

Over the past decade, the worldwide demand to develop electrical energy storage is growing as a result of increased energy demand, rapid increases in the price of fossil fuels and the environmental consequences of their use. To

achieve green and sustainable energy development, the substitution of alternative energy generation and storage for fossil fuels must be considered. Although renewable energy technologies such as wind and solar generated electricity are becoming popular in several developed countries, good energy storage systems are needed by the electrical grid. Going forward with large-scale stationary electrical storage requires more reliable and lower cost new battery systems.[80] The abundance and low cost of Na in the earth can become an advantage when a large amount of alkali is demanded for large-scale applications.

In the past three decades, extensive research efforts from science and engineering have been made mainly for the lithium system for rechargeable batteries. In contrast, sodium intercalation chemistry has been explored considerably less than lithium intercalation system, there may be significant unexplored opportunity in sodium ion batteries. One of the challenges in sodium battery system is the lack of a high energy density cathode material which is safe and low cost. Hence, there may be great opportunity to find novel electrode materials that meet all the criteria for sodium ion battery. Development of high energy density cathode with low cost would enhance the use of an ambient temperature sodium and sodium ion battery on large-scale stationary electrical storage for electrical grid. Furthermore, if the safety is suitable, the sodium ion battery can be utilized in electric vehicles.

Sodium is located below lithium in the periodic table and they show similar chemical properties in many aspects. The fundamental principles of the sodium

ion battery and lithium ion battery are identical, during charge and discharge the alkali ions move back and forth between the two electrodes. With sodium's high abundance and low cost, and very suitable redox potential ($E^{\ominus}Na^+/Na$ = -2.7 V only 0.3 V above that of $E^{\ominus}Li^+/Li$ = -3.0 V).

Studies on sodium ion batteries began in the late 1970s and the early 1980s.[81-83] Sodium-based layered electrode materials can be categorized into two main groups:[84] O3 type or P2 type, in which the sodium ions are accommodated at octahedral and prismatic sites, respectively. A study by Lu and Dahn demonstrated that the P2-layered oxide, $Na_{2/3}[Ni_{1/3}Mn_{2/3}]O_2$, can reversibly exchange Na-ions in sodium cells,[85, 86] but the voltage profile was complicated, showing single and two phase regions, and transformation to O2 structure at high voltage range. More recently, Li substituted $Na_{1.0}Li_{0.2}Ni_{0.25}Mn_{0.75}O_2$ was studied by Kim et al. and displayed 95 mAh g^{-1} of specific capacity, excellent cycling and rate capabilities.[87] It is claimed that Li in the TM layer improves the structural stability during the cycling. Some other P2-type phases seem to achieve a higher capacity as electrode materials. $P2-Na_{0.6}MnO_2$ delivers a large initial capacity of 160 mAh g^{-1},[88] $P2-Na_{2/3}Fe_{0.5}Mn_{0.5}O_2$ delivers higher initial capacity of 190 mAh g^{-1},[89] however the cyclability is insufficient. O3-phase $NaCoO_2$,[82] $NaCrO_2$,[90] $NaVO_2$,[91] $NaNi_{0.5}Mn_{0.5}O_2$[92] and so on are electrochemically active, but the repeatable reversible capacity cannot exceed 120 mAh g^{-1}. Recently, Tarascon successfully synthesized O3-phase $NaNi_{1/3}Mn_{1/3}Co_{1/3}O_2$ which can deliver a reversible capacity of 120 mAh g^{-1}. Their voltage profile shows complicated

phase transformation during charge, followed the sequence O3 $\Rightarrow$ O1 $\Rightarrow$ P3 $\Rightarrow$ P1which was proved by their in-situ XRD work.[93]

Reachargeable ambient temperature sodium and sodium ion batteries can be used for many energy storage applications, especially large-scale stationary electrical storage for electrical grid. Other possible applications for sodium ion batteries including, but not limited to portable device, transportation, defense products, aerospace products and so on. There is a demand for new cathode materials for sodium electrochemical cells and batteries. The present invention addresses this need.

Chapter 1, in part, is a reprint of the material "Performance and design considerations for lithium excess layered oxide positive electrode materials for lithium ion batteries" as it appears in the Energy & Environmental Science, Sunny Hy, Haodong Liu, Minghao Zhang, Danna Qian, Bing-Joe Hwang and Ying Shirley Meng, 2016, **9**, 1931-1954. The dissertation author was the co-author of this paper. The author wrote the challenges for high energy density part. Chapter 1, in part, is a reprint of the material "Lithium and sodium containing cathodes/electrochemical cells" as it appears in the US patent, Ying Shirley Meng, and Haodong Liu, 2015, WO2015035138. The dissertation author was the primary investigator and inventor of this patent. The author wrote the whole patent.

Figure 1.1 Schematic of a rechargeable Li-ion battery.
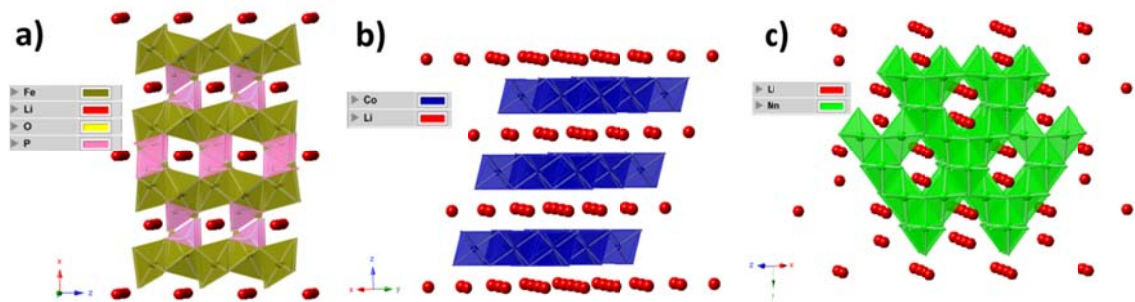
Figure 1.2 Schematics of crystal structures of a) LiFePO$_4$, b) LiCoO$_2$, and c) LiMn$_2$O$_4$.
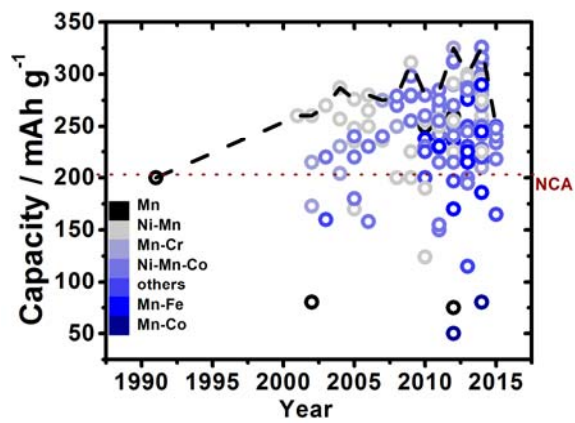
Figure 1.3 Evolution of the discharge capacity by years.
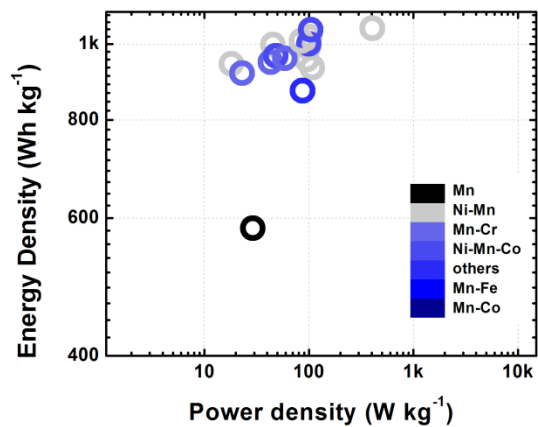
Figure 1.4 Ragone plot at the material level exhibiting the highest first discharge capacity for each year from Figure 1.3 (dashed black line).
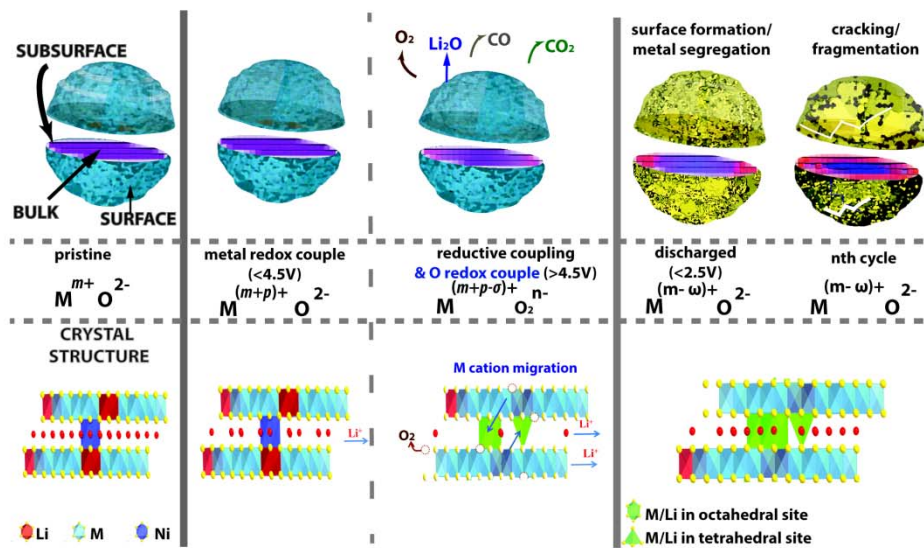
Figure 1.5 Schematic diagram of the changes that occur during electrochemical cycling that occurs within the surface and the crystal structure. The middle represents the changes in the redox for the cation and anions that participate in the charging compensation mechanism.

Chapter 2. Advanced characterization tools

Developing methods to exploit the activity of Li in Li-ion batteries will be essential to understanding the performance. In this regard, the development of Li probing techniques, preferably *operando*, will be the key. Studies for half-cell systems to full-cell systems will give better insight into what different phenomenon may occur under different electrode/electrolyte pairings. Neutron diffraction is one of the most powerful analytical tools used to characterize the structure of a crystalline material and is a primary characterization tool of this work.

2.1. The diffraction for structural analysis

Figure 2.1 is two dimensional illustration of Bragg's law. n is the order of reflection, λ is the wavelength of the incident radiation, d is the spacing of specific lattice planes and θ is the scattering angle between the incident radiation and the lattice planes as shown in Figure 2.1. When incident radiation waves reach a crystalline sample are scattered by the atoms in the system the Bragg diffraction occurs. The equation of Bragg's law:

$n\lambda = 2d \sin\theta$ (eq. 2.1)

The wave-like interaction of the incident beam scattered by the crystalline sample generates diffraction patterns. The number of peaks observed in a diffraction pattern depends primarily on the space group, and atom positions in the unit cell. The analysis of diffraction patterns, the

Rietveld refinement has been widely adopted by researchers. Through the use the Rietveld refinement, the lattice parameters, atomic positions, atomic occupancies could be achieved.

2.2. The advantages of neutron diffraction for Li-ion batteries research

Figure 2.2 (a) is the schematic of X-ray and neutron interact with atoms. X-ray scattering interacts with the electrons surrounding the atoms, whereas neutron interacts with the atomic nuclei of materials. Figure 2.2 (b) compared the neutron and X-ray atomic scattering powers. The scattering power of X-rays depends on the numbers of electrons in an atom, which gives low sensitivity to light elements and low contrast among neighbouring elements. Neutron scattering has several distinct advantages for battery studies: 1) The sensitivity of neutron to light elements such as lithium and oxygen are significant in order to determine their position in the crystal structure; 2) Compares to the X-ray, the neutron shows larger scattering contrast between neighboring elements in the periodic table specifically the scattering lengths, e.g. for transition metals in this case: Ni, 10.3 fm; Mn, -3.73 fm; Co, 2.49 fm; and 3) The deep penetration capability of neutron allows simultaneous observation of the cathode and anode.

Figure 2.3 shows the XRD and ND refinements of $Li_{1.2}Ni_{0.2}Mn_{0.6}O_2$ and surface modified $Li_{1.2}Ni_{0.2}Mn_{0.6}O_2$. Due to the similarity in sizes of Li^+ (76 pm) and Ni^{2+} (69 pm), the Li^+ and Ni^{2+} mixing exists in all the Ni based layered oxide cathodes.[67] The X-ray diffraction shows exchanged Li of $Li_{1.2}Ni_{0.2}Mn_{0.6}O_2$ in TM

layer reduced from 0.062(2) to 0.048(4) after surface modification. However, this surface modification should not change the bulk property of $Li_{1.2}Ni_{0.2}Mn_{0.6}O_2$. As a comparison, the neutron diffraction shows similar exchanged Li in TM layer, 0.037(1) and 0.039(5), respectively. This example verifies that the neutron is more sensitive to the Li than X-ray.

Figure 2.4 illustrates the XRD and ND of $LiNi_{0.8}Co_{0.158}Al_{0.05}O_2$. The Rietveld refinements are carried out using $LiNi_{0.8}Co_{0.158}Al_{0.05}O_2$ model and $LiNi_{0.5}Mn_{0.3}Co_{0.2}O_2$ model, respectively. Since Ni, Co, and Mn stays very close in the periodic table, the scatterings in X-ray are not able to distinguish these atoms. As a result, both models fit very well with the XRD pattern of $LiNi_{0.8}Co_{0.158}Al_{0.05}O_2$. In the case of neutron diffraction, the fitting using $LiNi_{0.8}Co_{0.158}Al_{0.05}O_2$ model is very good. But the $LiNi_{0.5}Mn_{0.3}Co_{0.2}O_2$ model gives not only mismatches in a few peaks, but also leads to unreasonable structural information. This example proves that the neutron is better than X-ray to distinguish neighbor elements in periodic tables.

Figure 2.5 plots the lab XRD, synchrotron XRD and ND of $Li_{1.13}Ni_{0.3}Mn_{0.567}O_2$. The oxygen occupancies of $Li_{1.13}Ni_{0.3}Mn_{0.567}O_2$ in three patterns are refined, which shows 2.193, 2.043, and 1.997 O in the formula, respectively. This example indicates the lab XRD, synchrotron XRD, and ND give around 9.7%, 2.2%, and 0% relative errors on oxygen occupancies.

2.3. The current state of art *operando* neutron diffraction studies in Li-ion batteries

The neutron diffraction is powerful tool for Li-ion batteries research. *Operando* characterization observes the real time structural or chemical information under real reaction, which could monitor the dynamic process, phase transition, and avoids the structural relaxation. However, challenges exist in broadening the application of *operando* neutron diffraction for Li-ion batteries research. First, limited by the generation reactions of neutrons, the neutron flux is usually several orders of magntitude lower than X-rays. In another words, longer acquisition times as well as larger amounts of samples are required for neutron diffraction experiments. In addition, the existence of hydrogen, which has a large incoherent neutron-scattering cross-section, is detrimental to the signal-to-noise ratio of neutron diffraction pattern. Separators (polyethylene based porous membrane) and poly carbonate based electrolyte solutions contain a considerate amount of hydrogen. These two major reasons pose significant challenges to *operando* neutron diffraction for Li-ion battery research although it is such a powerful technique for light elements like lithium.

Figure 2.6 (a) is statistics of publications reporting *operando* neutron studies of Li-ion batteries. There are only around 40 publications on this topic, most works are published after 2010. The number of publications reach the peak in 2014, then goes down. There are three major reasons prevents people using the *operando* neutron diffraction Li-ion battery research: 1) the access to the neutron sources is much harder than X-ray sources; 2) as mentioned before, the neutron experiments require large quantity of samples, as a consequence, a specific cell design is required to get good neutron diffraction signals; 3) neutron

detects cathode, anode, current collectors in a battery, the data analysis become very difficult.

Figure 2.6 (b) summarizes the electrode systems which are studied by the *operando* neutron diffraction. Because almost all the Li-ion batteries contain graphite anodes, 28.81% works studied the behavior of graphite anodes, though it has been heavily studied by X-rays. Due to the easy access to the commercialized batteries, the layered LCO, and LFP occupies 25.42% published works. The spinel system belongs to cubic symmetry, which results in relative easy data analysis. The spinel LMO, LNMO, and LTO are also studied a lot. Only two works focused on the Li-rich materials, which will be discussed later in this thesis.

Figure 2.6 (c) shows the battery designs for *operando* neutron diffraction. The key to guarantee a successful *operando* neutron diffraction is to balance the signal to noise ratio and electrochemical performance. In this thesis, the author choose the pouch cell design, which could provide sufficient material exposed to the neutron beam, the performance of a cell is also maintained.
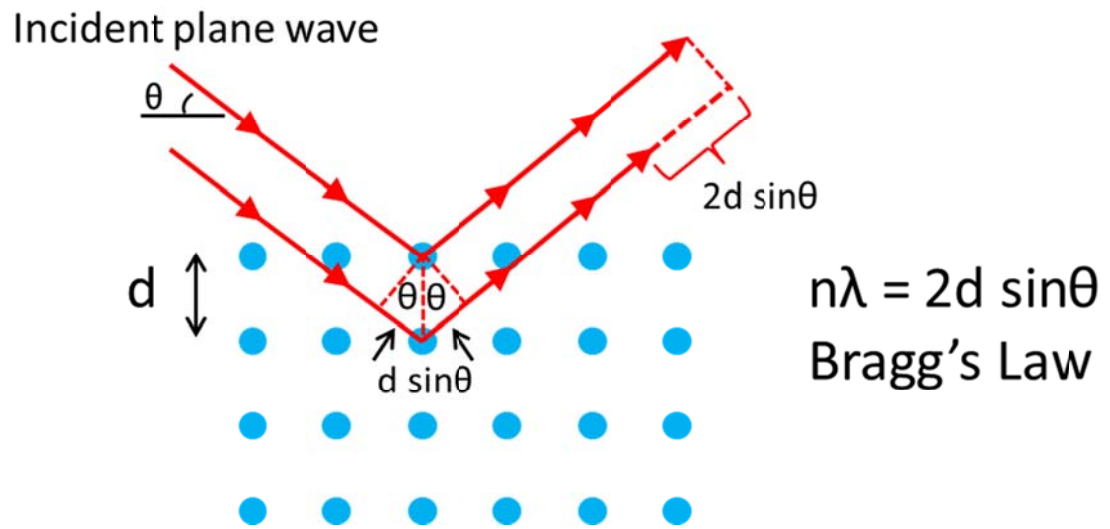
Figure 2.1 Two dimensional illustration of Bragg's law.
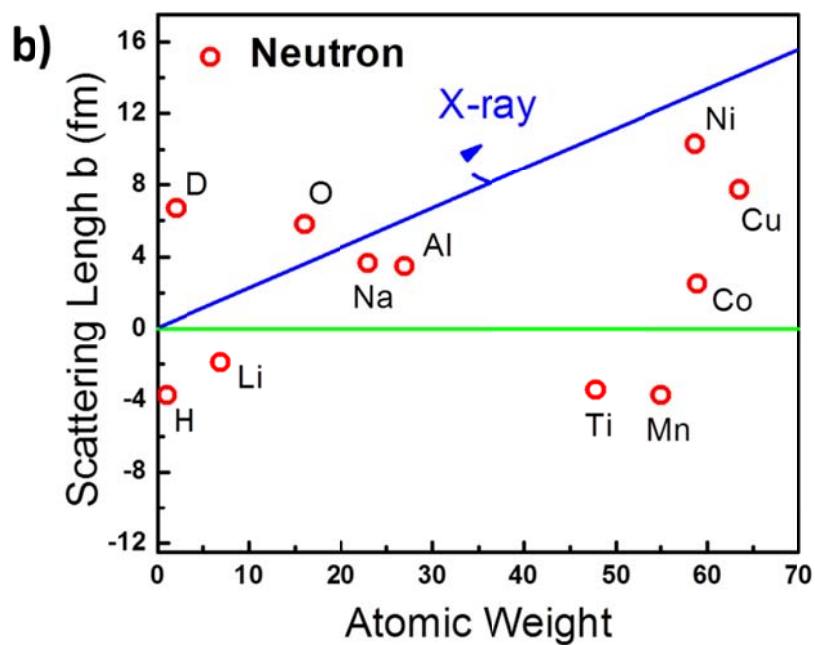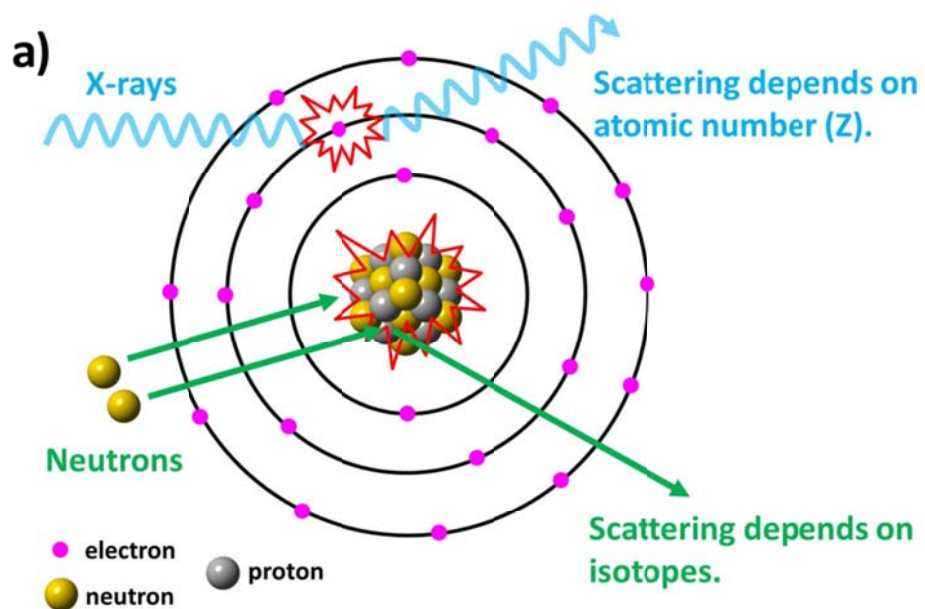
Figure 2.2 (a) The schematic of X-ray and neutron interact with atoms. (b) Comparison of neutron and X-ray atomic scattering powers.
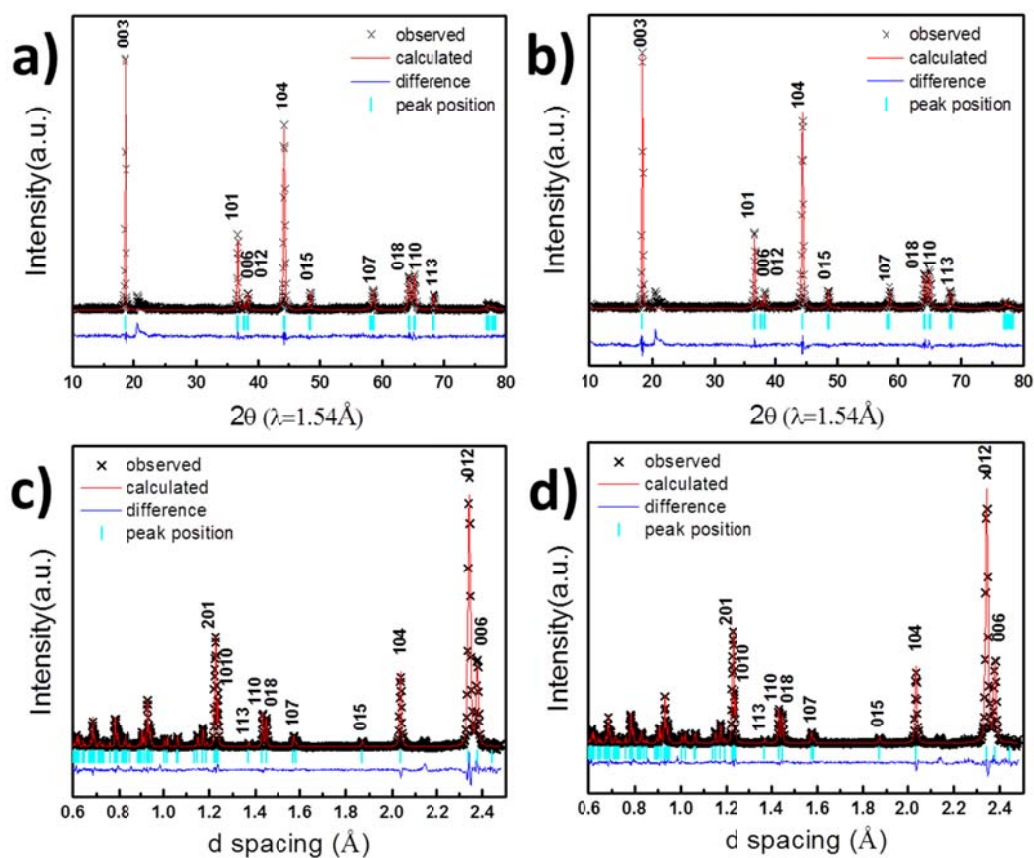
Figure 2.3   (a) The XRD of $Li_{1.2}Ni_{0.2}Mn_{0.6}O_2$. (b) The XRD of surface modified $Li_{1.2}Ni_{0.2}Mn_{0.6}O_2$. (c) The ND of $Li_{1.2}Ni_{0.2}Mn_{0.6}O_2$. (d) The ND of surface modified $Li_{1.2}Ni_{0.2}Mn_{0.6}O_2$.
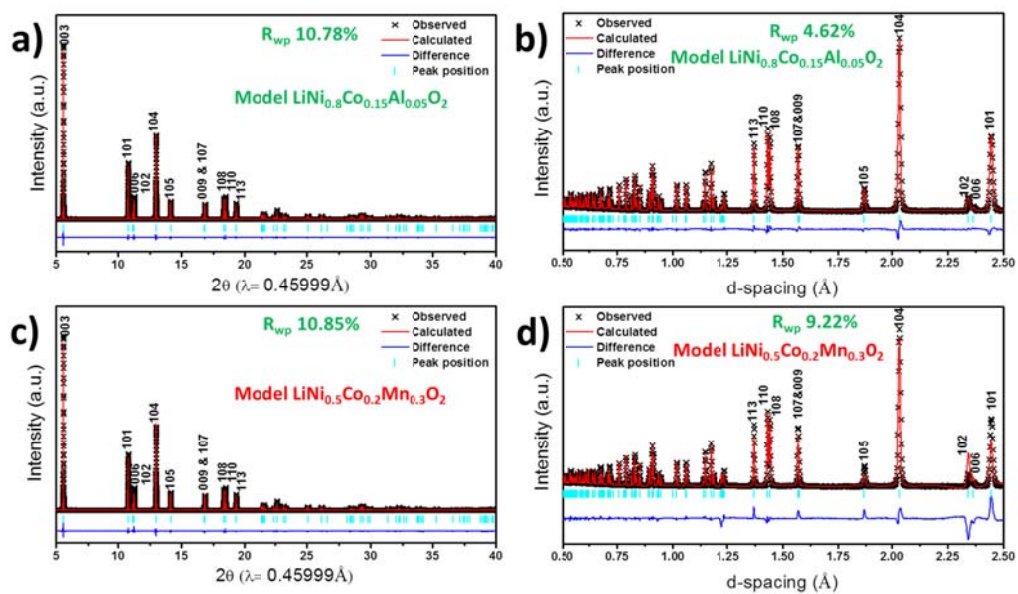
Figure 2.4 The XRD of $LiNi_{0.8}Co_{0.158}Al_{0.05}O_2$ (a) using $LiNi_{0.8}Co_{0.158}Al_{0.05}O_2$ model; (c) using $LiNi_{0.5}Mn_{0.3}Co_{0.2}O_2$ model. The ND of $LiNi_{0.8}Co_{0.158}Al_{0.05}O_2$ (b) using $LiNi_{0.8}Co_{0.158}Al_{0.05}O_2$ model; (d) using $LiNi_{0.5}Mn_{0.3}Co_{0.2}O_2$ model.
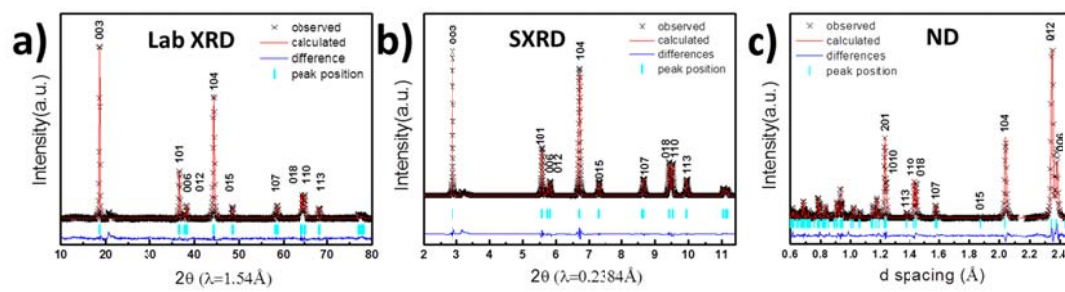
Figure 2.5 The refinement of $Li_{1.13}Ni_{0.3}Mn_{0.567}O_2$ (a) using in house lab XRD; (b) using APS synchrotron XRD; (c) using neutron diffraction.
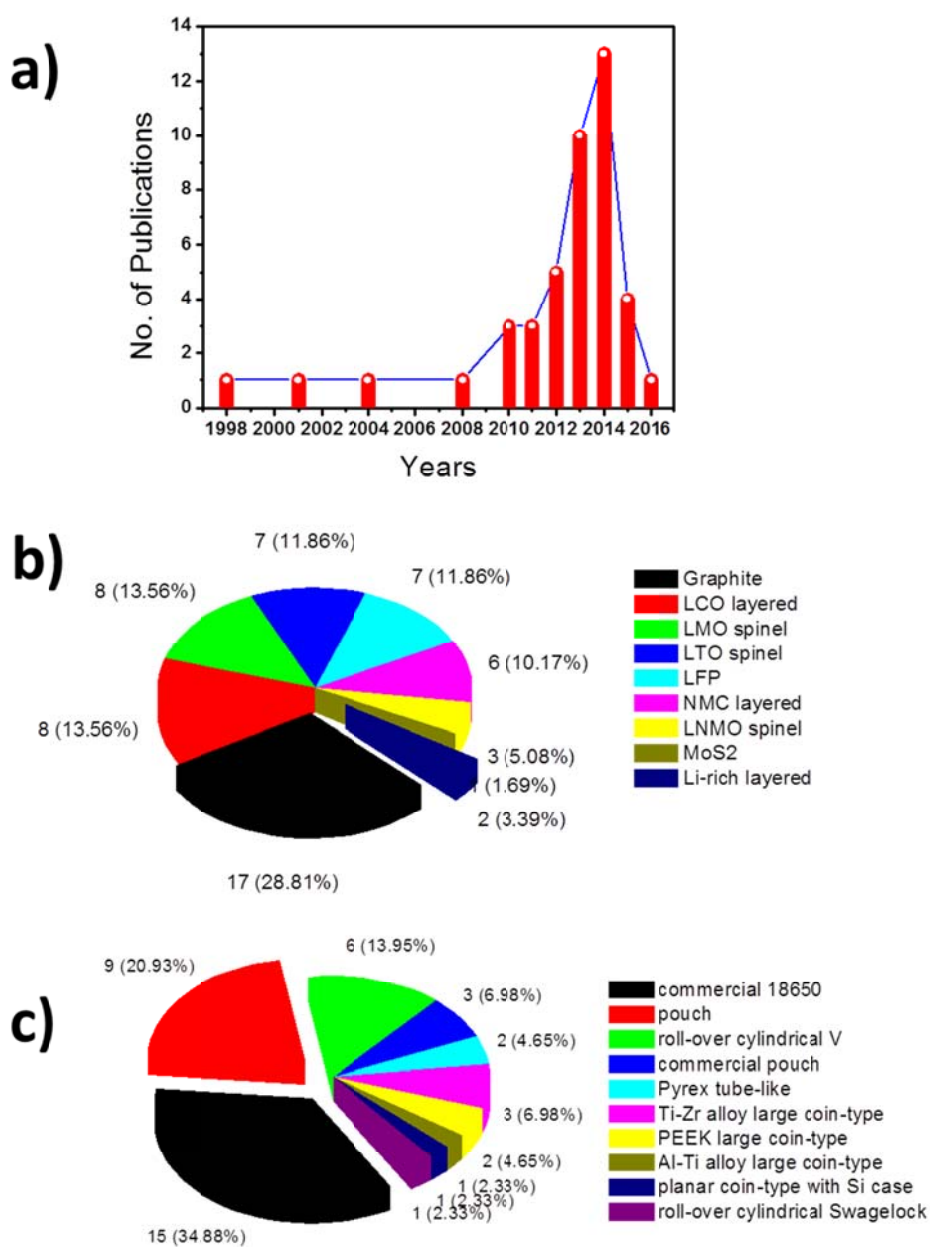
Figure 2.6 (a) Statistics of publications reporting *operando* neutron studies of Li-ion batteries. (b) Statistics of *operando* neutron studies on electrode materials. (c) Statistics of battery types for *operando* neutron studies.

Chapter 3. *In-situ* neutron diffraction study of the xLi2MnO3.(1-x)LiMO2 (x= 0, 0.5; M= Ni, Mn, Co) layered oxide compounds during electrochemical cycling

The layered oxide compounds $xLi_2MnO_3 \cdot (1-x)LiMO_2$ (M= Ni, Mn, Co) are of great interest as positive electrode materials for high energy density lithium-ion batteries. *In-situ* neutron diffraction was carried out to compare the structural changes between the classical layered compound $Li[Ni_{1/3}Mn_{1/3}Co_{1/3}]O_2$ (x=0) and lithium-excess layered compound $Li[Li_{0.2}Ni_{0.18}Mn_{0.53}Co_{0.1}]O_2$ (x=0.5) during electrochemical cycling. In this work, lab made pouch cells were built for the *in-situ* study and graphite was used as the anode material. Irreversible structural change of $Li[Li_{0.2}Ni_{0.18}Mn_{0.53}Co_{0.1}]O_2$ during first charge (4.7V)/ discharge cycle (2.0V) was indicated by dynamic changes in lattice d-spacing, while the $Li[Ni_{1/3}Mn_{1/3}Co_{1/3}]O_2$ showed completely reversible structural evolution between 4.4V-2.5V. *Ex-situ* neutron powder diffraction was performed on both pristine and chemically delithiated lithium-excess layered compounds to better understand the irreversible structure change.

3.1. Introduction

Rechargeable lithium-ion batteries play a significant role in many portable devices such as laptops and cell phones. They are emerging as the energy

storage systems for electric vehicles because of high energy density and long cycle life. The layered oxide compounds $xLi_2MnO_3.(1-x)LiMO_2$ (M= Ni, Mn, Co) are of great interest as a new generation of positive electrode materials for high energy density lithium-ion batteries because of their high energy density at lower costs. The currently commercialized $LiNi_{1/3}Mn_{1/3}Co_{1/3}O_2$ (x=0) cathode material, has firstly been reported to have a capacity of 150 mAh g^{-1} in the voltage window of 2.5 – 4.2V by Ohzuku et. al.,[94] and 200 mAh g^{-1} in the voltage window of 2.5 – 4.6V.[95] S. C. Yin et. al. suggest an upper cutoff voltage of 4.3 – 4.4V for good cycling retention, as their observation shows that in this voltage window Lithium de/re-intercalation is reversible.[96] Recently, there is a intense research effort focused on the Lithium excess material $xLi_2MnO_3 \cdot (1 - x)LiMO_2$ (in $LiMO_2$, M= Ni, Mn, Co) where x > 0, which has excess Li in the transition metal layer. The X-ray diffraction pattern of the layered oxides can be refined with the α-NaFeO$_2$ structure (R-3m). [94-96] Superlattice peaks exist in the X-ray diffraction pattern between 20 and 25° (2θ), which are associated with a honeycomb ordering of Li^+, Ni^{2+}, Mn^{4+}, and Co^{3+} in the transition metal layer.[97, 98] The Lithium-excess materials can deliver reversible capacities in excess of 250 mAh g^{-1} when the x is close to 0.5,[24, 52, 99] but large irreversible capacity up to ~ 100 mAh g^{-1} exists in the first charge and discharge between 2V and 4.8V, several groups have proposed detailed mechanisms for this large irreversible capacity.[47, 100] During the initial charging region in first cycle, as lithium is removed from the layered structure the capacity originates from the oxidation of Ni^{2+} to Ni^{4+} and Co^{3+} to $Co^{3.6+}$ up to 4.4V. A high voltage plateau region around 4.5V appears after the

slope region. The large first cycle irreversible capacity has been mainly attributed to an irreversible loss of oxygen from the lattice during the first charge accompanied by Li removal. It is also a result of side reactions with the electrolyte on the electrode surface.[52, 100, 101] However, it is still up to debate where the anomalous high reversible capacity comes from in the lithium excess layered oxides. In order to gain more in-depth insights about the differences in classical layered oxide (x=0) and lithium excess layered oxide (x=0.5), *in-situ* neutron diffraction experiments were designed to observe the structural and compositional changes in these oxides during electrochemical process.

Previous literature has focused heavily on the use of X-ray scattering to understand the structural evolution of these materials. Recently, an *in-situ* XRD study has been done on the $Li[Li_{0.2}Ni_{0.2}Mn_{0.6}]O_2$ to investigate the structural change and mirco-strain during the first electrochemical cycle.[102] In addition, an *in-situ* XAS experiment was performed on the $Li[Ni_{0.17}Li_{0.2}Co_{0.07}Mn_{0.56}]O_2$ to study the charge–discharge reaction mechanism in the first 2 cycles.[103] However, X-ray scattering is limited in that it interacts with the electrons surrounding the atoms making it difficult for Li-ion battery compounds, whereas neutron interacts with the atomic nuclei of materials. Neutron scattering has several distinct advantages over x-ray scattering for *in-situ* battery studies[104]: 1) Deep penetration that allows simultaneous observation of the cathode and anode; 2) Larger scattering contrast between neighboring elements in the periodic table specifically the scattering lengths, e.g. for transition metals in this case: Ni, 10.3 fm; Mn, -3.73 fm; Co, 2.49 fm;[96] and 3) The sensitivity to light elements such as Li is significant in

order to estimate their position in the crystal structure. However, due to the large incoherent neutron-scattering cross-section of hydrogen, the existence of hydrogen is detrimental to the signal-to-noise ratio of neutron diffraction pattern. Separators (polyethylene based porous membrane) and poly carbonate based electrolyte solutions contain large amount of hydrogen. This poses a significant challenge to *in-situ* neutron diffraction for lithium ion battery research although it is such a powerful technique.

The number of *in-situ* ND studies are limited and have focused on traditional materials such as $LiCoO_2$,[104, 105] $LiMn_2O_4$,[106, 107], $Li_4Ti_5O_{12}$[108] and graphite[109]. In order to avoid large absorption from the presence of hydrogen in the separator and electrolyte, most studies use a special designed electrochemical cell[104-106, 108, 109]. In this work, lab made pouch cell were designed for *in-situ* ND study. Both $LiNi_{1/3}Mn_{1/3}Co_{1/3}O_2$ and $Li[Li_{0.2}Ni_{0.18}Mn_{0.53}Co_{0.1}]O_2$ materials are studied by *in-situ* neutron diffraction during electrochemical cycling on the engineering materials diffractometer VULCAN (see the references), at Spallation Neutron Source, Oak Ridge National Laboratory. The structural transition behaviors of the two cathode compounds during the first few cycles are presented. Structure change and phase transition of anode graphite is also discussed briefly in this article.

3.2. Experimental Methods

3.2.1. Synthesis

A coprecipitation followed by two steps calcination was used for the synthesis of the materials.[65] Transition metal (TM) nitrates, $Ni(NO_3)_2 \cdot 6H_2O$ (ARCROS, 99%), $Co(NO_3)_2 \cdot 6H_2O$ (ARCROS, 99%), and $Mn(NO_3)_2 \cdot 4H_2O$ (Alfa Aesar, 98%) were dissolved into deionized water then titrated into $LiOH \cdot H_2O$ (Fisher) solution. The coprecipitated TM hydroxides were then filtered using vacuum filtration and washed three times with deionized water. The collected TM hydroxides were dried in an oven at 180°C for 10 h in air. The dried TM precursors were then mixed with a stoichiometric amount of $LiOH \cdot H_2O$ (Fisher) corresponding to the amount of $M(OH)_2$ from the coprecipitation step. This mixture was ground for 30 min to ensure adequate mixing and then placed into a furnace at 480°C for 12 h. The precalcinated powders were then calcinated at 900 °C for 12 h in air.

Chemical delithiations were performed in a glovebox (argon atmosphere) with < 1ppm moisture, $Li_{1.2}Ni_{0.2}Mn_{0.6}O_2$ was mixed with the designed amount of NO_2BF_4 (ARCROS, 97%) in acetonitrile (Alfa Aesar, 99.8%) and stirred for 24 hours, then filtered.

3.2.2. Cell design

Figure 3.1 (a) is a simple schematic of our pouch cell, which includes a dual sided graphite anode (the anode is based on standard graphite material) and two pieces of single side cathode. The electrode loading for the anode and $Li[Li_{0.2}Ni_{0.18}Mn_{0.53}Co_{0.1}]O_2$ cathode is around 8 mg cm^{-2}, while the loading for $LiNi_{1/3}Mn_{1/3}Co_{1/3}O_2$ cathode is around 12 mg cm^{-2}. This cell configuration design

aimed at increasing the loading of active materials in our pouch cells to increase neutron diffraction pattern statistics. Cells were all assembled in a glovebox under argon atmosphere. A Celgard separator is used to cover the anode with a piece of single side cathode on each side of the anode. The electrolyte solution composed of 1 M $LiPF_6$ in a 1:1 ethylene carbonate (EC):dimethyl carbonate (DMC). The cathode is composed of 90% active material, 5% PVDF and 5% carbon black on an aluminum collector. In order to ensure the full charge performance of the cathode materials, about 25% excess anode material was used in the pouch cell.

3.2.3. *In-situ* neutron diffraction

A Bio-Logic SP-300 potentiostat was used to electrochemically cycle the cell under constant charge and discharge currents. The $Li[Li_{0.2}Ni_{0.18}Mn_{0.53}Co_{0.1}]O_2/C$ pouch cell was charged at 32 mA (~ C/15) to 4.7V then discharged at -27 mA (~ C/15) to 2V while the $LiNi_{1/3}Mn_{1/3}Co_{1/3}O_2/C$ pouch cell was charged at 43.2 mA (~ C/5) to 4.4V then discharged at -43.2 mA (~ C/5) to 2.5V. In order to observe more cycles within the limited beam time, the following cycles between a voltage range of 2.5 – 4.4V were using ±84 mA (~ C/2) to charge and discharge. Figure 3.1 (b) is the cell set up at the VULCAN beamline. An incident beam (5mm*12mm) of 0.5 to 3.5 Å bandwidth allowing 0.5~2.5 Å d-space in diffracted pattern in the $\theta\pm90°$ detector bank was selected using the double-disk choppers at 30 Hz speed. The SNS was at nominal 800KW. Time stamped neutron event data were collected while the cells were under

continuous cycling [110]. Neutron diffraction data were sliced (every 3600 seconds) and reduced by the VDRIVE software.[111] Single peak refinements were carried out using the GSAS[112] program.

3.2.4. *Ex-Situ* neutron powder diffraction

Neutron powder diffraction patterns were collected for the lithium excess materials $Li[Li_{0.2}Ni_{0.2}Mn_{0.6}]O_2$ and chemically delithiated lithium excess sample using beamline HB2A [113] at the High Flux Isotope Reactor (HFIR) at Oak Ridge National Laboratory. Samples were loaded in a hermetically sealed holder to prevent air exposure. A monochromatic incident wavelength of 1.54 Å was chosen. Full pattern Rietveld refinement was performed using the GSAS[112] programs with the EXPGUI[114] interface.

3.3. Results and discussion

3.3.1. Cathode in $Li[Ni_{1/3}Mn_{1/3}Co_{1/3}]O_2/C$ pouch cell

Figure 3.2 (a)-(c) shows the charge/discharge curve with surface contour plots of $LiNi_{1/3}Mn_{1/3}Co_{1/3}O_2$ (102), (108) and (110) ND peaks evolution as a function of time. The hydrogen atoms due to the presence of a large volume of electrolyte and separator materials contribute to the large fraction of the background, which reduces the signal-to-noise ratio. Other components in the pouch cell, such as the Al and Cu current collectors have crystalline features and cause ND peak overlap. These factors forced the use of single peak refinement to prevent erroneous full profile fitting results. Since both the cathode and anode

material have a hexagonal lattice, d_{hkl} can be calculated by using the equation below:

$$1/d_{hkl}=\{4/3*[(h^2+hk+k^2)/a^2]+l^2/c^2\}^{1/2} \quad \text{(eq. 3.1)}$$

Figure 3.4 (a) is a- and c- lattice parameters evolution during cycling. During charging, Li^+ is extracted from the layered structure, at the same time Ni^{2+} is oxidized to Ni^{4+} which leads to ionic radii decreasing (e.g. r Ni^{3+}=0.60Å, r Ni^{4+}=0.48Å), as a consequence a- lattice parameter contracted monotonously. The removal of Li^+ introduces a concentration gradient and electrostatic repulsion from adjacent oxygen layers accounting for the increased c- lattice parameter.[115] The (108) peak remains unchanged while (110) decreased rapidly when Li ions are extracted, and at the end of charge (110) planes have the shortest distance. The (108) plane corresponds to the out-of-plane periodicity, which intersects 1 in every 8 transition metal (TM) or Li^+ layers (along the c- axis). The out-of-plane lattice spacing changes correspond strongly to the c- lattice parameter. As l increases in the (10l) family of peaks, the d_{10l} shift decreases in magnitude. Since l here equals to 8 the change of c only brings negligible change of d_{108}. The (110) plane depends strongly on a- lattice parameter, illustrating strong anisotropy in the material during electrochemical cycling. At the beginning of the charge a=2.852±0.001 Å, c=14.173±0.0008 Å which are close to the reported results,[96] and the trends upon charge are consistent with previous work[116]. The discharge is a process of Li^+ reinserting into the layered structure. After discharge, a- and c- parameter return to a=2.851±0.001 Å, c=14.179±0.0006 Å illustrating a completely reversible intercalation mechanism. Figure 3.2 (e)-(f)

show the (102), (110) and (108) peaks in the following cycles, only 5-7th cycles data were collected due to beam off during 2nd-4th cycles. But we can clearly see the (108) remains unchanged, while (102) and (110) repeatedly decrease during charge and increase during discharge.

3.3.2. Li[Li$_{0.2}$Ni$_{0.18}$Mn$_{0.53}$Co$_{0.1}$]O$_2$/C pouch cell

As a comparison study, the structural changes of the Li[Li$_{0.2}$Ni$_{0.18}$Mn$_{0.53}$Co$_{0.1}$]O$_2$ cathode and graphite anode during first electrochemical cycle were observed. The pouch cell has a characteristic sloping region up to 4.3 V and a plateau region at 4.4 V. The charge capacity is more than 250 mAh g^{-1}, discharge capacity is more than 200 mAh g^{-1} due to irreversible capacity loss in the first cycle. The capacity before 4.3 V is more than 90 mAh g^{-1}, suggesting that most of the Co^{3+} has been oxidized to Co^{4+}.

Figure 3.3 (a)-(e) shows the charge/discharge curve with several selected ND peaks visually depicted as surface contour plots to show the peak evolution as a function time. Due to the limited amount of active materials in the beam, only the evolution of (102) peak of Li[Li$_{0.2}$Ni$_{0.18}$Mn$_{0.53}$Co$_{0.1}$]O$_2$ has been observed. Figure 3.4 (b) is the single peak refinement results for d$_{102}$ change during the first electrochemical cycle. In the slope region before 4.3 V, d$_{102}$ decreased rapidly from 2.326±0.0005Å to 2.318±0.0006Å, corresponding to the Ni^{2+}/Ni^{4+} and Co^{3+}/Co^{4+} redox reaction. As aforementioned, when Li$^+$ is extracted from the layered structure, Ni^{2+} is oxidized to Ni^{4+} and Co^{3+} is oxidized to Co^{4+} which results in a decrease in the ionic radii of these ions and a larger repulsion from

the adjacent oxygen layers. After the slope region a plateau region is observed, in this region the d_{102} spacing decreased slightly by 0.002 ± 0.0005Å. During discharge, Li^+ is reinserted into the structure, subsequently the d_{102} spacing increases monotonically. At the end of first cycle, d_{102} is 2.338 ± 0.0006Å which is larger than the pristine value. Although it is hard to distinguish how the *a-* and *c-*lattice parameters have changed after the first electrochemical cycle, it is obvious that the volume of the lattice has increased, which is consistent with previous reports.[52, 102]

Compared to the cathode, the graphite anode shows stronger peaks such as the (112), (110), (100), (004) and (006). Figure 3.3 (c)-(e) only shows the Li_xC_6 (004) and (110) peak. Since several *in-situ* ND studies have previously reported the structural changes seen with the graphite anode,[105, 117] it will not be discussed in detail here. By looking at Figure 3.3 (c)-(e), at the end of charge, the Li_xC_6 (004) peak becomes weak while LiC_6 (002) peak starts to appear, indicating a phase transformation process. The phase change process is also indicated by Li_xC_6 (110) peak, at the middle stage of charge LiC_{12} phase formed, then gradually transforms to LiC_6 phase as more Li^+ inserted into the anode. In the current cell design there is 25% excess graphite anode, so at the end of charge we should have a mixed phase between Li_xC_6 and LiC_6. Neeraj Sharma[105] also observed a two phase system at end of charge for their *in-situ* ND study on the $LiCoO_2$/C system. Figure 4 (c) shows the calculated graphite lattice parameters during the first charge/discharge process. At the beginning of the 1st charge, the *a*-parameter of the graphite anode is 2.458 ± 0.0017 Å and the *c*-parameter is

6.776±0.0004 Å (distance between carbon layers equals c/2), while at the end of charge it undergoes a phase change to LiC_6 phase coupled with a large increase in the *a-* parameter of 4.304±0.0003 Å and the c- parameter of 3.666±0.0003 Å (distance between carbon layers equals c), which is consistent with previous work.[118, 119] During discharge, as Li^+ is extracted from the graphite layer the LiC_6 phase disappeared. At the end of the discharge the a-parameter of the Li_xC_6 phase goes back to 2.462±0.0024 Å slightly larger than the pristine which is 2.458±0.0017 Å, possibly because of the irreversible Li^+ in the graphite. In another word, the structure of anode is reversible during electrochemical cycle. The ability of monitoring the dynamic structural changes in cathode and anode simultaneously is another strong merit of neutron scattering technique.

3.3.3. *Ex-situ* Neutron Diffraction on $Li[Li_{0.2}Ni_{0.2}Mn_{0.6}]O_2$

As a complementary experiment of *in-situ* neutron study of lithium-excess layered oxide material, *ex-situ* neutron diffractions were carried out on lithium-excess material $Li[Li_{0.2}Ni_{0.2}Mn_{0.6}]O_2$. Chemical delithiation was designed to simulate the charge process where a large amount of Li is extracted from the structure.

Chemical delithiation was designed to remove 0.8 mol of Li^+ from $Li[Li_{0.2}Ni_{0.2}Mn_{0.6}]O_2$ by using NO_2BF_4. After 0.4 mol of Li^+ removed from the structure, all the Ni^{2+} were oxidized to Ni^{4+}. The rest 0.4 mol Li^+ were assumed to be removed in the form of Li_2O. Neutron diffraction patterns of the pristine sample and chemically delithiated sample are shown in Figure 3.5 and refined using a

single R-3m phase. The superlattice peaks between 20–30°(2θ) can be seen in both samples. Such superstructure peaks are associated with a honeycomb ordering of Li, and transition metals in the TM layers.[97, 98] The superlattice peaks can be seen more clearly in the chemically delithiated sample. It is possible that the irreversible loss of oxygen increased the contrast between the superlattice peaks and main peaks. These peaks can not be fitted by using R-3m space group. According to previous study of layered oxides[120] , we used C/2m and $P3_112$ space groups to do the pattern matching (see Figure 3.6-3.9). By applying C/2m and $P3_112$ space group, not only these superlattice peaks, but also other peaks can be fitted, e. g. the peak at 42°. Although these peaks can be fitted using the C/2m or $P3_112$ space groups, refinement of the structural model is lacking due to large amounts of defects originating from chemical delithiation oxygen vacancies. We propose that chemical delithiation creates large amounts of site disorder as well as structural defects within the lithium-excess material that prohibit simple structural refinement using a single R-3m, C2/m or $P3_112$ space group. In order to refine the pattern quantitatively, more work has to be done to identify the suitable structure model.

Rietveld refinement of the chemically delithiated structure used a single R-3m space group excluding the superlattice range and was based on 0.4 mol Li^+ in the structure ($Li_{0.4}Ni_{0.2}Mn_{0.6}O_{1.8}$). After delithiation, the lattice parameter a decreased 0.008 Å, while the lattice parameter c increased 0.0141 Å due to Ni oxidation from Ni^{2+} to Ni^{4+} causing increased repulsion between the adjacent oxygen layers. These changes are not as large as previous reports possibly due

to the presence of other phases existing as defects as evidenced by the group of superlattice peaks. The large amounts of Li^+ vacancies as well as the increased *c-* lattice spacing facilitate Ni interlayer migration accounting for the increase from 3.27% to 6.67% following delithiation. Furthermore, Rietveld refinement also identified 20% oxygen deficiency in the single R-3m phase model. These vacancies created in the oxygen layers enable Li/Ni cation migration by hopping through nearby vacancies. Refinement of the neutron pattern of the delithiated structure identified the formation of tetrahedral Li^+ sites. The use of chemical delithiation combined with neutron diffraction proves to be a powerful method to identify structural changes which correlate to those proposed from electrochemical delithiation.[121, 122]

3.4. Conclusion

In this work, a lab pouch cell was designed for *in-situ* Neutron diffraction in order to study two high capacity cathode materials in the layered oxides family: classical layered oxide $LiNi_{1/3}Mn_{1/3}Co_{1/3}O_2$ and lithium excess layered oxide $Li[Li_{0.2}Ni_{0.18}Mn_{0.53}Co_{0.1}]O_2$. By using a single peak refinement technique, structural changes of these two materials are observed quantitatively. Li excess layered oxide $Li[Li_{0.2}Ni_{0.18}Mn_{0.53}Co_{0.1}]O_2$ shows an irreversible volume expansion after the first cycle which is most likely caused by oxygen loss from the structure, while classical layered oxide $LiNi_{1/3}Mn_{1/3}Co_{1/3}O_2$ retains the reversible structure in the electrochemical voltage window. Anisotropy in the *a-* and *c-* lattice directions are observed. *Ex-situ* neutron diffraction experiments on lithium-excess material

also reveal irreversible changes of structure after chemical delithiation. Major efforts are currently underway to improve the *in situ* neutron scattering data quality to enable full Rietveld refinement of atomic positions. In addition to having the ability to monitor the dynamic changes in the cathode, our setup allows for the simultaneous observation of the anode material. Our observation shows a phase transformation in the anode at end of charge and start of discharge. The reversible change of structure and phase transformation shows good reversibility performance of the graphite anode.

Chapter 3, in part, is a reprint of the material "In-situ neutron diffraction study of the $xLi_2MnO_3.(1-x)LiMO_2$ (x= 0, 0.5; M= Ni, Mn, Co) layered oxide compounds during electrochemical cycling" as it appears in the Journal of Power Sources, Haodong Liu, Christopher R. Fell, Ke An, Lu Cai, Ying Shirley Meng, Journal of Power Sources, 2013, 240, 772. The dissertation author was the primary investigator and author of this paper. All experiments and data analysis were performed by the author except for the *ex-situ* neutron powder diffraction data collection.
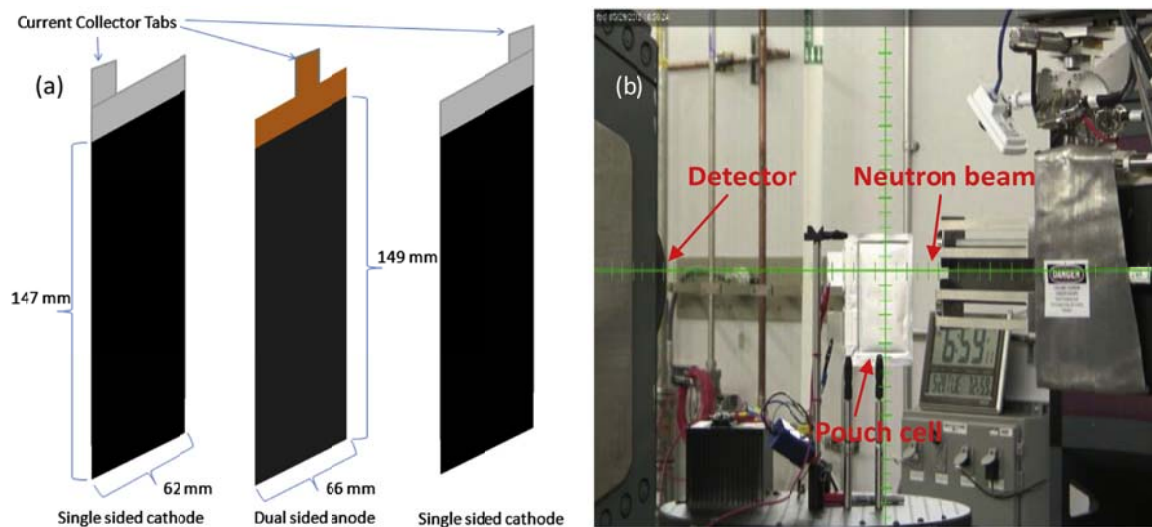
Figure 3.1   (a) Simple schematic of lab made pouch cell for *in-situ* neutron diffraction study; (b) Pouch cell installed on VULCAN beamline.
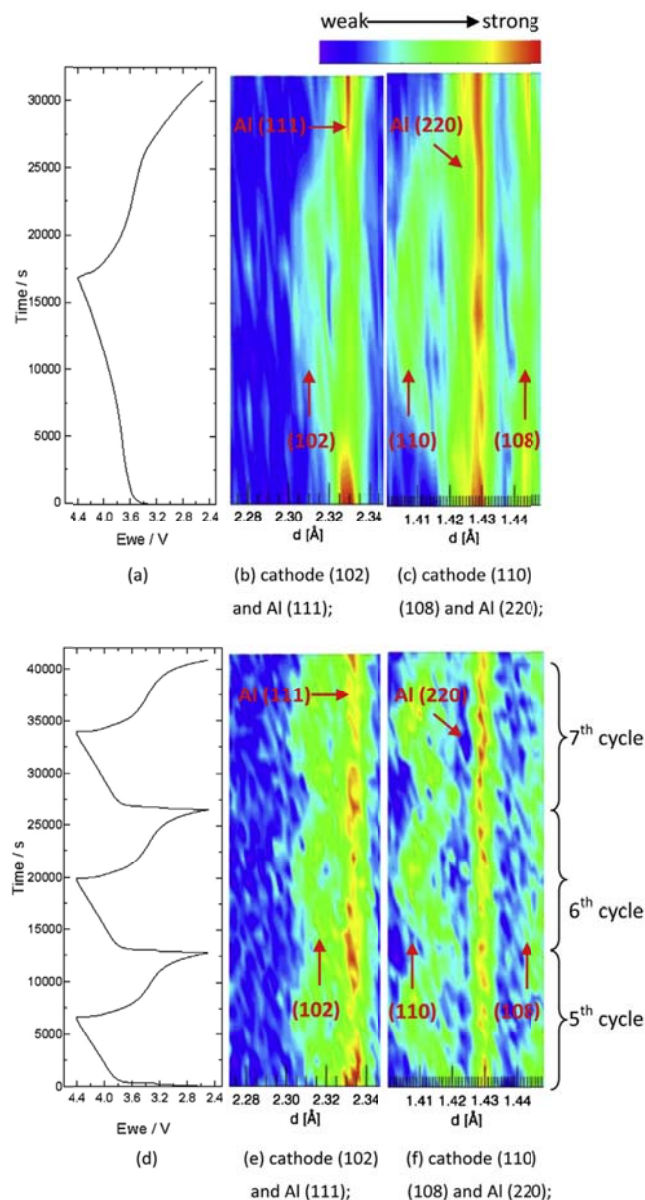
Figure 3.2 (a) 1st cycle charge/discharge curve of Li[Ni$_{1/3}$Mn$_{1/3}$Co$_{1/3}$]O$_2$ and surface contour plots of (b)-(c) 1st cycle Li[Ni$_{1/3}$Mn$_{1/3}$Co$_{1/3}$]O$_2$ (102), (110) and (108); (d) 5-7th cycles charge/discharge curve of Li[Ni$_{1/3}$Mn$_{1/3}$Co$_{1/3}$]O$_2$ and surface contour plots of (e)-(f) 5-7th cycles Li[Ni$_{1/3}$Mn$_{1/3}$Co$_{1/3}$]O$_2$ (102), (110) and (108) Neutron Diffractions.
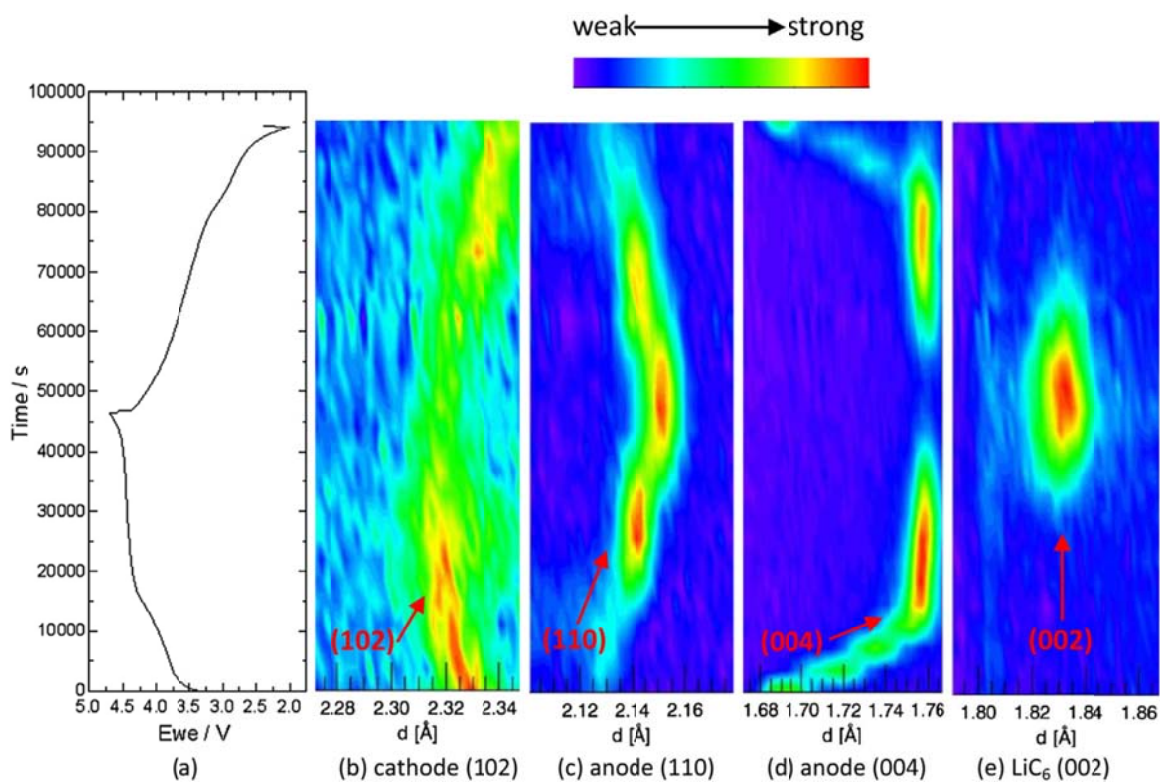
Figure 3.3 (a) 1st cycle charge/discharge curve of Li[Li$_{0.2}$Ni$_{0.18}$Mn$_{0.53}$Co$_{0.1}$]O$_2$ and surface contour plots of (b) Li[Li$_{0.2}$Ni$_{0.18}$Mn$_{0.53}$Co$_{0.1}$]O$_2$ (102); (c) Li$_x$C$_6$ (110); (d) Li$_x$C$_6$ (004); (e) LiC$_6$ (002) Neutron Diffractions.
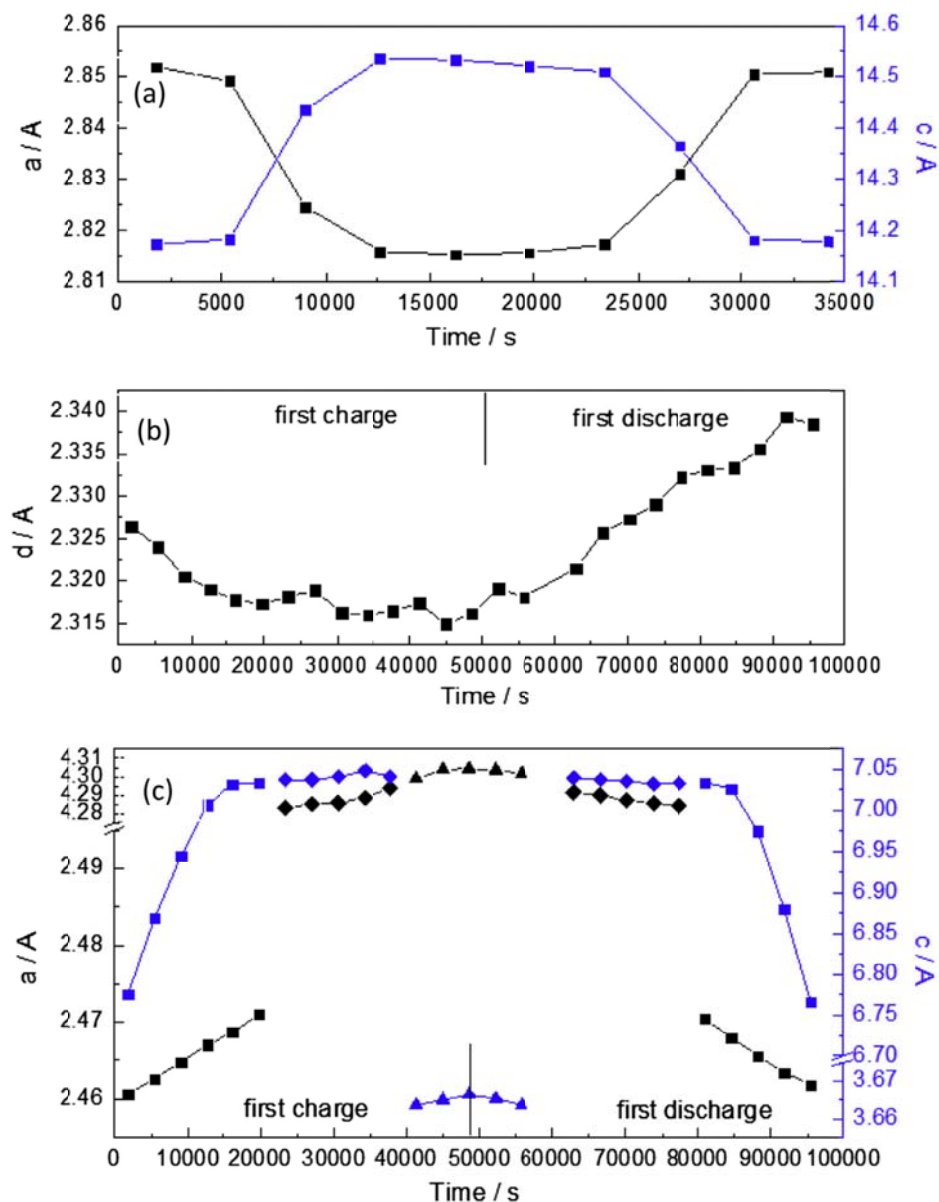
Figure 3.4 (a) Cathode Li[Ni$_{1/3}$Mn$_{1/3}$Co$_{1/3}$]O$_2$ lattice parameters change during 1st cycle, black is the a-parameter, blue is the c-parameter; (b) Li[Li$_{0.2}$Ni$_{0.18}$Mn$_{0.53}$Co$_{0.1}$]O$_2$ (102) d-spacing change during 1st cycle; (c) anode graphite lattice parameter change during 1st cycle, black is the a-parameter, blue is the c-parameter, the square is the Li$_x$C$_6$ phase, the diamond is the LiC$_{12}$ phase, the triangle is the LiC$_6$ phase.
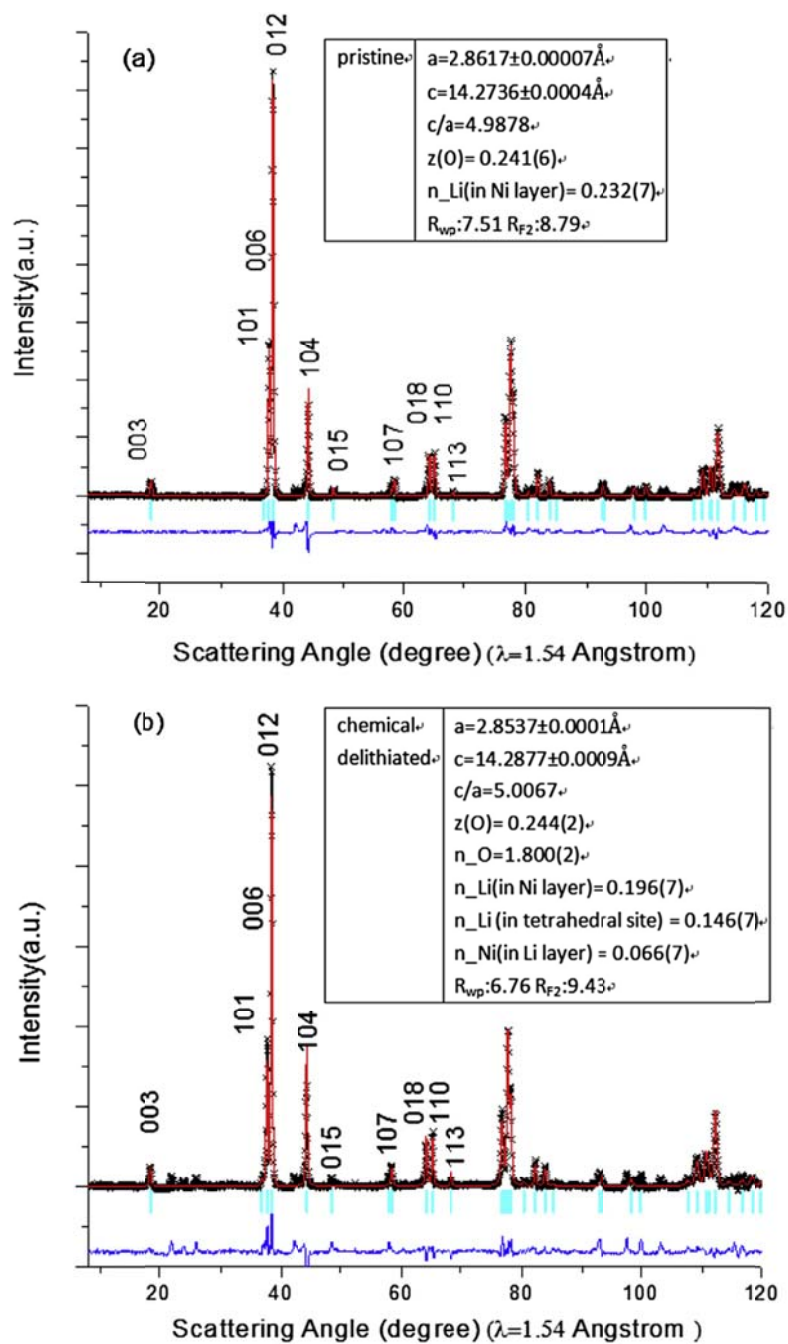
Figure 3.5 *Ex-situ* Neutron Diffraction patterns and Rietveld Refinement results: (a) pristine $Li[Li_{0.2}Ni_{0.2}Mn_{0.6}]O_2$; (b) chemically delithiated sample $Li_{0.4}Ni_{0.2}Mn_{0.6}O_{1.8}$.
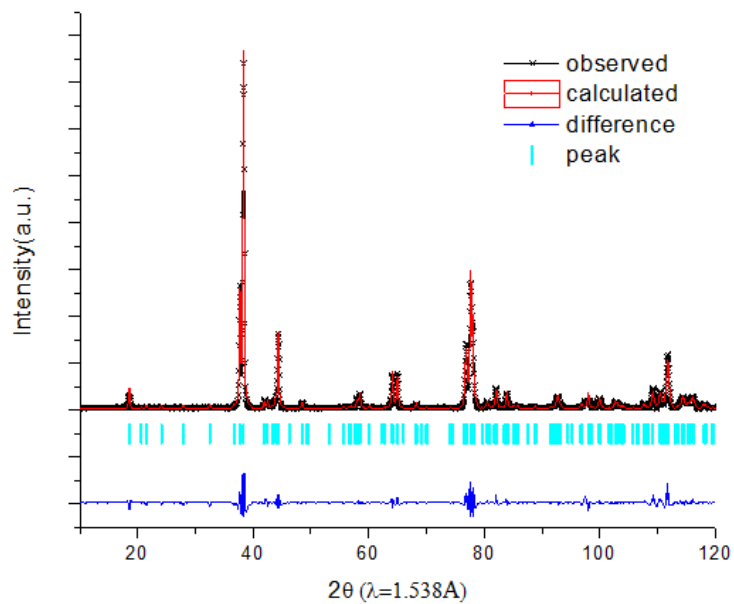
Figure 3.6 *Ex-situ* neutron diffraction patterns and profile matching with C/2m space group result of pristine Li[Li$_{0.2}$Ni$_{0.2}$Mn$_{0.6}$]O$_2$.
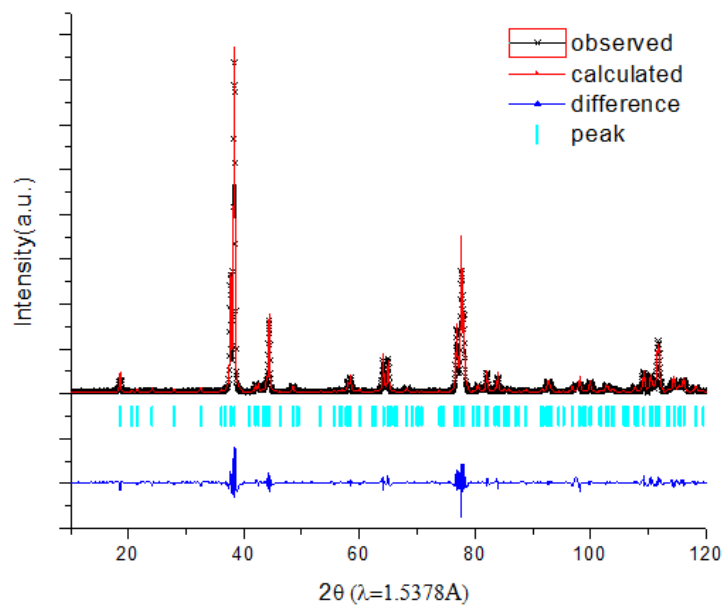
Figure 3.7   *Ex-situ* neutron diffraction patterns and profile matching with $P3_112$ space gourp result of pristine $Li[Li_{0.2}Ni_{0.2}Mn_{0.6}]O_2$.
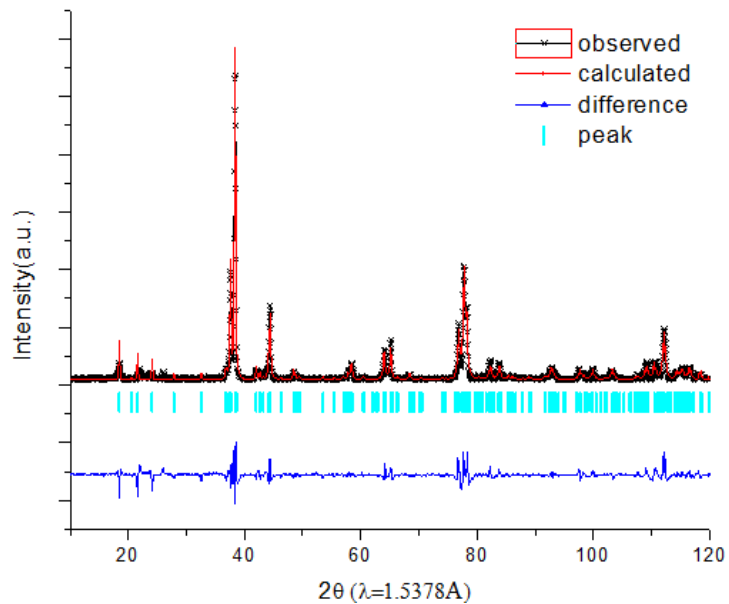
Figure 3.8 *Ex-situ* neutron diffraction patterns and profile matching with C/2m space gourp result of chemically delithiated sample $Li_{0.4}Ni_{0.2}Mn_{0.6}O_{1.8}$.
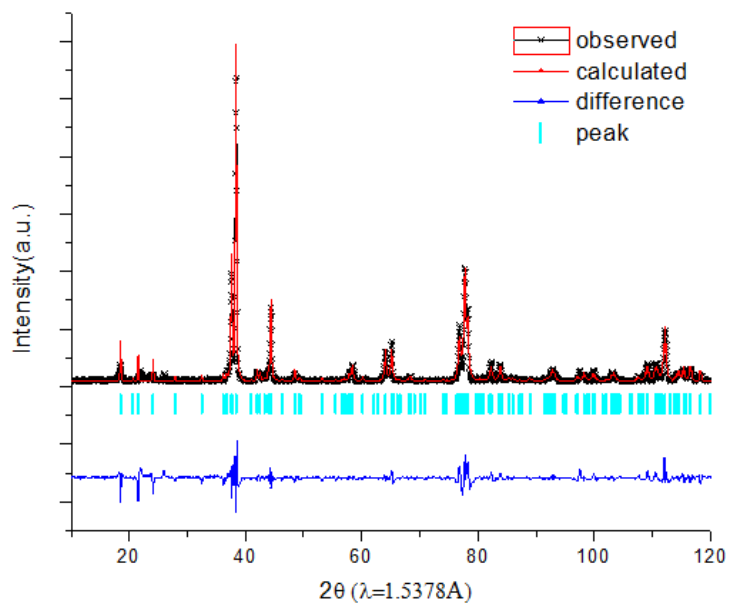
Figure 3.9 *Ex-situ* neutron diffraction patterns and profile matching with $P3_112$ space gourp result of chemically delithiated sample $Li_{0.4}Ni_{0.2}Mn_{0.6}O_{1.8}$.

Chapter 4. *Operando* Lithium Dynamics in The Li-Rich Layered Oxide

Cathode Material via Neutron Diffraction

Neutron diffraction under *operando* battery cycling is used to study the lithium and oxygen dynamics of high Li-rich Li[Li$_{x/3}$Ni$_{(3/8-3x/8)}$Co$_{(1/4-x/4)}$Mn$_{(3/8+7x/24)}$]O$_2$ (x=0.6, HLR) and low Li-rich Li[Li$_{x/3}$Ni$_{(1/3-x/3)}$Co$_{(1/3-x/3)}$Mn$_{(1/3+x/3)}$]O$_2$ (x=0.24, LLR) compounds that exhibit different degrees of oxygen activation at high voltage. The measured lattice parameter changes and oxygen position show largely contrasting changes for the two cathodes where the LLR exhibits larger movement of oxygen and lattice contractions in comparison to the HLR that maintains relatively constant lattice parameters and oxygen position during the high voltage plateau until the end of charge. DFT calculations show in the presence of oxygen vacancy during the high voltage plateau, changes in the lattice parameters and oxygen position are consistent with experimental observations. Lithium migration kinetics for the Li-rich material is observed under *operando* conditions for the first time to reveal the rate of lithium extraction from the lithium layer and transition metal layer are related to the different charge and discharge characteristics. At the beginning of charging, the lithium extraction predominately occurs within the lithium layer. Once the high voltage plateau is reached, the lithium extraction from the lithium layer slows down and extraction from the transition metal layer evolves at a faster rate.

4.1. Introduction

The progressive advancements in communication and transportation has changed human daily life to a great extent.[123] With the birth of the secondary lithium ion battery, the past few decades have moved mobile devices and personal computer devices from novelty to an almost essential necessity in order to function in a modern day society. While important advancements in battery technology has come since its first demonstration, the high energy demands needed to electrify the automotive industry have not yet been met with the current technology.[8, 124, 125] One considerable bottleneck is the cathode energy density.[8, 124, 125] The lithium layered oxides utilize transition metal redox pairs for charge/discharge compensation during lithium extraction and intercalation offering a theoretical capacity of 270 mAh g^{-1} for complete lithium extraction.[8, 125, 126] However, practical capacities have so far shown to be ~200 mAh g^{-1} due to degradation reactions and large lattice contractions at low lithium content, limiting its capability to meet future demands. One possible cathode material are the Li-rich layered oxide compounds $xLi_2MnO_3 \cdot (1-x)LiMO_2$ (M= Ni, Mn, Co) (0.5=<x=<1.0) that exhibit capacities over 280 mAh g^{-1} obtainable by the combination of the typical transition metal redox pair with the additional oxygen redox reaction as the charge compensation mechanism.[53, 127, 128] In this class of compounds, lithium ions can reside in both lithium layer and transition metal layer of close packed oxygen framework, typical from O3 type layered oxides like $LiCoO_2$. Large irreversible capacities are often observed in these materials due

to irreversible oxygen loss or side reactions stemming for the electrolyte.[66] It has been also observed using *ex-situ* NMR that lithium reinsertion back into the transition metal layer is little to none.[51] Several different lithium extraction/insertion sites and migration pathways are available, where lithium may be extracted from lithium or transition metal layers and lithium from octahedral coordinated sites to tetrahedral sites to form Li-Li dumbbells.[47] However, these studies have not revealed the dynamic process of lithium migration for the Li-rich material under *operando* electrochemical cycling conditions.

Neutron scattering has several distinct advantages for battery studies: 1) The sensitivity of neutron to light elements such as lithium and oxygen are significant in order to determine their position in the crystal structure; 2) Compares to the X-ray, the neutron shows larger scattering contrast between neighboring elements in the periodic table specifically the scattering lengths, e.g. for transition metals in this case: Ni, 10.3 fm; Mn, -3.73 fm; Co, 2.49 fm; and 3) The deep penetration capability of neutron allows simultaneous observation of the cathode and anode. However, challenges exist in broadening the application of *operando* neutron diffraction for Li-ion batteries research. First, limited by the generation reactions of neutrons, the neutron flux is usually several orders of magnitude lower than X-rays. In another words, longer acquisition times as well as larger amounts of samples are required for neutron diffraction experiments. In addition, the existence of hydrogen, which has a large incoherent neutron-

scattering cross-section, is detrimental to the signal-to-noise ratio of neutron diffraction pattern. Separators (polyethylene based porous membrane) and poly carbonate based electrolyte solutions contain a considerate amount of hydrogen. These two major reasons pose significant challenges to *operando* neutron diffraction for lithium ion battery research although it is such a powerful technique for light elements like lithium.[43] Several groups designed special strategies to overcome these problems. Novak et al. designed large electrochemical cells with special configuration to guarantee enough active material expossure to the incident neutron beam.[129, 130] Sharma used expensive deuterated electrolytes to minimize the noise from hydrogen.[131] Vadlamani selected single crystal (100) Si sheets as casing material, which improved signal-to-noise ratio relative to other casing materials.[132]

In order to gain more in-depth insights about the lithium (de-)intercalation mechanisms in Li-rich layered oxides, track particularly the lithium ions in transition metal layer, *operando* neutron diffraction experiments were designed to quantitatively observe lithium migration in this type of oxides during the electrochemical process. In this study, we use amorphous silicon as an anode for the neutron diffraction battery design in order to avoid any overlap of signal that may be associated with the anode material. We perform *operando* neutron diffraction to probe lithium and oxygen for a high Li-rich (HLR), $Li[Li_{x/3}Ni_{(3/8-3x/8)}Co_{(1/4-x/4)}Mn_{(3/8+7x/24)}]O_2$ (x = 0.6) material, and low Li-rich (LLR), $Li[Li_{x/3}Ni_{(1/3-x/3)}Co_{(1/3-x/3)}Mn_{(1/3+x/3)}]O_2$ (x = 0.24) material with varying degrees of the high

voltage plateau. In conjunction with the *operando* neutron diffraction, density functional theory (DFT) calculations were used to explore the incorporation of dilute oxygen vacancy, its affect on the lattice mechanics and oxygen positions. We also observe site-dependent lithium migration taking place during different stage of charging/discharge processes. To our knowledge, this is the first time differentiation of lithium migration has been observed and identified during battery operation for this class of materials. Furthermore, this work demonstrates the potential of investigating dynamic changes of light elements in large format (10-100 times larger format than the typical operando cells for synchrotron X-ray diffraction) prismatic and cylindrical batteries under realistic cycling condition via *operando* neutron diffraction method.

4.2. Experimental Section

Material: HLR and LLR cathode materials was generously provided by Envia Systems. The materials were synthesized via a co-precipitation route and details are provided elsewhere.[133-135] Inductively coupled plasma atomic emission spectroscopy (ICP-AES) was used to determine the composition of lithium and transition metal of the HLR and LLR cathode materials. Those data were then used as initial parameters for the Rietveld refinement of the neutron diffraction patterns.

Cell Design: The cells were designed and assembled in a dry room at Envia's fabrication facility. The cell includes 12 pieces of dual sided anode (graphite or amorphous silicon) and Li-rich layered cathode. This cell

configuration & design aims at increasing the loading of active materials in our pouch cells to increase neutron diffraction pattern statistics. A Celgard separator is used to alternatively cover the anode and cathode on each side. The electrolyte solution composed of 1 M $LiPF_6$ in a 1:1 ethylene carbonate (EC):diethyl carbonate (DEC). The cathode is composed of 92% active material, 4% PVDF and 4% carbon black on an aluminum current collector.

Operando Neutron Diffraction **:** A Bio-Logic SP-300 potentiostat was used to electrochemically cycle the cell under constant charge and discharge currents. The $Li[Li_{x/3}Ni_{(3/8-3x/8)}Co_{(1/4-x/4)}Mn_{(3/8+7x/24)}]O_2$ (x = 0.6, HLR) / Si pouch cell was charged at 80 mA (~ C/15) to 4.7V then discharged at -80 mA to 1.5 V. The $Li[Li_{x/3}Ni_{(1/3-x/3)}Co_{(1/3-x/3)}Mn_{(1/3+x/3)}]O_2$ (x = 0.24, LLR) / Si pouch cell was charged at 80 mA (~ C/15) to 4.7V then discharged at -120 mA to 1.5 V (~ C/10). The time of fight (TOF) powder neutron diffraction data were collected on the VULCAN beamline at the Spallation Neutron Sources (SNS) in the Oak Ridge National Laboratory (ORNL).[110] An incident beam (5mm*12mm) of 0.7 to 3.5 Å bandwidth allowing 0.5~2.5 Å d-space in diffracted patterns in the ±90° 2θ detector banks was selected using the double-disk choppers at 30 Hz speed. High intensity mode was employed with Δd/d ~0.45%. The SNS power was at nominal 1100KW.[110] Time stamped neutron event data were collected while the cells were under continuous cycling. Neutron diffraction data were sliced and reduced by the VDRIVE software.[111] Full pattern Rietveld refinement was performed using the GSAS programs with the EXPGUI interface.[112, 114]

The *operando* neutron diffraction data were sliced every 3600s or 7200s and reduced by the VDRIVE software.[111] Multi-phase Rietveld refinement was carried out to analyze the structure evolution of Li-rich cathode as a function of state of charge. The multi-phase refinement model include Li-rich cathode,[43, 136] cathode current collector Al, and anode current collector Cu. The texture and crystal structure of Al and Cu were optimized for the first data set and subsequently fixed in the following data. In each data set, the lattice parameters, lithium occupancies, and oxygen positions are refined. The weight profile factor R_{wp} is usually < 1.31%.

Computation Methods: The first principles calculations were performed in the spin polarized GGA approximations to the Density Functional Theory (DFT). Core electron states were represented by the projector augmented-wave method[137] as implemented in the Vienna ab initio simulation package (VASP).[138, 139] The Perdew-Burke-Ernzerhof exchange correlation [140] and a plane wave representation for the wavefunction with a cutoff energy of 450 eV were used. The Brillouin zone was sampled with a dense kpoints mesh by Gamma packing.

4.3. Results and discussions

4.3.1. Neutron diffraction battery device and electrode materials

Figure 4.1 (a) shows the *operando* neutron diffraction experiment set up. The incident neutrons are continuously scattered by the pouch cell during constant current charge / discharge. The scattered neutrons are recorded by the detectors in real time. A thick pouch cell with twelve layers was designed to

increase the amount of cathode material in the scattering volume, which achieves better signal than the previous single layer cell.[43] Figure 4.2 shows *operando* neutron diffraction plots of LR / graphite cell and for the HLR / Si cell during charge (5 hours charging data). For the graphite cell, the evolution of peaks from the cathode and anode show several overlapping Bragg peaks of graphite and LR. The refinement and challenges of LR / graphite cell is detailedly described in the support information. We redesigned the multi-layered pouch cell by replacing the graphite anode with an amorphous silicon anode. For the HLR / Si cell, the evolution of (110), (108), (107), (104), (102), and (006) peaks from cathode can be clearly distinguished when compared to the LR / graphite cell.

Multi-phase Rietveld refinement of the neutron pattern of pouch cell, considering LR,[43] graphite anode,[109, 141] cathode current collector Al,[142] and anode current collector Cu was performed.[143] The refined pattern of LR / graphite cell before the electrochemical cycling is displayed in Figure 4.3, the strong scattering from graphite anode apparently lowers the contribution of the cathode signal to the neutron pattern. In addition, there are some peaks from the cathode overlapping with graphite peaks at < 1.3 Å d-spacing region. The graphite anode also undergoes a complicated phase transformation during charge/ discharge, which will introduce two more phases to the refinement.[109] Those factors will reduce the reliability of refined structure for cathode with increasing floating parameters, limiting refinement of atom occupancy and position.

Figure 4.1 (b) and 4.1 (c) show the refined patterns of the HLR and LLR / Si cell before any electrochemical cycling where no signal from anode is

observed and the weight profile factor R_{wp} is reduced. Table 4.1 compares the refinements results of the HLR and LLR cathode batteries before cycling. For the purpose of comparison, the R$\bar{3}$m layered structure was used for the refinement of the HLR and LLR. The Li/Ni mixing was found to be 4.5(7)% in HLR, which is slightly higher than LLR that showed 2.6(6)%.

4.3.2. Lattice dynamics and lattice oxygen evolution during battery charge and discharge

Figure 4.4 (a) and (b) shows the charge/ discharge voltage profile of HLR and LLR / Si cell, respectively, which was charged to 4.7 V at constant current of 80 mA, then discharged to 1.5 V at 80 mA and 120 mA (discharge at higher current due to the limited beamtime), respectively. The HLR / Si full cell shows a typical voltage profile of the Li-rich material that includes three distinct regions described as followed: 1) a slope region < 4.3 V that is predominately the Ni $^{2+/4+}$ redox pair, 2) a plateau region > 4.3 V that involves the simultaneous extraction of oxygen and lithium where oxygen participates in the charge compensation mechanism, and 3) A single slope during the first discharge that is a combination of transition metal redox pairs and oxygen participation.[67, 144-146] Based on the capacity, there are 0.865 Li$^+$ extracted out from HLR cathode at end of charge, and 0.562 Li$^+$ inserted back after discharge. Due to the low efficiency of Si anode, the first cycle coulombic efficiency of this full cell is 64.4%. The LLR / Si full cell shows a longer slope region due to high nickel content and shorter pateau region compared to the HLR / Si full cell. There are 0.942 Li$^+$ extracted out from LLR

cathode at the end of charge, and 0.617 Li^+ inserted back after discharge, leading to a 65.4% first cycle coulombic efficiency that is comparable to the HLR / Si cell.

The lattice parameters of both cells are plotted in Figure 4.4 (a) and 4.4 (b), respectively. Before charge, the *a* and *c* lattice parameters of HLR are 2.8465(2) Å and 14.217(2) Å, respectively. During the slope region, Li^+ is extracted from the layered structure while Ni^{2+} and Co^{3+} are oxidized to Ni^{4+} and Co^{4+}, and that causes the ionic radii to decrease (e.g. r Ni^{2+}=0.69Å, r Ni^{3+}=0.60Å, r Ni^{4+}=0.48Å), leading to a rapid contraction of the *a* lattice parameter to 2.8265(3) Å (0.70% smaller than OCV state).[43] The refined oxygen positions were plotted in Figure 4.5 (a) in red circles. The oxidation of TM ions increased the electrostatic attraction between the TM ions and oxygen ions that decreases the bond length of TM-O. On the other hand, the removal of Li^+ introduces a concentration gradient and electrostatic repulsion from adjacent oxygen layers accounting for the increasing of *c* lattice parameter to 14.381(4) Å (1.15% larger than OCV state). As a comparison, the *a* lattice parameter of LLR decreased 1.16% from 2.8481(2) Å to 2.8150(3) Å, and the *c* lattice parameter of LLR increased 1.65% from 14.227(2) Å to 14.462(3) Å. The larger changes of lattice parameters of LLR after the slope region is caused by the higher concentration of TM ions having been oxidized.

All the TM ions stay in their highest oxidation state without further oxidation during the plateau region, which causes the *a* lattice parameter remaining relatively constant. The oxygen position is also observed to be

constant in this plateau region indicating the TM ions do not participate in the charge compensation process during this plateau region. With the Li^+ continuously being extracted, out of expectations, the c lattice parameter of HLR decreased slightly to 14.346(5) Å (0.24% smaller than end of slope) at the charged state. However, the c lattice parameter of LLR dramatically decreased to 14.206(4) Å (1.77% smaller than end of slope) at the charged state even beyond the pristine state. The contraction of c lattice parameter is less severe or delayed in HLR compared to the LLR as a result of the higher degree of oxygen activity as indicated by the longer high voltage plateau, which is consistent with previous *in-situ* X-ray studies.[121, 144, 147]

The first principles calculations were performed to gain more insight to the changes in lattice parameters[148] and oxygen positions. The supercell is composed of twelve-formula units of $Li[Li_{1/6} Ni_{1/6}Co_{1/6}Mn_{1/2}]O_2$. For the convenience to interpret the delithiation in computation, the formula of this compound will be written in the form of $Li_{14/12}Ni_{2/12}Co_{2/12}Mn_{6/12}O_2$. As shown in Figure 4.5, oxygen ions are close-packed and stacked in ABCABC (O3) stacking, while TM layers and lithium layers stack alternatively in the octahedron sites. The cation ordering in TM layer is plotted in Figure 4.5, each Li^+ is surrounded by 5 Mn^{4+} and 1 Co^{3+}. The lattice parameters and oxygen positions are calculated as a function of lithium content in the structure. The range of $Li_{14/12}$ to $Li_{8/12}$ corresponds to the slope region, and $Li_{8/12}$ to $Li_{6/12}$ corresponds to the plateau region. The computational results show a decrease of a lattice parameter and oxygen position, while the c lattice parameter expands during the slope region.

Thus, the trend of the lattice parameters and oxygen position is consistent with the experimental results in this region. However, the computational results shows discrepancy from experimental results where a continuous change in the lattice parameters and oxygen position at the plateau region. We created an dilute oxygen vacancy (1/24) model and simulated the delithiation from $Li_{8/12}Ni_{2/12}Co_{2/12}Mn_{6/12} \square_{1/12}O_{23/12}$ to $Li_{6/12}Ni_{2/12}Co_{2/12}Mn_{6/12} \square_{1/12}O_{23/12}$. The computational results for the oxygen vacancy model are in good agreement with the the experimental results showing constant lattice parameters and little oxygen movement during the high voltage plateau region.

As Li^+ is inserted back to HLR cathode during discharge, the *a* lattice parameter increased monotonically to 2.8497(4) Å, which is 0.11% larger than the pristine state. The increase of the *a* lattice parameter and elongation of TM-O bond are caused by the reduction of TM ions during discharge. The changes of *c* lattice parameter changes during discharge are complex, which increased at first then decreased to 14.323(5) Å (0.75% larger than OCV state). The trends in the lattice parameters as function of the state of charge for HLR are quite consistent with previous *in-situ* XRD studies.[147] Similar to the HLR, both *a* and *c* lattice parameters of LLR suffered irreversible changes after the first cycle, the *c* lattice parameter become 14.336(5) Å (0.77% larger than OCV state). However, the *a* lattice parameter increased monotonically only to 2.8408(5) Å during discharge, which is 0.26% smaller than the pristine state. This changes in *a* lattice parameter show little discrepancy with previous study. We ascribe this to the low efficiency of Si anode, which limited the amount of lithium inserts back to the LLR.

To our best knowledge, this *operando* neutron study to investigate the lattice dynamics and lattice oxygen evolution in a full cell configuration is reported for the first time.

4.3.3. *Operando* observation of path-specific lithium migration

Based on the R$\bar{3}$m layered structure, there are two different lithium sites within Li-rich layered oxide. Most of the Li$^+$ is located within the lithium layer, while the excess amount of Li$^+$ stay within TM layer as indicated by the refinement results for HLR and LLR before cycling. As shown in Figure 4.6 (a), during the slope region, the Li$^+$ in lithium layer is observed to be extracted out with little to no extraction from the TM layer. A similar trend was also observed for LLR in Figure 4.6 (b). DFT calculations was carried out to verify the experimental observations by comparing the energies of removing different Li$^+$. At fully lithiated state, the results from calculations showed that the extraction of Li$^+$ from TM layer will consume more energy (0.5505 eV / uniter cell) than the removal of Li$^+$ from the lithium layer.

During the first charge plateau region, Li$^+$ was observed to be extracted from both the lithium layer and TM layer. Based on the reported experimental and computational studies, A certain amount of tetrahedral Li would likely form during this plateau.[47, 77] These tetrahedral site lithium will block Li$^+$ from going back to the TM layer. As a sequence, when Li$^+$ inserts back to Li-rich layered oxide during discharge, all the Li$^+$ goes back to the lithium layer. After the first cycle, the lithium content in HLR TM layers irreversibly decreased to 0.069(78)

(29% of its OCV state) and 0.035(68) (33% of its OCV state) for LLR. Similar results have been reported by NMR spectroscopy,[51, 76] it is found very few Li^+ can be intercalated back into the TM layer after being charged at high voltages.

The Li^+ extraction / insertion rates of both HLR and LLR during different regions in their first charge / discharge were calculated and the detailed results are listed in Table 4.2. At the beginning of charging, the rate of lithium extraction within lithium layers for the slope region is 8.08×10^{-4} atoms min^{-1} and 7.75×10^{-4} atoms min^{-1} for HLR and LLR, respectively. Li^+ extraction rate within the TM layer for this region is relatively slow in comparison with 0.333×10^{-4} atoms min^{-1} and 0.075×10^{-4} atoms min^{-1} for HLR and LLR, respectively. The corresponding rate of change of the a and c lattice parameters are -4.83×10^{-5} and 3.90×10^{-4} Å min^{-1} for HLR and -4.67×10^{-5} and 3.26×10^{-4} Å min^{-1} for the LLR. Interestingly, in the plateau region for HLR, the rate of Li^+ extraction decreases in the lithium layer to 5.85×10^{-4} atoms min^{-1} and increases in the TM layer to 2.22×10^{-4} atoms min^{-1}. Similarly, for LLR in the plateau region, The extraction rate within the lithium layer also slows down slightly to 6.93×10^{-4} atoms min^{-1} and increases to 1.10×10^{-4} atoms min^{-1} from the TM layer. The corresponding rate of change in the a lattice parameter for HLR and LLR are relatively small ($\sim 10^{-6}$ Å min^{-1}) for the plateau region while the c lattice parameter rates within the plateau region are -5.67×10^{-5} and -5.92×10^{-4} Å min^{-1} for the HLR and LLR, respectively. The extraction rate of Li^+ in transition metal layer in HLR is two times that of LLR and the decrease in rates for HLR and LLR within the lithium layer are to 27.6 % and 8%, respectively. As previous computation study has indicated, the

existence of oxygen vacancies lowers the diffusion barriers for cations in TM layer.[149] Over the entire charging region, the total Li extraction rate is similar for both HLR and LLR. The differences in the total lithium extraction between the slope and plateau region for the two materials is related to the different charging compensation mechanisms that dominate the respective regions. For LLR, the slope region, where the transition metal redox pair reaction ($Ni^{2+/4+}$ and $Co^{3+/4+}$) occurs, is the dominant mechanism extracting a total of ~0.57 Li. In comparison, the plateau region for LLR, where oxygen is involved, ~0.35 Li is extracted. For HLR where oxygen involvement is more dominant, the slope region has a total of ~0.36 Li while the plateau region has a total of ~0.49 Li extracted. Considering the relatively higher Ni content in the LLR (0.253) versus the HLR (0.15), the length of the slope region is appropriate. The region specific extraction rate of Li^+ in the TM layer for both the LR materials and the computation results may suggest that the formation of oxygen vacancy can facilitate the migration of lithium from the transition metal layer or possibly migration of lithium to tetrahedral sites. In any case, the migration behavior of the two Li-rich materials show that the rate of lithium extraction and re-insertion for the slope, plateau, and discharge regions during electrochemical cycling is path-dependent.

4.4. Conclusion

Operando neutron diffraction on a high Li-rich and low Li-rich cathode were performed during battery operation using a custom 1 Ah pouch battery with amorphous silicon to isolate structural changes for the cathode. Evolution of the

lattice parameters and oxygen position revealed large lattice contractions occuring for the low Li-rich cathode and a largely delayed change in the high Li-rich cathode at higher voltages. Lithium dynamics were observed and quantified. It is revealed for the first time that lithium migration rates at different sites are highly dependent on the different voltage regions that exhibit different battery characteristics. First, the extraction of lithium at the slope region is largely dominated by migration within lithium layers. During the plateau region, lithium migration within lithium layers slows down and migration from the transition metal layer occurs. Upon discharge, lithium from the transition metal layer is largely irreversible with only lithium reinsertion occuring within lithium layers. These results provide new insights into the lithium migration behavior in lithium rich layered oxides and demonstrate the unique capabilities to observe light elements in the bulk under *operando* conditions via neutron diffraction.

Chapter 4, in part, is a reprint of the material "Operando Lithium Dynamics in the Li-Rich Layered Oxide Cathode Material via Neutron Diffraction" as it appears in the Advanded Energy Materials, Haodong Liu, Yan Chen, Sunny Hy, Ke An, Subramanian Venkatachalam, Danna Qian, Minghao Zhang, Ying Shirley Meng, Advanced Energy Materials, 2016, 1502143. The dissertation author was the primary investigator and author of this paper. All experiments and data analysis were performed by the author except for the material preparation and cell making.
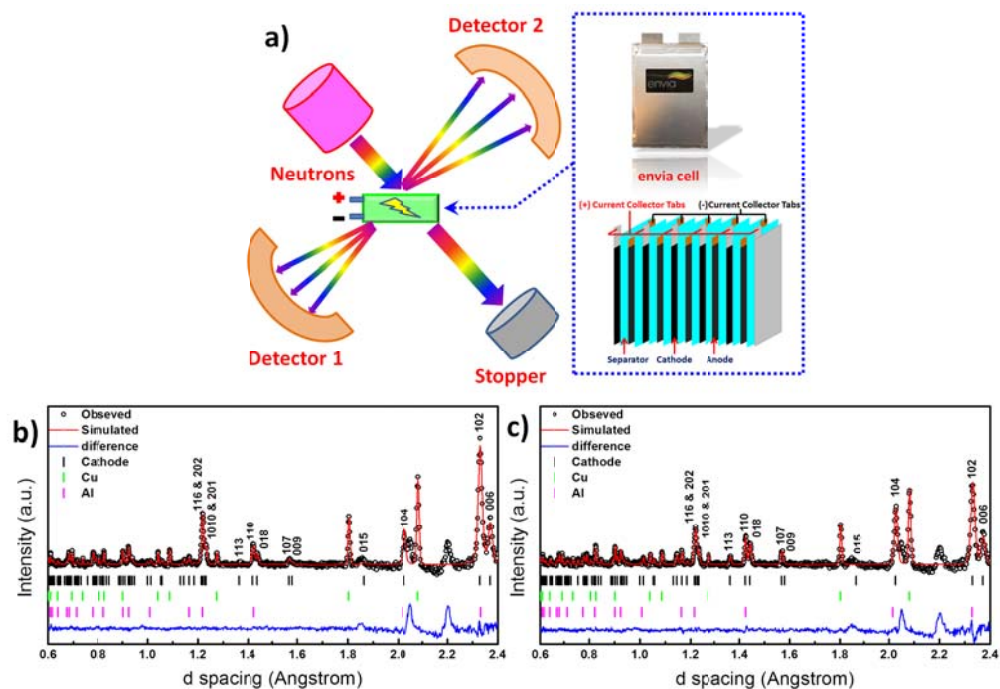
Figure 4.1 (a) schematic of the operando neutron diffraction study and the pouch cell. (b) refined diffraction pattern of HLR / Si cell and (c) LLR / Si cell at the open circuit potential state.
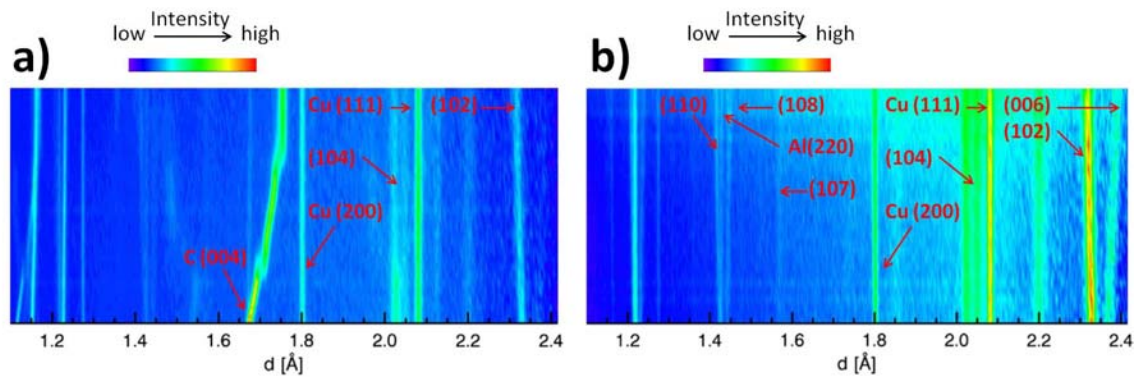
Figure 4.2 Neutron diffraction contour plots of (a) LR / graphite cell and (b) for the HLR / Si cell during charge (5 hours charging data).
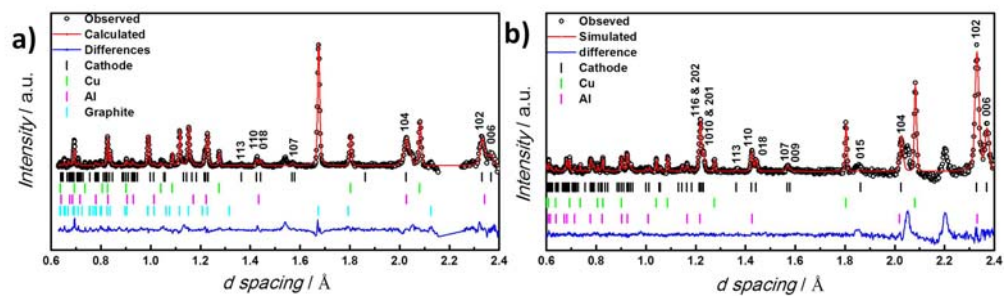
Figure 4.3 Refined diffraction pattern of (a) LR / graphite cell and (b) HLR / Si cell at the open circuit potential state.
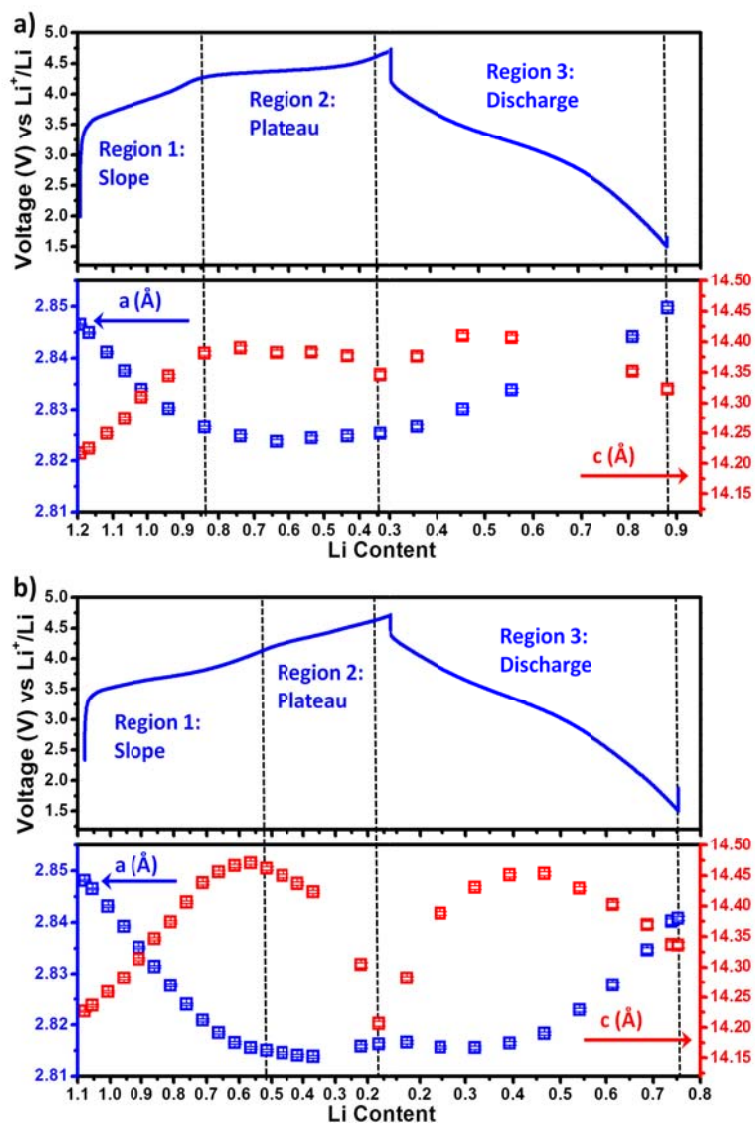
Figure 4.4 Electrochemical charge/discharge profile with corresponding lattice parameters at different states of delithiation/lithiation for (a) HLR and (b) LLR.
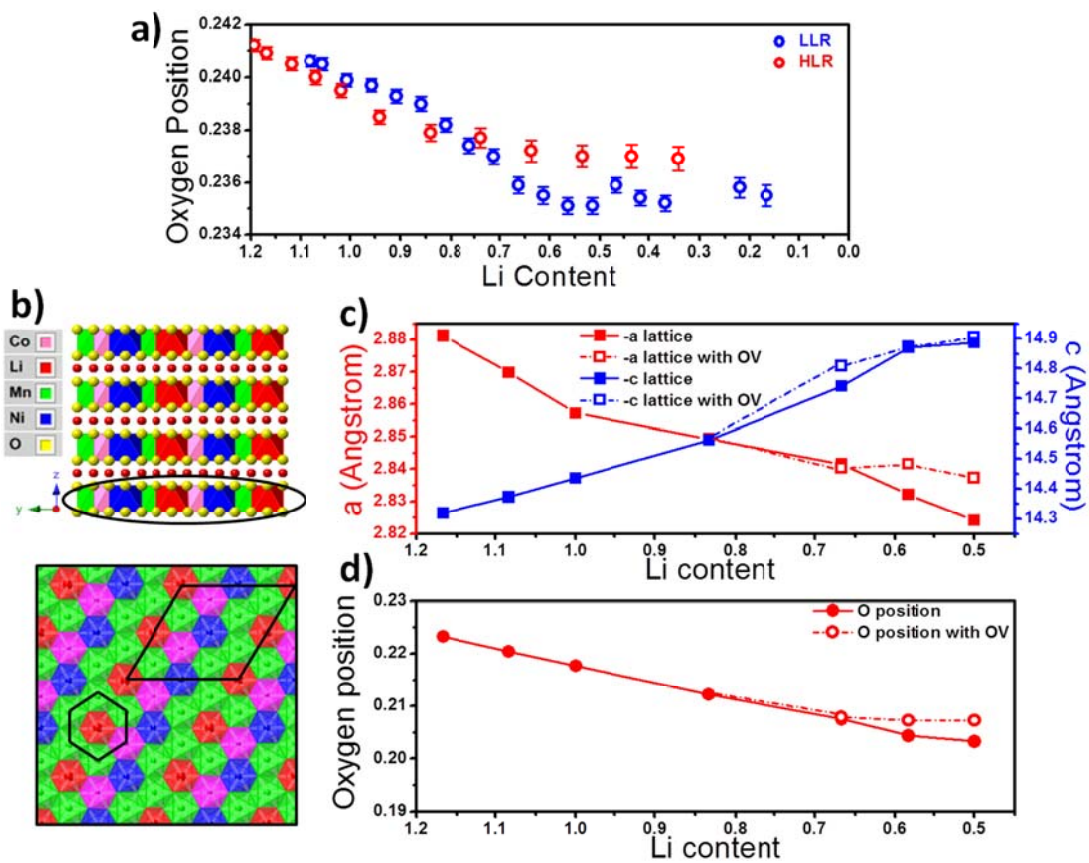
Figure 4.5 (a) oxygen position from refinement results, (b) the cation ordering in TM layer used for DFT calculations, (c) DFT results of the evolution of the lattice parameters and (d) oxygen position with and without oxygen vacancy.
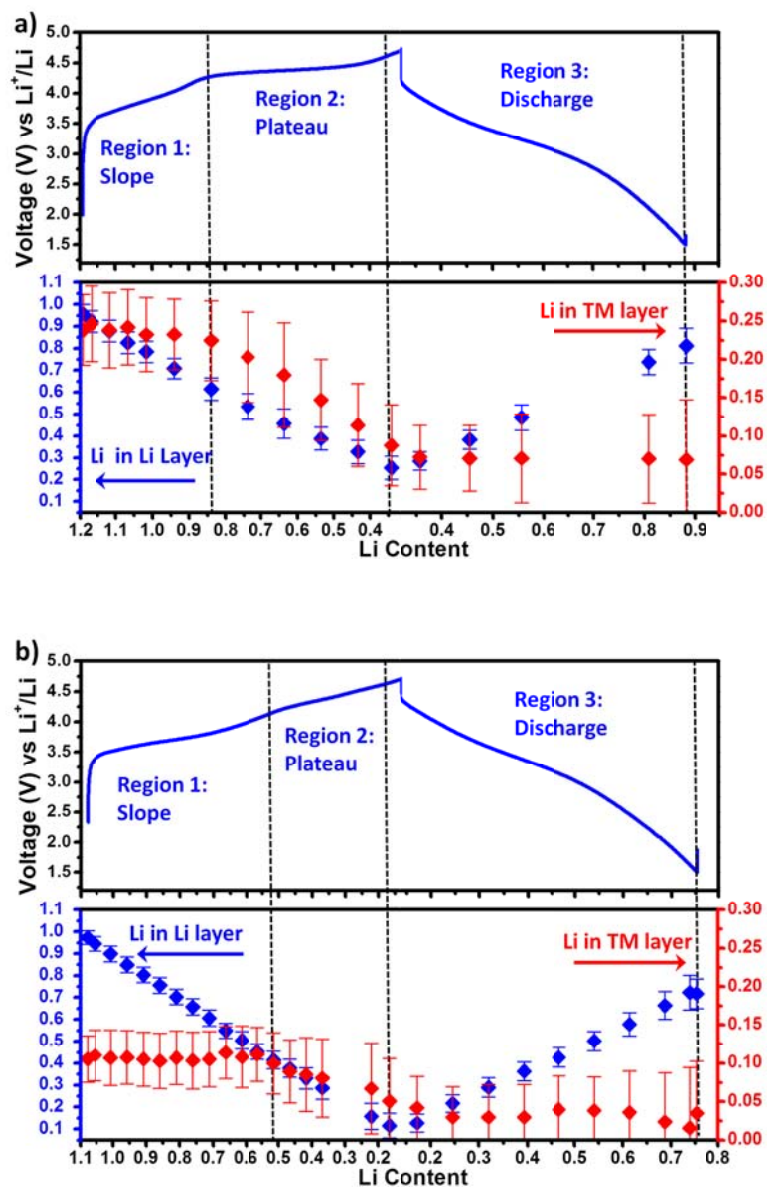
Figure 4.6 Electrochemical charge/discharge profile with corresponding lithium occupancy at different states of delithiation/lithiation for (a) HLR and (b) LLR.

Table 4.1 Refinement results of the HLR (top)[a] and LLR (bottom)[b] batteries at the open circuit potential state.

	a_{hex} (Å)	c_{hex} (Å)	Li/Ni mixing	oxygen coordinates	R_{wp} (%)	χ^2
HLR	2.8465(2)	14.217(2)	0.045(7)	0.2412(2)	1.20	1.70
LLR	2.8481(2)	14.227(2)	0.026(6)	0.2406(2)	1.06	1.40

Table 4.2   Lithium extraction rate based on different regions during electrochemical charging.

site	Electrochemical Charge region	C-rate (C=250 mAh g^{-1})	Extraction / Insertion rate (atoms/min)
Li$_{TM}$(HLR)	Slope	C/15	0.333×10^{-4}
Li$_{Li}$(HLR)	Slope	C/15	8.08×10^{-4}
Li$_{TM}$(HLR)	Plateau	C/15	2.22×10^{-4}
Li$_{Li}$(HLR)	Plateau	C/15	5.85×10^{-4}
Li$_{TM}$(HLR)	Discharge	C/15	-
Li$_{Li}$(HLR)	Discharge	C/15	8.42×10^{-4}
Li$_{TM}$(LLR)	Slope	C/15	0.075×10^{-4}
Li$_{Li}$(LLR)	Slope	C/15	7.75×10^{-4}
Li$_{TM}$(LLR)	Plateau	C/15	1.10×10^{-4}
Li$_{Li}$(LLR)	Plateau	C/15	6.93×10^{-4}
Li$_{TM}$(LLR)	Discharge	C/10	-
Li$_{Li}$(LLR)	Discharge	C/10	1.17×10^{-3}

Chapter 5. Understanding the Role of NH$_4$F and Al$_2$O$_3$ Surface Co-Modification on Lithium-excess Layered Oxide Li$_{1.2}$Ni$_{0.2}$Mn$_{0.6}$O$_2$

In this work we prepared Li$_{1.2}$Ni$_{0.2}$Mn$_{0.6}$O$_2$ (LNMO) using a hydroxide co-precipitation method and investigated the effect of co-modification with NH$_4$F and Al$_2$O$_3$. After surface co-modification, the first cycle coulombic efficiency of Li$_{1.2}$Ni$_{0.2}$Mn$_{0.6}$O$_2$ improved from 82.7% to 87.5%, and the reversible discharge capacity improved from 253 mAh g^{-1} to 287 mAh g^{-1} at C/20. Moreover, the rate capability also increased significantly. A combination of neutron diffraction (ND), high-resolution transmission electron microscopy (HRTEM), aberration-corrected scanning transmission electron microscopy (a-STEM) / electron energy loss spectroscopy (EELS), and X-ray photoelectron spectroscopy (XPS) revealed the changes of surface structure and chemistry after NH$_4$F and Al$_2$O$_3$ surface co-modification while the bulk properties showed relatively no changes. These complex changes on the material's surface include the formation of an amorphous Al$_2$O$_3$ coating, the transformation of layered material to a spinel-like phase on the surface, the formation of nanoislands of active material, and the partial chemical reduction of surface Mn^{4+}. Such enhanced discharge capacity of the modified material can be primary assigned to three aspects: decreased irreversible oxygen loss, the activation of cathode material was facilitated with pre-activated Mn^{3+} on the surface, and stabilization of the Ni redox pair. These

insights will provide guidance for the surface modification in high voltage cathode battery materials of the future.

5.1. Introduction

To meet the requirements for electric vehicles (EVs), better cathode materials with higher energy density and longer cycle life have to be developed. The Li-excess layered oxide compounds, $xLi_2MnO_3 \cdot (1-x)LiMO_2$ (M= Ni, Mn, Co), are one potential class of cathode materials due to their high energy density and relatively lower costs.[150] Despite the fact that Li-excess materials may exhibit reversible discharge capacities greater than 280 mAh g^{-1} (almost twice the practical capacity of $LiCoO_2$),[94, 144, 151] there are several inherent material issues that limit its practical application. The first one is the large irreversible capacity observed in the first cycle, which lowers the initial coulombic efficiency. Secondly, the rate capability does not satisfy high power applications. However, the most serious concern is the severe capacity and voltage degradation after long cycles, which results in a significant decrease in energy density.[152]

In order to remediate these issues several surface modification methods have been applied to the cathode particles to decrease potential side reactions between electrode and electrolyte, such as HF etching and the formation of undesirable products within the solid-electrolyte interface (SEI) film.[101] The most widely used surface modification materials are oxides, fluorides, and phosphates, for example, TiO_2, Al_2O_3, AlF_3, and $AlPO_4$. [46, 153, 154] However, most of these materials are intrinsically electronic semiconductors or insulators. Learning from

the case of LiFePO$_4$, carbon and Al have been used as a coating layer in order to improve the electronic conductivity of the material.[155, 156] Other researchers have introduced an ionic conductor to the surface of Li-excess, such as, lithium phosphorus oxynitride (LiPON), LiNiPO$_4$, and Li$_3$VO$_4$.[157-160] Manthiram et al. combined the advantages of different surface modifications and developed hybrid strategies. One of their recent works combined reduced graphene oxide and AlPO$_4$, which largely suppressed undesired SEI formation.[161] In contrast to the studies mentioned above, Thackeray et al. demonstrated that a mild acid treatment can also reduce the first cycle irreversible capacity of Li-excess layered oxides.[162]

Although these surface modifications improved the electrochemical performance of Li-excess, the fundamental role in terms of their chemical and structural effects, are still not well understood. In this work, we prepared Li-excess layered oxide with composition of Li$_{1.2}$Ni$_{0.2}$Mn$_{0.6}$O$_2$ (LNMO) using a routine hydroxide co-precipitation method. A mild acid, NH$_4$F, and metal precipitant, Al^{3+}, were used together to modify the surface of Li-excess. Our analysis focuses on a mechanistic study aimed to determine the reasons for the electrochemical enhancement. First, the bulk crystal structures and morphologies of these materials were examined. Then, a series of surface sensitive characterizations were carried out to investigate the chemical and structural changes after surface co-modification. The combination of electrochemical analyses and physical characterization enabled us to explain how the NH$_4$F and Al$_2$O$_3$ surface co-modification improved the initial coulombic efficiency, rate

capability, and changed cycling stability of Li-excess. These findings help us understand the working mechanisms of surface modifications which will shed lights on designing reasonable surface modifications for high voltage cathode materials in the future.

5.2. Experimental Methods

5.2.1. Synthesis and surface modification

A co-precipitation reaction, followed by two-step calcination was used for the synthesis of the Li-excess layered oxides.[43, 65] Transition metal (TM) nitrates, $Ni(NO_3)_2 \cdot 6H_2O$ (ACROS Organics, 99%), and $Mn(NO_3)_2 \cdot 4H_2O$ (Alfa Aesar, 98%) were dissolved into deionized water, then titrated into $LiOH \cdot H_2O$ (Fisher) solution. The precipitated TM hydroxides were then subjected to vacuum filtration and washed three times with deionized water. The collected TM hydroxides were dried in an oven at 180°C for 10 h in air. The dried TM precursors were then mixed with a stoichiometric amount of $LiOH \cdot H_2O$ (Fisher). This mixture was ground for 30 min to ensure adequate mixing and then placed into a furnace at 480°C for 12 h. Later, the pre-calcined powders were calcinated at 900 °C for 12 h in air, to achieve the final product.

The procedure for preparing NH_4F and Al_2O_3 surface co-modified Li-excess (NALNMO) was adapted from work by Zheng et al.[46] The specific amounts of NH_4F and Al^{3+} in this work were 3 mol% and 1 mol% of the $Li_{1.2}Ni_{0.2}Mn_{0.6}O_2$ powders, respectively. To prepare NH_4F and Al_2O_3 surface co-modified $Li_{1.2}Ni_{0.2}Mn_{0.6}O_2$ powders, NH_4F (Aldrich, 99.99%) and $Al(NO_3)_3 \cdot 9H_2O$

(Aldrich, 99.997%) were separately dissolved in deionized water. Firstly, the $Li_{1.2}Ni_{0.2}Mn_{0.6}O_2$ powders were dispersed into the aluminum nitrate solution by continuous magnetic stirring at the controlled temperature of 80°C. Then, the NH_4^+ solution was slowly dropped into the solution, followed by a slow evaporation of solvent. The obtained precursor was heated at 400°C in a tube furnace for 5 h under the flow of nitrogen gas.

5.2.2. Neutron diffraction

The time-of-fight (TOF) powder neutron diffraction data were collected at the VULCAN instrument at Spallation Neutron Sources (SNS), Oak Ridge National Laboratory (ORNL).[110] Around 0.6 g of powder was filled into a vanadium sample can. An incident beam (5mm×12mm) of 0.7 to 3.5 Å bandwidth, allowing 0.5~2.5 Å d-space in the diffracted pattern of the ±90° 2θ detector banks, was selected using the double-disk choppers at 30 Hz frequency. High resolution mode was employed with Δd/d ~0.25%. The SNS was at nominal, 1100KW, power.[110] Powder neutron diffraction data were collected in high resolution mode for a duration of 3 h and processed using VDRIVE software.[111] Full pattern Rietveld refinement was performed to extract the structure parameters using GSAS software with EXPGUI interface.[112, 114]

5.2.3. Scanning electron microscopy

The particle morphology and size distribution of the synthesized powders were determined using an FEI XL30 ultrahigh-resolution scanning electron

microscope (UHR SEM) system with a Sirion column, which enables very high-resolution imaging at low acceleration voltage. All images were collected under an accelerating voltage of 15 kV. The powders were suspended on double-sided carbon tape, placed on a specimen holder.

5.2.4. High-resolution transmission electron microscopy

HRTEM images were collected using an FEI Tecnai G2 Polara cryoelectron microscope with a field emission gun and a voltage of 300 kV. The powders were suspended on a 300-mesh copper grid with lacey carbon.

5.2.5. Electrochemical test

Electrochemical properties were measured using an Arbin battery cycler in galvanostatic mode between 4.8 and 2.0 V. Cathodes were prepared by mixing the active material, LNMO or NALNMO, with 10 wt % Super P carbon (TIMCAL) and 10 wt % poly(vinylidene fluoride) (PVDF) in N-methylpyrrolidone (NMP, 99% extra pure, ACROS Organics). The slurry was cast onto an Al foil using a doctor blade and dried in a vacuum oven overnight at 80 °C. The electrode discs were punched and dried again at 80 °C for 6 h before storing them in an argon filled glovebox (O_2, H_2O level < 1 ppm). 2016-type coin cells were used to electrochemically cycle LNMO and NALNMO to different cycles. The coin cells were prepared in the same argon-filled glovebox using lithium metal ribbon as anode and 1 M $LiPF_6$ in ethylene carbonate/dimethyl carbonate (EC:DMC in 1:1 vol ratio) electrolyte solution (Novolyte). Celgard model C480 (Celgard Inc., USA)

were used as the separator. The loading of active material was around 3.7 mg cm^{-1} for both LNMO and NLNMO. Multiple cells were electrochemically tested to confirm reproducibility.

The cycled samples were recovered by disassembling cycled batteries in an argon-filled glovebox. The cathode was washed with DMC 3 times and then allowed to dry in argon atmosphere overnight. The cathodes were transferred to the XPS chamber using an airtight vacuum transfer system. For TEM samples, the powders were suspended on a copper grid with lacey carbon. The approximate time of sample exposed to air (from a sealed environment to the microscope column) was less than 5 s.

5.2.6. X-ray photoelectron spectroscopy

Surface chemistry was probed using a PHI 3056 X-ray photoelectron spectrometer equipped with a dual Al Kα (1486.7 eV) and Mg Kα (1256.6 eV) anode source, operated at 350 W, and with sample chamber pressure below 10^{-8} Torr. Samples were dissembled in an Ar-filled glovebox, rinsed with a small quantity of anhydrous DMC (Sigma-Aldrich), and transferred to the XPS chamber using an airtight vacuum transfer system. High-resolution scans were acquired using a pass energy of 23.5 eV and an energy step of 0.05 or 0.075 eV. Survey scans were measured using pass energy of 93.5 eV and a 0.5 eV energy step. The binding energies were calibrated by setting the hydrocarbon C1s (C-C, C-H) signal to 284.6 eV, which corresponds mainly to the carbon black in the composite electrode and adventitious carbon. C signal was measured before and

after any other signal to precisely calibrate the energy scale. The data were analyzed using CasaXPS software and all peaks were fit using a Shirley-type background.

5.2.7. *a*-STEM/EELS

Electron microscopy work was carried out on a Cs corrected FEI Titan 80/300-kV TEM/STEM microscope, equipped with a Gatan Image Filter Quantum-865. All STEM images and EELS spectra were acquired at 300 kV and with a beam size of ~0.7 Å. EELS spectra shown in this work were acquired from a square area of ~0.5 ×0.5 nm using an acquisition time of 2 s and a collection angle of 35 mrad. High angle annular dark field (HAADF) images were obtained at a convergence angle of 30 mrad and a large inner collection angle of 65 mrad. Images acquired by an HAADF detector with a small convergence angle and a relatively large inner collection angle are also called "Z-contrast" images, where the contrast is proportional to $Z^{1.7}$.[163, 164]

To minimize possible electron beam irradiation effects, EELS and HAADF figures presented in this work were acquired from areas without pre-beam irradiation. Mn L_3 to L_2 intensity ratio analysis was performed using the method described by Wang et al.[165]

5.3. Results

5.3.1. Bulk crystal structure and morphology characterization

Figure 5.1 represents the SEM images of the LNMO and NALNMO. Both materials show secondary particles with a wide size distribution, ranging from 1μm to 10 μm; the primary particle size distribution ranges from 80 nm to 150 nm. The SEM images show no morphology or particle size difference between LNMO and NALNMO. The presence of Al was confirmed using EDS, which is shown in Figure 5.2.

Due to the low scattering cross section of lithium in X-ray scattering, neutron diffraction was carried out on both LNMO and NALNMO powders in order to carefully investigate their crystal structures.[166] Figure 5.3 shows the neutron diffraction and Rietveld refinement of both samples. The major diffraction peaks of these two materials are indexed according to the parent hexagonal structure with R$\bar{3}$m space group. The patterns indicate that both samples adopt a well-layered structure with little Li/Ni mixing, as evidenced by the existence of doublets at (006)/(012) and (018)/(110). [167, 168] No obvious changes were observed in these peaks after NH_4F and Al_2O_3 surface co-modification, indicating that the layered phase is well maintained. In addition, there are no extra peaks observed in NALNMO.

Table 5.1 lists the summary of Rietveld refinement results. The lattice parameters of LNMO are a = 2.8615(1) Å and c = 14.2580(6) Å, which are in good agreement with our previous XRD studies.[122] The refined oxygen position of the pristine material is (0, 0, 0.2417(7)), and there is 3.7(4) % Ni in the Li layer. As a comparison, the lattice parameters of NALNMO surface co-modified material are a = 2.8623(1) Å and c = 14.2621(6) Å, which are only slightly larger

(< 0.03%) than those of the LNMO. The oxygen position after NH_4F and Al_2O_3 surface co-modification is unchanged at (0, 0, 0.2416(7)), and there is slightly more Ni^{2+} in the Li layer, which is 3.9(4) %. In summary, the neutron diffraction study shows that the surface co-modification by NH_4F and Al_2O_3 does not change the bulk structure of $Li_{1.2}Ni_{0.2}Mn_{0.6}O_2$; the layered O3 structure is well maintained after the surface modification. The process introduces only slight changes in the material's lattice parameters and Li/Ni interlayer mixing.

5.3.2. Electrochemical performance

Figure 5.4 (a) compares the first charge/discharge voltage profiles of LNMO and NALNMO within the voltage window of 2 - 4.8 V, at 12.5 mA g^{-1} (C/20). The surface modified sample shows the same characteristic profile, with a sloping region (to 4.4 V) corresponding to the oxidation of nickel from Ni^{2+} to Ni^{4+}, followed by the oxidation of oxygen from the lattice during the voltage plateau region.[100, 122, 144, 169] Even without deducting the weight of non-active Al_2O_3 in NALNMO, the surface modified material still shows higher charge and discharge specific capacity than the pristine material. After NH_4F and Al_2O_3 surface co-modification, charge and discharge capacities are increased from 306 ± 6 mAh g^{-1} to 328 ± 4 mAh g^{-1}, and from 253 ± 2 mAh g^{-1} to 287 ± 6 mAh g^{-1}, respectively, as well as coulombic efficiency from 82.7% to 87.5%. More importantly, the irreversible capacity was reduced from 53 ± 8 mAh g^{-1} (~17%) to 41 ± 10 mAh g^{-1} (~12%). It is interesting and surprising that the NALNMO electrodes shows a longer plateau region, which is related to either oxygen loss

and/or the oxidation of lattice oxygen,[100, 169] while the observed irreversible capacity decreases.

Figure 5.4 (b) and 5.4 (c) represent the discharge profiles of both materials subject to different rates, from 12.5 mA g^{-1} (C/20) to 500 mA g^{-1} (2C); the charge current remained 12.5 mA g^{-1} in all cases. The NALNMO electrode delivered higher discharge capacity than LNMO at all testing rates. Even at 500 mA g^{-1} current density, the surface modified material still shows a discharge capacity as high as 181 mAh g^{-1}.

The long-term cycling performance of both materials were compared by charging and discharging each at a current density of 25 mA g^{-1} (C/10), which is represented in Figure 5.5. The NALNMO electrode exhibits higher discharge capacity in early cycles, but becomes similar to the pristine material after 80 cycles. The capacity difference between the two materials after 80 cycles is only 8 mAh g^{-1}, which is much smaller than the 44 mAh g^{-1} of the first cycle. The voltage decay upon cycling exists in both materials, but is slightly better in NALNMO, which is described in more detail below.

The discharge voltage profiles and corresponding dQ/dV plots of both materials upon cycling are shown in Figure 5.6. By comparing their dQ/dV, we can better understand how the capacity and voltage decay occur in each material. From those plots, we can clearly see three peaks during discharge. The 1st peak is above 4.0V, the 2nd peak sits between 3.5 - 4.0V, and the 3rd peak is below 3.5V. The 1st and 2nd peaks are a result of Ni^{4+} to Ni^{2+}, and possible oxygen reduction.[45, 145, 169, 170] The 3rd peak, on the other hand, is considered to be a

combination of Mn^{4+} to Mn^{3+} and oxygen reduction as a result of Li insertion back into the bulk structure, as several authors have previously reported.[70, 144, 145, 150] By comparing Figure 5.6 (b) and 5.6 (d), we can see that the 3rd peak area of pristine material is much smaller than that of the modified material. The changes that occur in that peak over 80 cycles are quite distinct for each material as well. Whereas the 3rd peak area of LNMO exhibits a continuous increase during cycling, the NALNMO peak area only increases during the initial 10 cycles. In contrast to the pristine material, the 3rd peak area of modified material continues to decrease after 10 cycles. Another major difference is that the 2nd peak of NALNMO remains relatively stable throughout cycling. Though it decreases in magnitude, its position remains constant. The 2nd peak of LNMO not only decreases in area, but also shifts to lower voltage and loses its prominence. The voltage fade in this region is demonstrated in Figure 4b as well. The 1st peak area of LNMO continuously decreases during cycling, and shifts towards lower voltage. On the other hand, the peak area of NALNMO increases during the first 10 cycles, then decreases thereafter. Its peak position decreases, but not by as much as LNMO, as it remains much more narrow. The NH_4F and Al_2O_3 surface co-modification stabilized the 1st and 2nd peak regions, a detailed understanding of these phenomena will be discussed later.

5.3.3 Surface structure and chemical species characterization

Neutron diffraction and SEM analysis demonstrated that the crystal structure and particle morphology of both materials were quite similar, however,

they exhibited large differences in electrochemical performance. Advanced techniques, such as HRTEM, a-STEM/EELS, and XPS were carried out to investigate the surface structure and chemistry of both materials in more detail.

High-resolution transmission electron microscopy was used to identify the Al_2O_3 coating on surface modified material. Figure 5.7 (a) and 5.7 (b) present HRTEM images of LNMO and NALNMO, respectively. The TEM images of both materials show very good layered crystal structure. Amorphous films are observed on the surface of NALNMO, while the LNMO shows a very clean surface. More than 20 particles were analyzed to examine the amorphous film. As shown in Figure 5.7 (b), this amorphous film is unevenly coated on the surface, with thickness ranging from 0 nm to 2.5 nm. As our recent study indicates, the surface chemistry of LNMO varies with different preparation methods.[66] We also applied the same NH_4F and Al_2O_3 surface co-modification on LNMO prepared using a carbonate synthesis method,[66] and interestingly the formed Al_2O_3 coating exhibited a uniform coating of 1 nm thickness, as shown in Figure 5.8. This shows that surface modifications and treatments have a degree of dependency of the specific synthesis route for even the same materials. It would be of great interest to explore this dependence further. In addition to the amorphous coating, there are isolated nanoislands sitting on the surface of particles, as illustrated in Figure 5.7 (c), which are not observed in our pristine $Li_{1.2}Ni_{0.2}Mn_{0.6}O_2$. Figure 6d depicts the TEM image of these nanoislands at higher magnification. They exhibit a well-layered crystal structure with particle size around 20 nm. EELS was performed on the isolated nanoislands to verify that

they were active material instead of Al-related compounds, as shown in Figure 5.9.

Figure 5.10 depicts the differences between the bulk and surface structure of NALNMO. Multiple grains were selected for study and the results were consistent; therefore, only representative data are shown here. Shown in Figure 5.10 (a) the atomistic surface structure of the NALNMO, however, is distinct from the bulk region, with extra bright spots in the lithium layer. In order to better visualize the different, fast Fourier transform (FFT) was carried out from both bulk (red square) and surface (blue square) as illustrated. The extra spots in FFT images from the surface (Figure 5.10 (c)) indicate a spinel-like structure compared to the pure layered structure of the bulk (Figure 5.10 (b)). The atomic model insets in Figure 5.10 (d) and 5.10 (e) better illustrate the contrast differences. The spinel-like phase on the surface is around 3nm thickness after the co-modification.

In addition to direct visualization of the crystal structure changes, EELS was carried out to obtain chemical information. Two representative NALNMO particles were observed and studied. One consists of C2/m phase, measured along the (10-1) zone axis; this electron diffraction pattern is represented by the inset of Figure 8a. The other is R$\bar{3}$m phase measured along the (010) zone axis, which is presented in Figure 5.11 (d). EELS was performed on NALNMO from bulk to surface, using a step size of ~1nm; the region of analysis is represented by the red rectangles in Figure 5.11 (a) and 5.11 (d). The L_3 and L_2 edges of transition metals are due to the electronic excitation from the $2p^{3/2}$ to $3d^{3/2}$ and

$3d^{5/2}$ orbitals and from the $2p^{1/2}$ to $3d^{3/2}$ orbital, respectively. Previous studies have shown that the L_3/L_2 ratio is sensitive to the valence state of Mn.[171, 172] The L_3/L_2 ratio, plotted as a function of distance from surface to bulk, are shown in Figure 5.11 (b) and 5.11 (e). The L_3/L_2 edge ratios of both particles reveal that the Mn oxidation state remains 4+ in the bulk, as it does in pristine LNMO.[122] However, the C2/m domain particle (Figure 5.11 (a)) shows Mn oxidation state reduced to 3+ within a 3 nm region of the surface. The corresponding O K-edge of bulk and surface are plotted in red and purple, respectively. The pre-peak in the O K-edge is due to the transition of 1s electrons to the unoccupied 2p orbitals, which hybridize with the TM 3d orbitals. The decrease in the pre-peak intensity of the C2/m domain particle agrees with the evidence that Mn at the surface is reduced.[169] The EELS study shows that the surface Mn in C2/m region getting pre-activated.

While STEM-EELS were used to examine small local regions, XPS was performed on soaked and cycled samples in order to investigate the overall chemical changes on the surface upon cycling. Figure 5.12 shows Ni 3p and Mn 3p XPS spectra of both LNMO and NALNMO after soaking in electrolyte, after 1 cycle, and after 10 cycles. The Mn 3p peak is composed of two components, with the main signal ~49.7 eV assigned to Mn^{4+} and a weaker signal at lower binding energy ~48.5 eV related to Mn^{3+}.[173] The relative percent of these components are given in Table 5.2. These results illustrate that soaking electrodes in the electrolyte will induce the formation of Mn^{3+}, even without charge/discharge. Before cycling, NALNMO shows almost three times more Mn^{3+} at the surface

than LNMO. The degree of Mn^{3+} is shown to continuously increase upon cycling for both materials. At any given cycle, however, the degree of Mn^{3+} is consistently greater for modified material, compared to the pristine. Figure 5.13 shows each material's Mn 3s regions. The difference in binding energy between those peaks (ΔE, Table 5.3) has been used to approximate the average Mn oxidation state (AOS) by the equation, $AOS = 8.956 - 1.126\ \Delta E$.[174] Figure 5.13 shows that the peak separation of NALNMO powder is larger than LNMO powder. The calculated approximate average Mn oxidation states for LNMO powder is 4+, while that of NALNMO is $Mn^{3.74+}$. After 10 cycles, the splitting increases for both LNMO and NALNMO, corresponding to the approximate average oxidation states of $Mn^{3.36+}$ and $Mn^{3.17+}$, respectively. The XPS of the Mn 3s region agrees well with the Mn 3p region; both indicate a lower average oxidation state of Mn at the surface of NALNMO.

The Li 1s peaks are detected above the Mn 3p region around 55 eV. The green peaks at 56 eV correspond to LiF and the blue peaks at 54.3 eV correspond to Li-O in the lattice.[175] By comparing both soaked electrodes, NALNMO exhibits more LiF on the surface than pristine LNMO.

All the Ni 3p peaks sit at binding energy of 67.5 eV, indicating that the oxidation states of surface Ni ions are 2+.[176] This result is expected because the valence of Ni in the discharged states should be reduced from Ni^{4+} to Ni^{2+}. The NALNMO shows an extra peak at 74 eV, which is assigned to Al 2p. The position of this peak suggests that the coating is Al^{3+} in Al_2O_3, as demonstrated by Baggetto et al.[173] Because the peak does not shift in binding energy through 10

cycles, the amorphous Al_2O_3 coating likely remains chemically unaltered on the sample to this point.

5.4. Discussion

5.4.1. Surface structural changes induced by NH_4F and Al_2O_3 co-modification

Based upon the HRTEM and a-STEM/EELS results reported here, the surface of layered LNMO transforms to a spinel-like structure after NH_4F and Al_2O_3 surface co-modification. This spinel-like phase is induced by the weak acid treatment of NH_4F during surface modification, as reported previously by Sun et al.[177] Here, we propose the reaction equation (5.1) to describe its formation; the value of x is very small, and is theoretically less than 0.0038.

$$Li_{1.2}Ni_{0.2}Mn_{0.6}O_2 + 8xNH_4F + 4xH_2O \leftrightharpoons (1-x) \ Li_{1.2}Ni_{0.2}Mn_{0.6}O_2 \cdot 0.4x(LiNi_{0.5}Mn_{1.5}O_4) + 8xLiF + 8xNH_4OH \ (eq. \ 5.1)$$
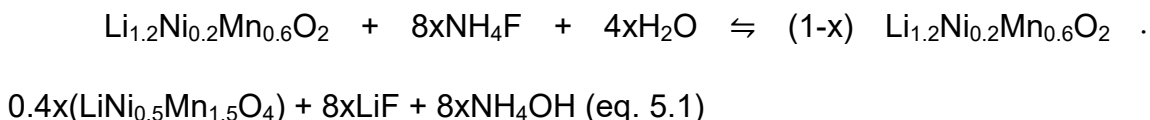
Before electrochemical cycling, NALNMO exhibits more LiF at the surface, which supports the reaction proposed above. Besides the formation of a spinel-like structure, nanoislands of active material were observed at the surface as well. Their presence may be the result of being etched away from the bulk by the NH_4F surface modification treatment.

In addition, non-uniform amorphous coatings have been observed by HRTEM. The XPS results indicate that the binding energy of Al 2p is 74 eV, which is the typical binding energy of Al_2O_3. This finding is supported by the study by Rosina, et al., which proposes that the surface coating of AlF_3 is actually

AlO_xF_y.[178] The Al-O bond was shown to preferentially form when the active material possesses surface hydroxides, which was likely the case for our hydroxide co-precipitated material.

We propose that the $Al(NO_3)_3 \cdot 9H_2O$ used in the surface modification process hydrolyzed directly; reaction equation (5.2) presents this process.

$$2Al(NO_3)_3 + 6\ NH_4OH \leftrightharpoons Al_2O_3 + 6\ NH_4NO_3 + 3\ H_2O\ (eq\ 5.2)$$
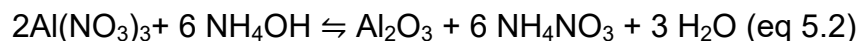
Based on the discussion above, a schematic structure model of NALNMO is depicted in Figure 5.14. A summary description of the proposed model possesses several unique attributes: 1) the spinel-like structure forms around the layered material's surface, with 3 nm thickness; 2) the amorphous coating exists on the outermost exterior and consists of amorphous Al_2O_3, as identified using TEM and XPS; 3) nanoislands, (<20 nm) exist on the surface as well, which arise from modification treatment.

5.4.2. Origin of improved electrochemical performance after NH_4F and Al_2O_3 surface co-modification

One related question raised in previous sections is, why does NALNMO exhibit a longer charge plateau, but less irreversible capacity? In fact it exhibited a 34 mAh g^{-1} larger discharge capacity overall. After all Ni ions are fully oxidized after the slope region from 3.7 to 4.4 V, the plateau at 4.5 V is believed to originate from Li$^+$ being extracted from the structure and accompanied by the oxidation of lattice oxygen. Armstrong et al. observed that oxygen leaves the structure in the form of O_2 gas by using in situ differential electrochemical mass

spectrometry (DEMS).[100] Hy et al. proposed the formation of Li_2O and Li_2CO_3 during the plateau region as a result of oxygen evolution, using surface enhanced Raman spectroscopy (SERS).[145] Koga et al. and Sathiya et al. claimed that lattice $O^{(2-\delta)-}/O^{2-}$ is activated during charge and discharge.[53, 179] The notably longer plateau exhibited by NALNMO may likely be caused by the nanoislands active material introduced during surface modification. Due to nanosizing, these nanoislands may show improved diffusion kinetics as well as higher propensity to activation during electrochemical cycling. This enhanced activation may be reflected in the first cycle charge profile, which exhibits a longer plateau region compare to the pristine material.

The amorphous Al_2O_3 surface coating likely acts as protective layer to prevent side reactions between electrode and electrolyte, as well as to limit the irreversible loss of oxygen, as proposed by Zheng et al. and Koga et al.[45, 46] This layer may, therefore, contribute to the improved irreversible capacity loss observed in the first cycle electrochemical profile. It should be noted that this protective layer was not observed on the surface nanoislands, which may contribute to the capacity fading observed for NALNMO.

Though there is only a simple slope observed during discharge, the dQ/dV plot shows it to be a complex multiple-reaction process. Because the capacity during discharge is always larger than the capacity theoretically possible by the Ni^{4+} to Ni^{2+} reduction reaction, many efforts have been made to describe the reversibility of oxygen reduction in order to explain the extra capacity.[145, 169, 170, 179] Some groups suggest that the extra capacity also originates from the Mn^{4+} to

Mn^{3+} reduction reaction.[144, 180] The LNMO and NALNMO respectively show 148 mAh g^{-1} and 159 mAh g^{-1} discharge capacity above 3.5 V, which is larger than the 126 mAh g^{-1} possible from theoretical redox of Ni^{2+}/ Ni^{4+}. This may indicate that a higher degree of reversibility of the oxygen redox pair reaction happens for the NALNMO above 3.5 V during discharge in comparison to the LNMO. The discharge capacities below 3.5V are 105 mAh g^{-1} and 128 mAh g^{-1} for LNMO and NALNMO, respectively. Considering the longer plateau during charge and more Mn^{3+} after 1 cycle observed in surface modified material and the stabilization of the 2nd peak in the dQ/dV curve, this capacity difference may arise from the pre-activated and electrochemically activated surface Mn allowing for some Mn^{3+}/Mn^{4+} redox pair reaction, and higher degree of reversibility for the oxygen redox pair reaction. In summary, the origin of the improved discharge capacity by NH_4F and Al_2O_3 surface co-modification may consist of decreased irreversible oxygen loss, higher degree of reversibility for the oxygen redox pair reaction facilitating the activation of cathode material, and pre-activating of the surface leading to more Mn^{3+}.

As described previously, NALNMO exhibits higher discharge capacity in early cycles, but becomes closer to the pristine sample, after 80 cycles. For the 3rd peak region, both materials show increasing capacity upon the 10th cycle, the increasing Mn^{3+} content from the 1st cycle to 10th cycle at surface of both materials detected by XPS is an indication for the increased participation of Mn^{3+}/ Mn^{4+} redox pair. A stark difference was found for the 2nd peak regions in the dQ/dV plot where the 2nd peaks of LNMO shift by a large degree driving the Ni-

redox process to lower potential and becoming indiscernible possibly destabilizing the LNMO. In contrast, while NALNMO shows a decrease in the intensity of the 2nd peak, the apex of the peak maintains it potential position and is still prevalent after the 80th cycle. Both the 1st and 3rd peaks have been associated with oxygen reduction, and the latter specifically to manganese reduction. For NALNMO, due to possibly pre-activation, the manganese and oxygen-redox occurs on the onset of early cycles while LNMO is mostly dominated by these reactions in later cycles. While NALMNO shows capacity decrease, the reduction process of Ni^{4+} to Ni^{2+} remains relatively constant maintaining long-term stability of this material.

Besides the capacity degradation, both materials suffer from voltage decay upon cycling. The three peaks in the dQ/dV plots were fit using separate Gaussian functions in order to determine the position of each peak. The 3rd peak of both materials shifted to ~ 3.0V after 80 cycles, which is 0.3 V lower than their first cycle. The changes in position of the 1st and 2nd peaks revealed different trends in both materials upon cycling. The 2nd peak of LNMO lowered by ~0.4V, while the same peak of NALNMO decreased by only ~0.1V. There is a ~0.2V shift of the 1st peak to lower voltage for LNMO, but only ~0.1V for the NALNMO. Based upon analysis of the dQ/dV plots and surface characterization of pristine and surface modified materials, we can draw the conclusion that the NH_4F and Al_2O_3 surface co-modification partly stabilized the 1st and 2nd peak regions, in terms of capacity and voltage, but the 3rd peak region continues to show degradation upon cycling.

This detailed study of the role of NH_4F and Al_2O_3 surface co-modification suggests that each treatment during the modification process can dramatically transform the materials' surface structure and chemistry. Those changes have contributed to the electrochemical performance of the final samples from different aspects. Adding mild acid introduced the surface spinel-like structure and etched nanoislands formations, which will facilitate the activation of the cathode material, leading to a higher discharge capacity. An amorphous surface coating reduced the direct reaction between electrode and electrolyte, resulting in less irreversible oxygen loss. More surface modification works are undergoing, in order to discover an ideal surface modification method.

5.5. Conclusion

In this work, we reveal that the surface chemistry of cathode materials will significantly affect the uniformity and chemistry of coating layer. The surface co-modifications brought changes to the material's surface, from both a structural and chemical aspect. In order to identify these sophisticated changes, multi-modality surface sensitive tools was applied in an attempt to obtain a complete picture. The NH_4F promoted the transformation of a surface spinel-like phase, as well as the formation of isolated nanoislands of active material, which facilitated the activation of the cathode material, leading to higher discharge capacity. At the same time, amorphous Al_2O_3 surface coating reduced the side reaction between electrode and electrolyte, and also irreversible oxygen loss, thus reducing the irreversible capacity. In particular, while the Mn^{3+} / Mn^{4+} redox pair

still showed to increase indicating destabilization, the surface co-modification stabilized the Ni^{2+} / Ni^{4+} region in terms of capacity and voltage. The fundamental understandings of this work may not only be widely used to explain the role of other surface modifications used for high voltage cathode materials, but they could also guide us in designing better cathode materials with higher energy density.

Chapter 5, in part, is a reprint of the material "Understanding the Role of NH_4F and Al_2O_3 Surface Co-Modification on Lithium-excess Layered Oxide $Li_{1.2}Ni_{0.2}Mn_{0.6}O_2$" as it appears in the ACS Applied Materials & Interfaces, Haodong Liu, Danna Qian, Mike G. Verde, Minghao Zhang, Loïc Baggetto, Ke An, Yan Chen, Kyler J. Carroll, Derek Lau, Miaofang Chi, Gabriel M. Veith, Ying Shirley Meng, ACS Applied Materials & Interfaces, 2015, 7 (44), 24791. The dissertation author was the primary investigator and author of this paper. All experiments and data analysis were performed by the author except for the TEM and STEM-EELS part.

Figure 5.1 SEM images: (a) and (b) are LNMO, (c) and (d) are NALNMO.

Element	Weight%	Atomic%
O K	38.62	65.06
F K	5.51	7.81
Al K	0.32	0.32
Mn K	41.29	20.26
Ni K	14.25	6.54
Totals	100.00	
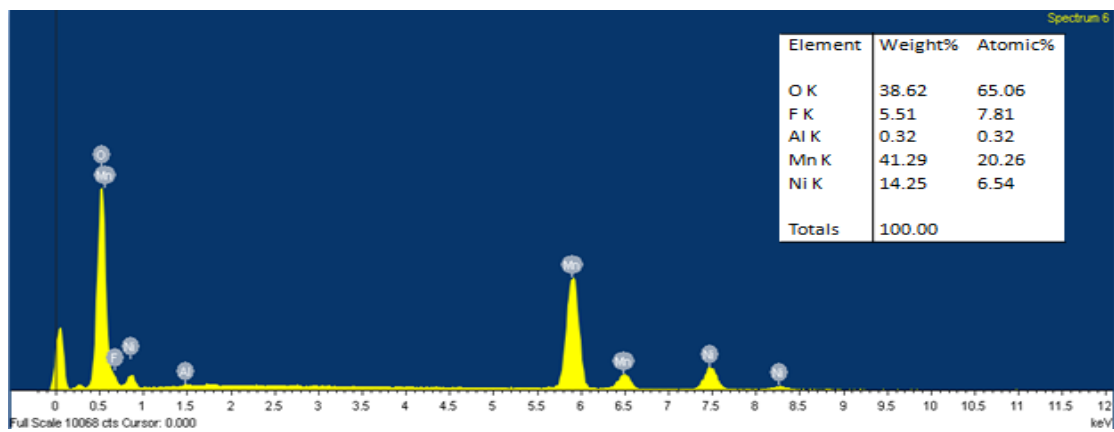
Figure 5.2 EDS spectrum of NALNMO starting material.
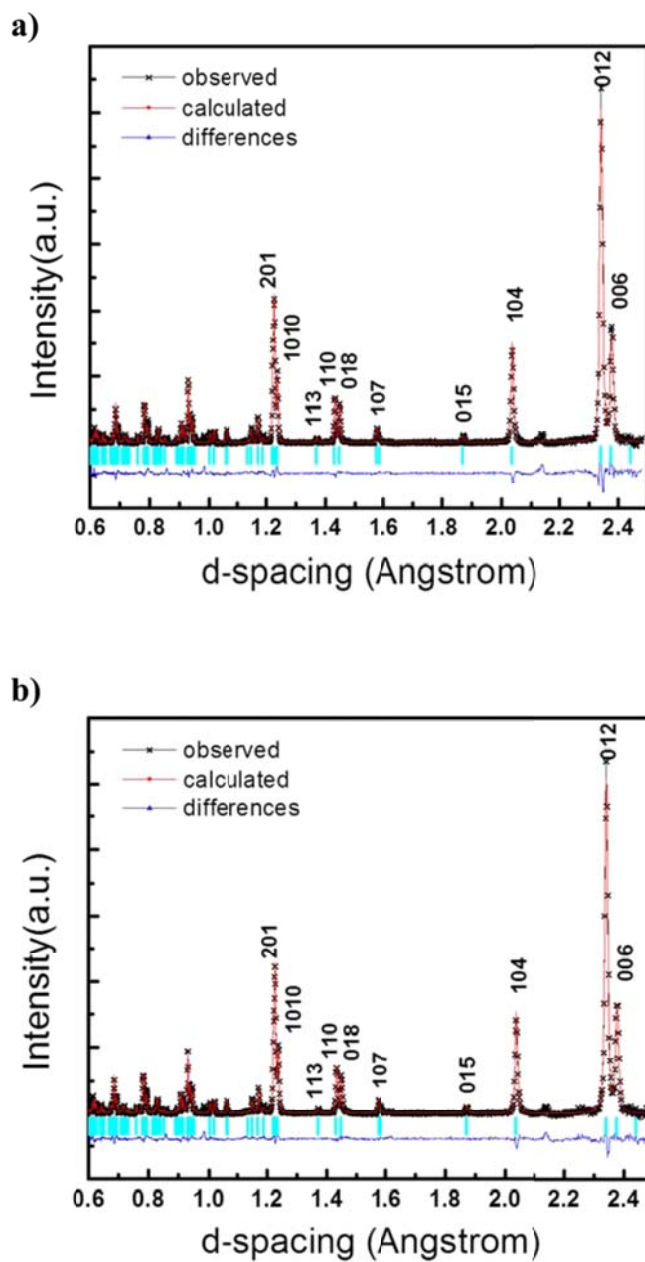
Figure 5.3 ND patterns of (a) LNMO and (b) NALNMO. The black crosses represent the observed pattern, the red line corresponds to the calculated diffraction pattern and the blue line shows the differences between observed and calculated pattern.
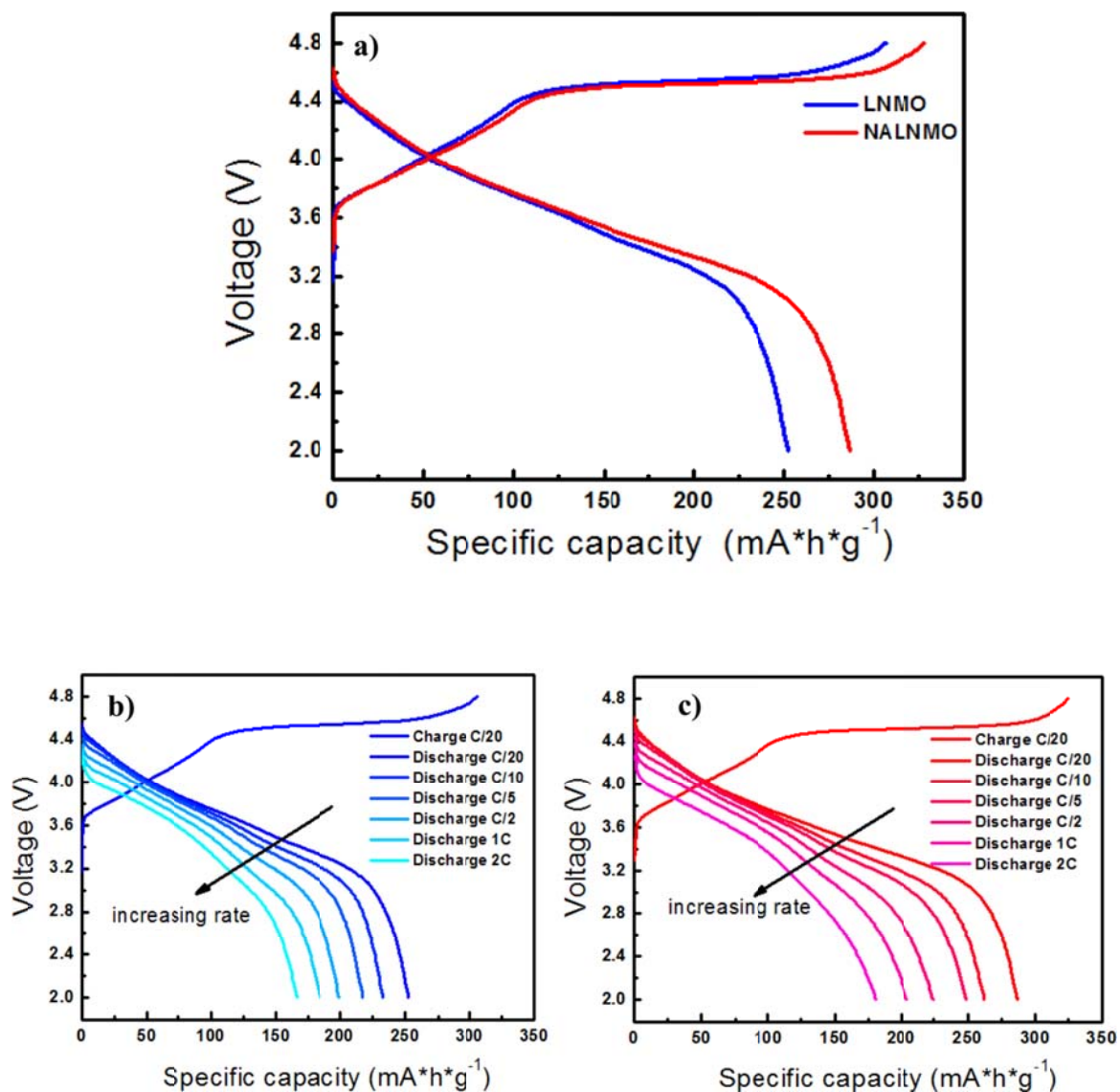
Figure 5.4 Comparison of electrochemical performances between LNMO and NALNMO. (a) first cycle charge/ discharge voltage profile, (b) voltage profile of LNMO under different current density, (c) voltage profile of NALNMO under different current density. Voltage range is 2.0 - 4.8 V at 1C = 250 mA g^{-1}.
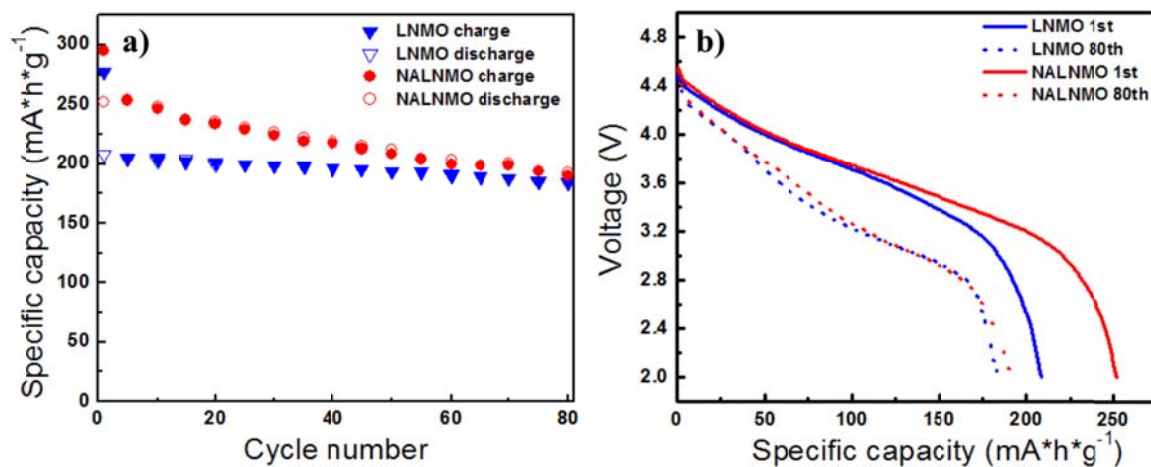
Figure 5.5   Comparison of (a) capacity, and (b) discharge voltage, between LNMO and NALNMO, after 80 cycles. Voltage range is 2.0 - 4.8 V at C/10 = 25 mA g^{-1}.
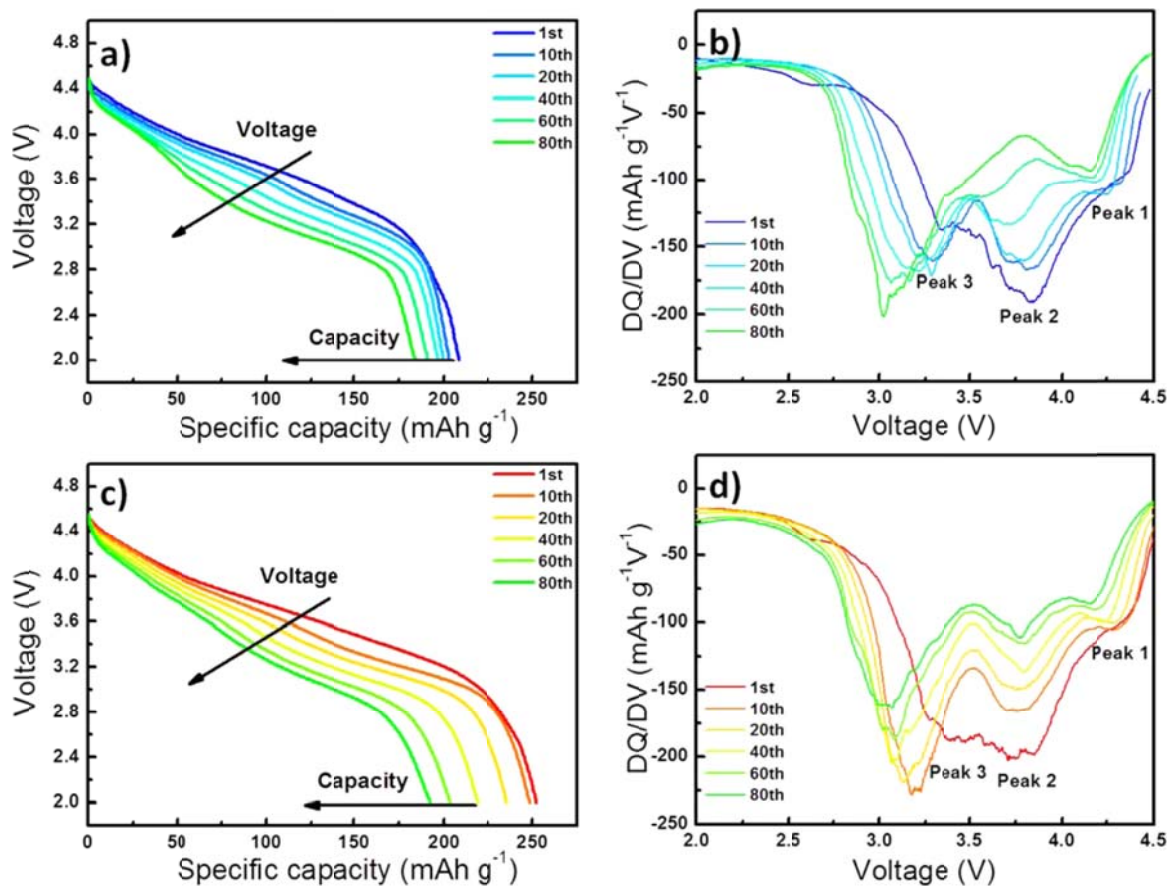
Figure 5.6 Discharge and corresponding dQ/dV profiles of (a) & (b) LNMO and (c) & (d) NALNMO, over the course of 80 cycles.
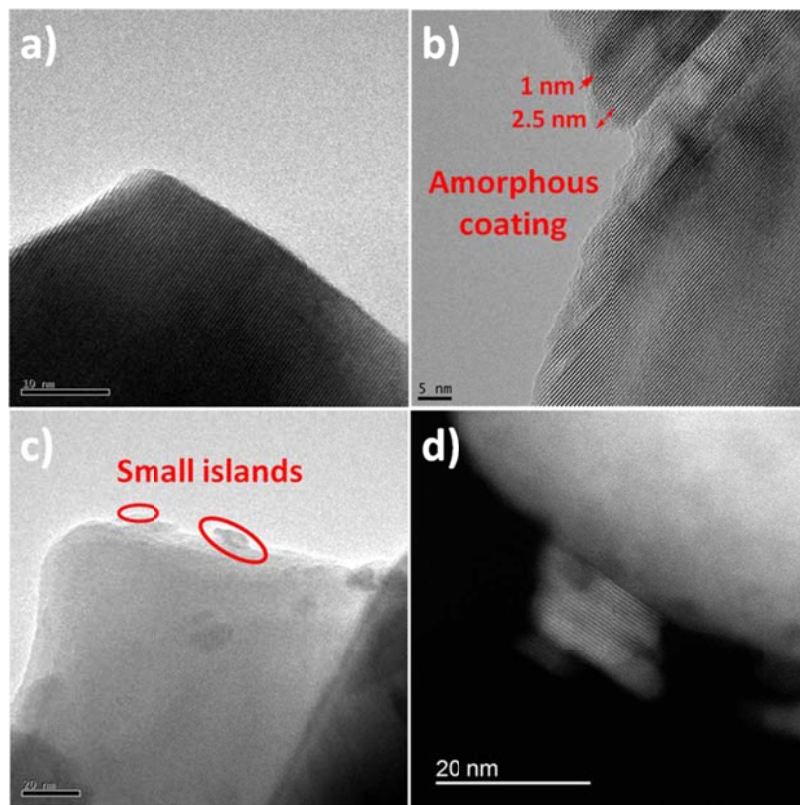
Figure 5.7 TEM and STEM photographs of LNMO and NALNMO, (a) TEM of LNMO, (b) and (c) TEM of NALNMO, (d) STEM of NALNMO.
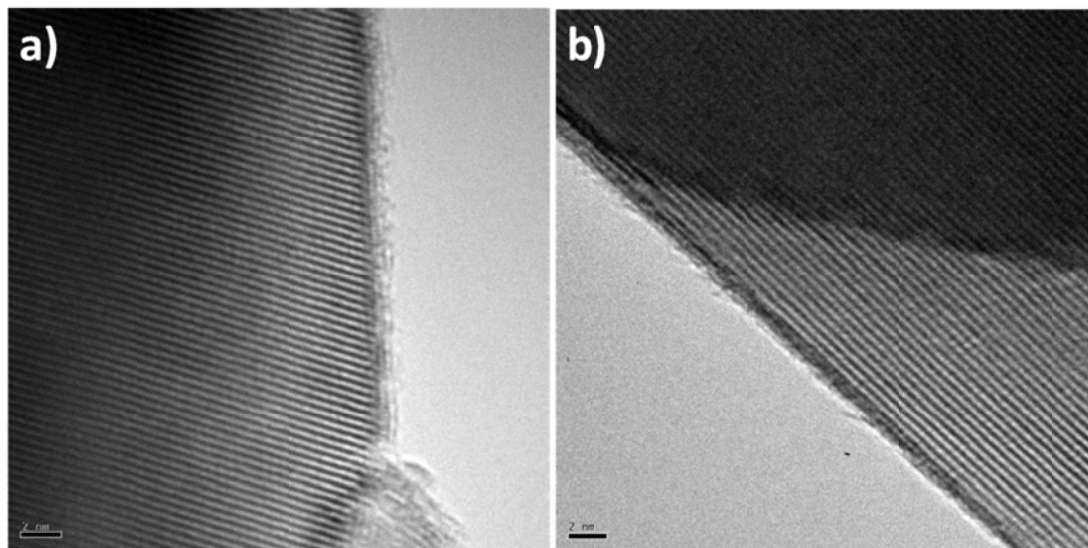
Figure 5.8   TEM photographs of pristine NALNMO, prepared from carbonate method.
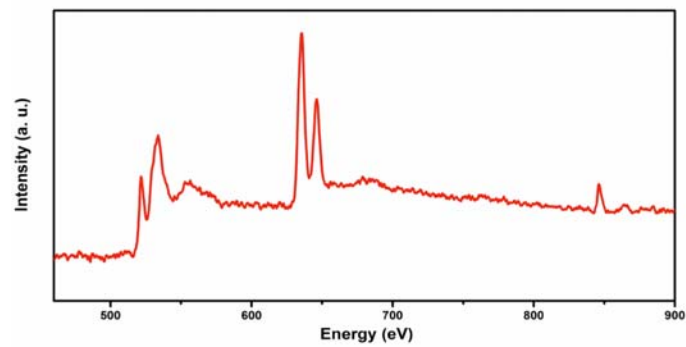
Figure 5.9 EELS spectrum of crystalline nano-islands at the surface of NALNMO.
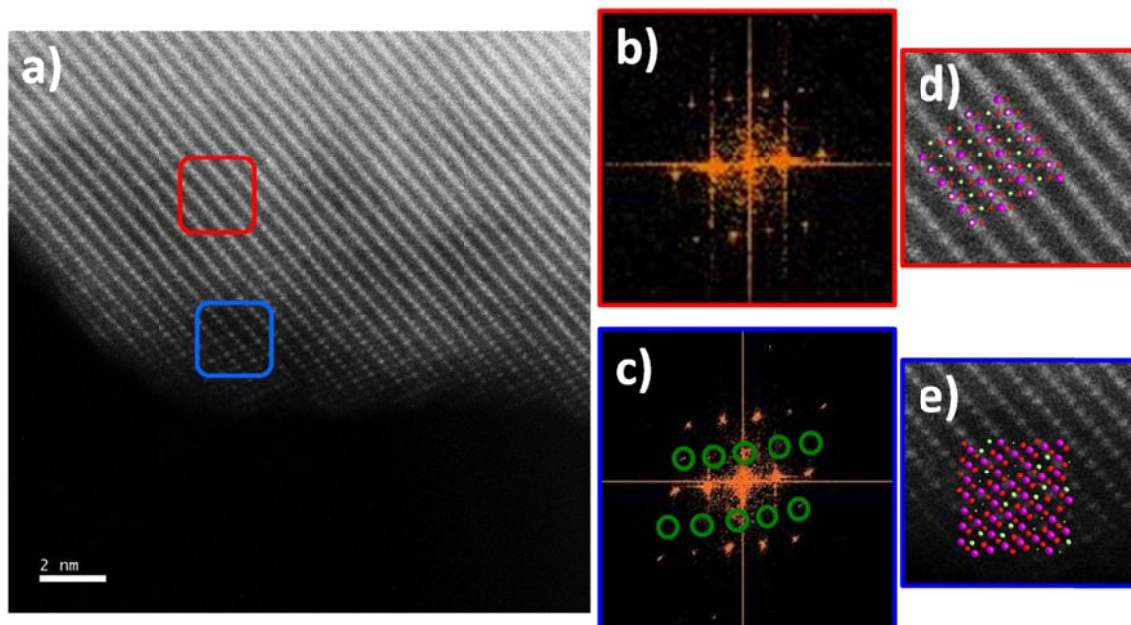
Figure 5.10 High-resolution STEM images of NALNMO, (a) NALNMO, (d) bulk region and (e) surface region. The fast Fourier transform FFT, (b) bulk region and (d) surface region. (The insets crystal structure in (d) and (e), green: Li, red: O, purple: transition metal)
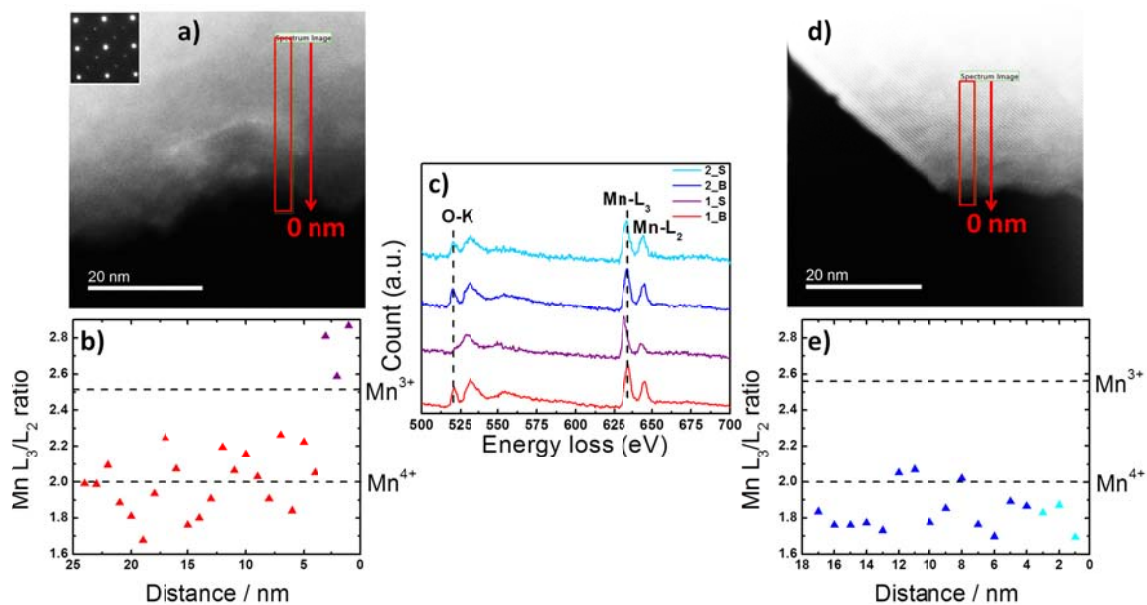
Figure 5.11 STEM images of NALNMO with step scan of Mn EELS L edge and O EELS K edge. (a) STEM of NALNMO with C2/m domain, (b) corresponding Mn L_3/L_2 ratio, (c) representative EELS spectra of the Mn L edge and O K edge from the surface and bulk of NALNMO with different domains, (1 is C2/m domain particle, 2 is R$\bar{3}$m domain particle, S represent surface, B represent bulk), (d) STEM of NALNMO with R$\bar{3}$m domain, and (e) corresponding Mn L_3/L_2 ratio.
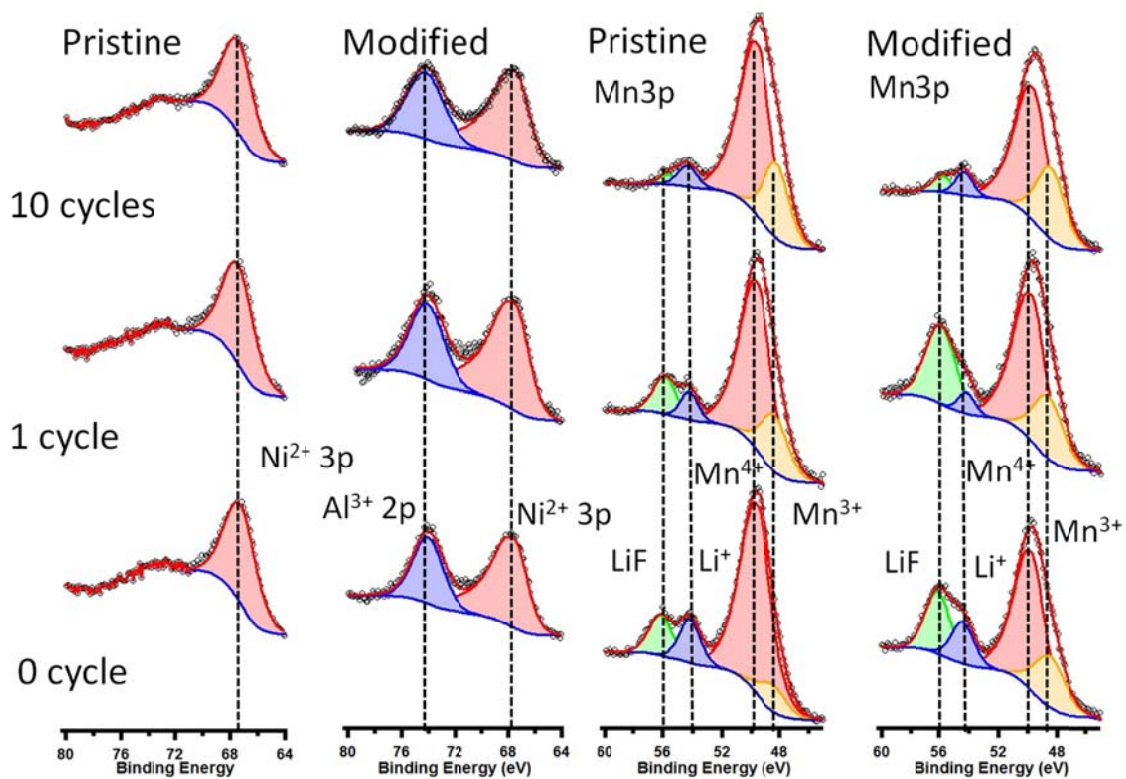
Figure 5.12 Ni 3p and Mn 3p core level X-ray photoelectron spectra of LNMO and NALNMO at various stages of cycling.
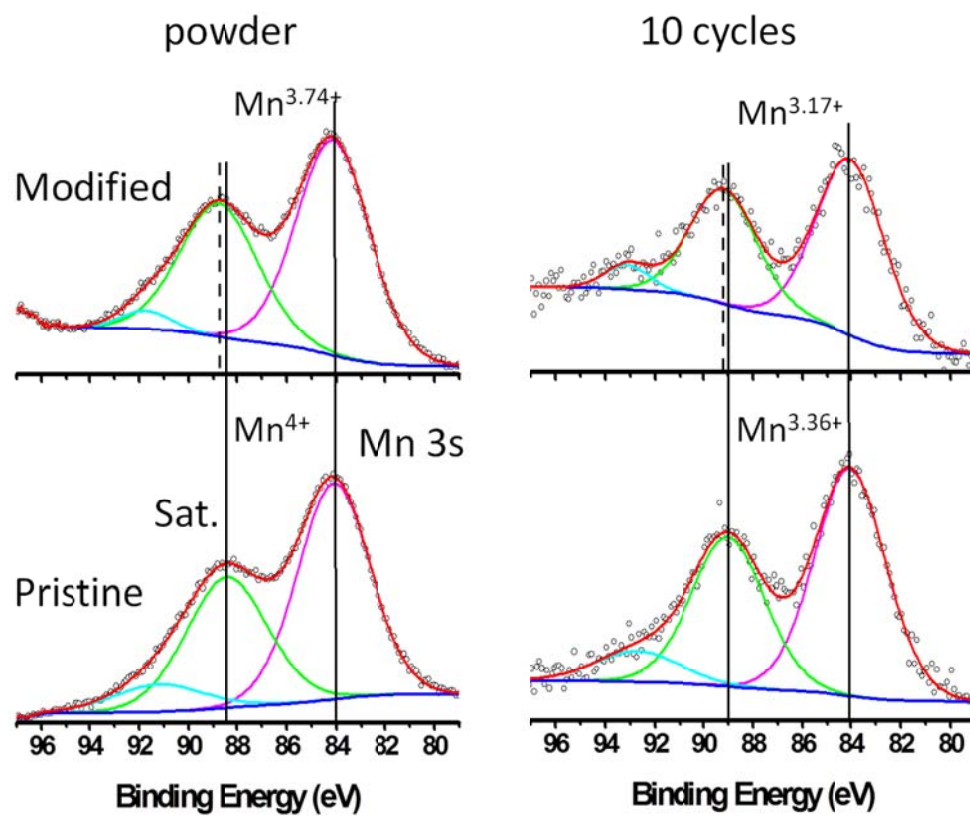
Figure 5.13 XPS Mn 3s regions of LNMO and NALNMO pristine and cycled electrode materials.
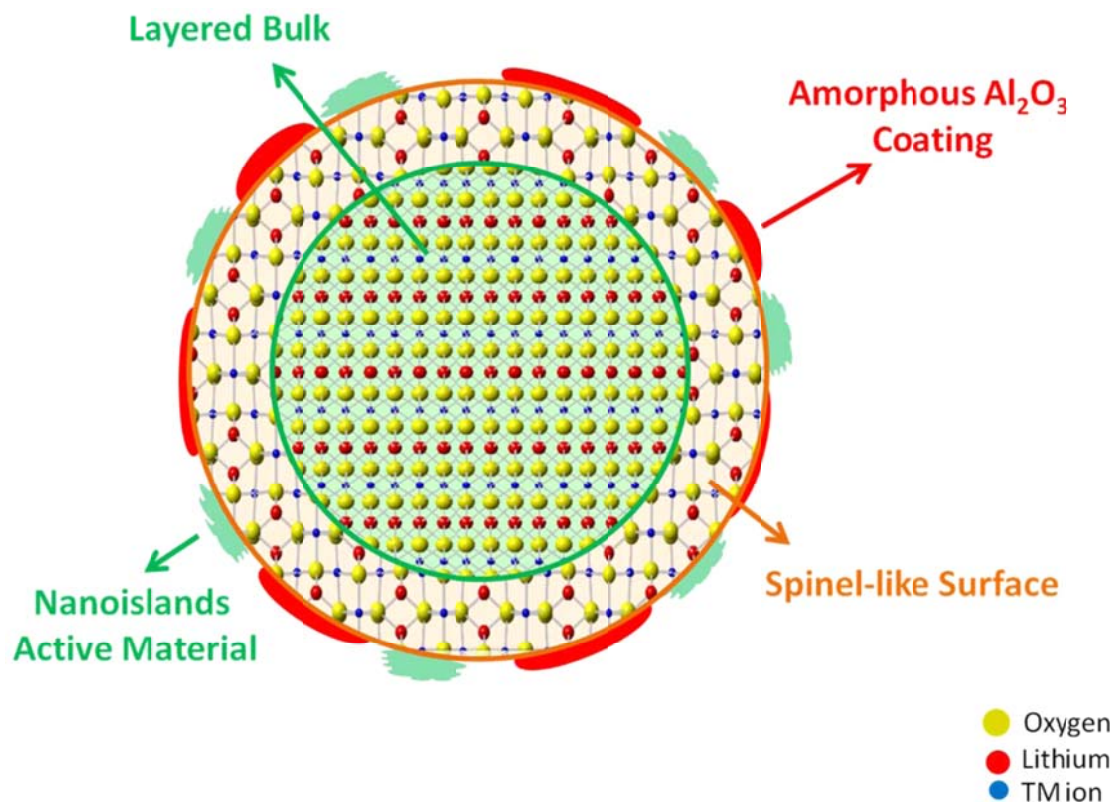
Figure 5.14 Schematic of proposed structure model of NALNMO (not draw to scale).

Table 5.1 Rietveld refinement results of neutron diffraction data for LNMO and NALNMO powders.

	a (Angstrom)	c (Angstrom)	Li/Ni mixing	Oxygen coordinates	R_p	R_{wp}
LNMO	2.8615(1)	14.2580(6)	0.037(4)	0, 0, 0.2417(7)	4.29%	5.77%
NALNMO	2.8623(1)	14.2621(6)	0.040(4)	0, 0, 0.2416(7)	3.81%	5.22%

Table 5.2 The summary of surface Mn^{3+} percentage of LNMO and NALNMO at different cycle number.

	Cycle #	Percentage of Mn^{3+} (%)
LNMO	Non-cycled	10.1
	1	21.6
	10	24.5
NALNMO	Non-cycled	25.8
	1	27.3
	10	31.0

Table 5.3 XPS Mn 3s region peak separations of LNMO and NALNMO pristine and cycled electrode materials.

	Cycle #	ΔE (eV)
LNMO	Powder	4.33
	10	4.97
NALNMO	Powder	4.63
	10	5.14

Chapter 6. Enhancing the Electrochemical Performance of Lithium-Excess Layered Oxide $Li_{1.13}Ni_{0.3}Mn_{0.57}O_2$ via a Facile Nanoscale Surface modification

In this work, a facile surface modification with nanoscale equilibrium Li_3PO_4-based surface amorphous films (SAFs) has been applied to Lithium-excess layered oxide $Li_{1.13}Ni_{0.3}Mn_{0.57}O_2$, which significantly improves the first cycle coulombic efficiency, rate capability, and cycling stability. The nanoscale surface modification can be easily achieved by ball milling and isothermal annealing. The optimized surface modified $Li_{1.13}Ni_{0.3}Mn_{0.57}O_2$ is capable of maintaining a high capacity of 201 mAh g^{-1} after 60 cycles at 55 °C testing with a rate of 1 C. This work provides a facile and scalable surface modification method to improve electrochemical performance of cathode materials for lithium ion batteries.

6.1. Introduction

The Lithium-excess layered oxides benefit from an extraordinary high reversible capacity (> 280 mAh g^{-1}) and is one of the most promising cathode materials for plug-in electric vehicle application.[43, 66, 181] However, this high-energy-density material suffers from large irreversible capacity in its first electrochemical cycle when it is charged to high voltages, namely more than 4.6

V. In addition, its rate capability is yet unsatisfactory for high power application. Moreover, the gradual voltage and capacity degradation upon electrochemical cycling, especially at elevated temperature when side reactions related to the interactions with the electrolyte occur more prevalently, represent the most serious technical challenge for this material.[145, 182] In the past few years, significant amount of surface modification works have been carried out to protect the surfaces of the Li-excess. Most of the reported surface modifications are performed under solution-based reactions.[67, 183, 184] For example, Bian et al. used LiOH and $NH_4H_2PO_4$ to coat Lithium-excess with Li_3PO_4.[183] However, the solution based surface modification adds an additional layer of complexity for preparation of Lithium-excess, which will definitely raise the cost of production. Although Konishi coated high voltage spinel $LiNi_{0.5}Mn_{1.5}O_4$ with uniform Li_3PO_4 via pulsed laser deposition (PLD), this technique requires special equipment, which is difficult to realize for large scale production.[185]

In this work, we modify the surface of Lithium-excess layered oxide $Li_{1.13}Ni_{0.3}Mn_{0.57}O_2$ via simple mixing and calcination to form Li_3PO_4-enriched and nanometer-thick surface amorphous films (SAFs).[126] Our results indicate that the optimized material shows remarkably improved performance.

6.2. Experimental

The synthesis of the Li-excess is described in our previous publications.[43, 67] The procedure for preparing Li_3PO_4 surface modified $Li_{1.13}Ni_{0.3}Mn_{0.57}O_2$ (LPLNMO) was adapted from work by Huang et al.[126] 0.06 g Li_3PO_4 (Alfa Aesar,

99.99%) and 3 g $Li_{1.13}Ni_{0.3}Mn_{0.57}O_2$ were mixed using a planetary ball mill (PM 100, Retsch). The powder was calcinated at 500 °C (LP500), 600 °C (LP600), and 700 °C (LP700), respectively, for 5 h in air. Electrochemical test, XRD, SEM and HRTEM characterization are described with details in our previous work.[66, 67]

6.3. Results and Discussion

Results

Figure 6.1 shows the SEM images of the LNMO and LPLNMOs. All materials show secondary particles with a wide size distribution below 10 µm; the primary particle size distribution ranges from 50 to 200 nm. There were no dramatic changes to the morphology or particle size after Li_3PO_4 surface modification.

HRTEM is used to identify the Li_3PO_4 coating (SAFs) on LP600. The TEM images show very good layered bulk crystal structure, and amorphous films on the surface of LP600. More than 20 particles are analyzed to examine the amorphous film. As shown in Figure 6.1 (i), particles have the amorphous film evenly coated on the surface, with the thickness of ~2 nm. While the majority of particles exhibit uniform coatings, there are some particles that still show clean surfaces with no indication of surface coatings, as illustrated in Figure 6.1 (j).

The XRD of LNMO and LPLNMOs are refined and plotted in Figure 6.2. The major diffraction peaks of these materials are indexed to the $R\bar{3}m$ space group.[66, 136, 146] No obvious changes were observed in these peaks after Li_3PO_4 surface modification, suggesting that the layered phase is well retained. The

lattice parameters of LNMO are a = 2.8641(3) Å and c = 14.253(2) Å. Both LP500 and LP600 show no change in lattice parameters, however, LP700 demonstrates expanded lattices, which suggests the bulk structure changes under high temperature calcination.

Figure 6.3 (a) – (d) illustrate the first charge/discharge voltage profiles of LNMO and LPLNMOs within the voltage window of 2−4.8 V, at 12.5 mA g^{-1} (C/20). The LNMO delivers a charge capacity of 317 mAh g^{-1}, and a discharge capacity of 223 mAh g^{-1}. A low coulombic efficiency of 70.4% has been observed in LNMO. The LP500 demonstrates similar charge capacity of 319 mAh g^{-1}, but much higher discharge capacity of 261 mAh g^{-1}. Consequently, the coulombic efficiency of LP500 increases to 81.2%. In contrast, the charge capacity of LP600 decreases to 299 mAh g^{-1} while the discharge capacity increases to 258 mAh g^{-1} at the same time. Both factors contribute to a compressed irreversible capacity of 41 mAh g^{-1} leading to the relatively higher coulombic efficiency of 86.3%. Once the calcinations temperature is raised to 700°C, the LP700 exhibits a high irreversible capacity of 110 mAh g^{-1}. Figure 3e compares the capacities of these materials at different discharge rates. Among all the materials, LP600 shows the highest coulombic efficiency and best rate capability.

The long-term cycling performance of LNMO and LPLNMOs were compared, which is represented in Figure 6.3 (f). Over the course of 100 cycles, LNMO, LP500, and LP700 suffer from significant capacity fading. According to the XRD results, the bulk structure of LP700 was changed by high temperature calcination which may accelerate the capacity degradation upon cycling.

Although the bulk structure of LP500 is retained, the temperature is not high enough to form an effective coating layer on the layered oxides.[126] Both LNMO and LP600 are cycled for extra 50 times. After 150 cycles, the capacity difference between the LNMO and LP600 increases to 49 mAh g^{-1}, which is larger than 36 mAh g^{-1} of the first cycle.

Both LNMO and LP600 are cycled at 55 °C within the voltage window of 2−4.8 V, at 250 mA g^{-1}. Figure 6.4 (a) compares their first charge/discharge voltage profiles. Both materials show larger charge/discharge capacities than their low current testing values at room temperature, which is due to the higher lithium activity at elevated temperature.[126] An obvious elongated slope (~ 218 mAh g^{-1}) appears in LNMO, which indicates the reactions between electrode and electrolyte happens below 4.4 V at 55 °C. After the Li_3PO_4 surface modification, the charge capacity decreases from 390 to 332 mAh g^{-1} while the discharge capacity increases from 246 to 271 mAh g^{-1}, respectively. The corresponding coulombic efficiency escalates from 63.1% to 81.6%.

The charge/discharge capacities of both materials are compared in Figure 6.4 (b). Large irreversible capacities exist in each cycle of LNMO, while the LP600 only exhibits irreversible capacity in its first cycle. LP600 delivers 201 mAh g^{-1} with an enhanced capacity retention of 74.2% after 60 cycles. As a comparison, LNMO only shows 41% capacity of its first cycle.

General discussions

LP600 delivers a high coulombic efficiency of 86.4% in its first cycle. Both suppressed irreversible lattice oxygen loss and reduced undesired side reactions with electrolyte lead to lower charge capacity, which is indicated by the shorter charge plateau. As a consequence, LP600 gets a better electrode/electrolyte interface, which facilitates the lithium transports during discharge and following cycles. The high temperature tests are designed to verify this hypothesis. In Figure 6.4 (c) – (d), the LNMO demonstrates large discharge voltage slippage, which indicates the rapid growth of cathode electrolyte interface (CEI) on the surface of LNMO.[67, 145, 182] This undesired CEI traps or slows down the lithium diffusion, thus causing serious capacity and voltage degradation in LNMO. In the case of LP600, the CEI is mitigated by the Li_3PO_4 coating layer by reducing direct contact between the electrode and electrolyte. In addition, the Li_3PO_4 coating layer protects the electrode from etching by acidic species in the electrolyte.[184, 186] Moreover, the surface reconstruction of Li-excess may also be alleviated through suppressing the oxygen loss. The Li_3PO_4 coating improves the voltage stability for Lithium-excess, however, it is suggested that surface modification, bulk substitution, and interface optimization should work together in order to overcome the voltage fading in Li-excess.

6.4. Conclusions

In this work, we applied nanoscale self-regulated Li_3PO_4-based surface amorphous films to Lithium-excess layered oxide $Li_{1.13}Ni_{0.3}Mn_{0.57}O_2$ via a facile method. The mixture of 2 wt.% Li_3PO_4 and $Li_{1.13}Ni_{0.3}Mn_{0.57}O_2$ annealed at 600 °C

shows significantly improved coulombic efficiency in first cycle, rate capability, and cycling stability of Li-excess. These improvements are valid even at an elevated temperature. We expect that this scalable method will also work for other high voltage cathode materials for lithium ion batteries.

Chapter 6, in full, is a reprint of the material "Enhancing the Electrochemical Performance of Lithium-Excess Layered Oxide $Li_{1.13}Ni_{0.3}Mn_{0.57}O_2$ via a Facile Nanoscale Surface Modification" as it appears in the Journal of the Electrochemical Society, Haodong Liu, Jiajia Huang, Danna Qian, Sunny Hy, Chengcheng Fang, Jian Luo, and Ying Shirley Meng, Journal of the Electrochemical Society, 2016, 163 (6), A971. The dissertation author was the primary investigator and author of this paper. All experiments and data analysis were performed by the author except for the TEM part.
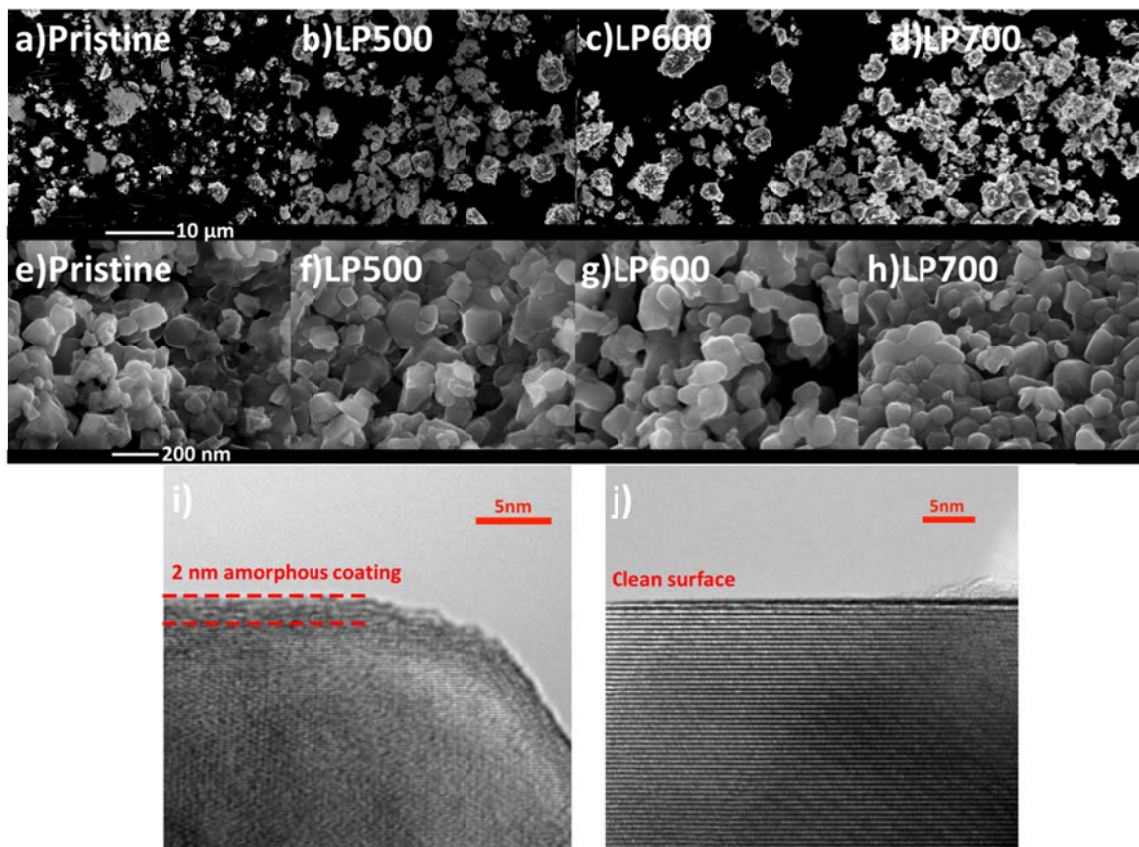
Figure 6.1 SEM images: (a)-(h). TEM images of LP600: (i) particles with coating and (j) particles that were surface modified but still were not coated.
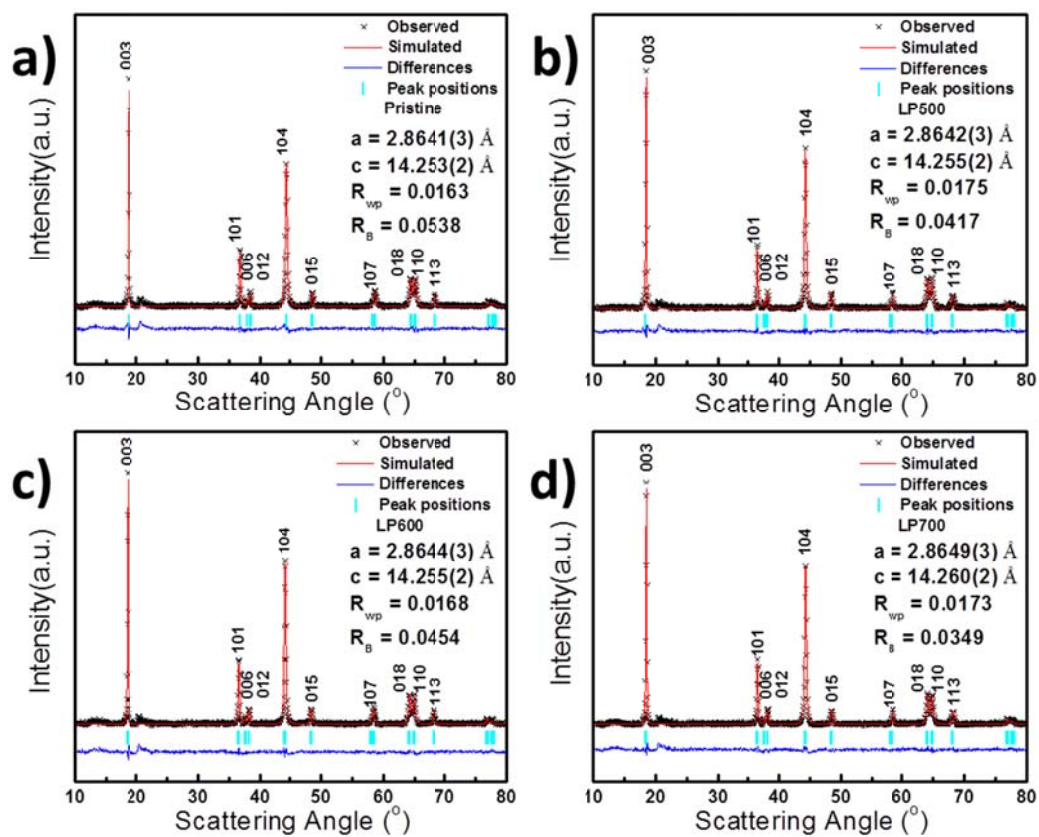
Figure 6.2 XRD patterns and refinements of LNMO and LPLNMOs.
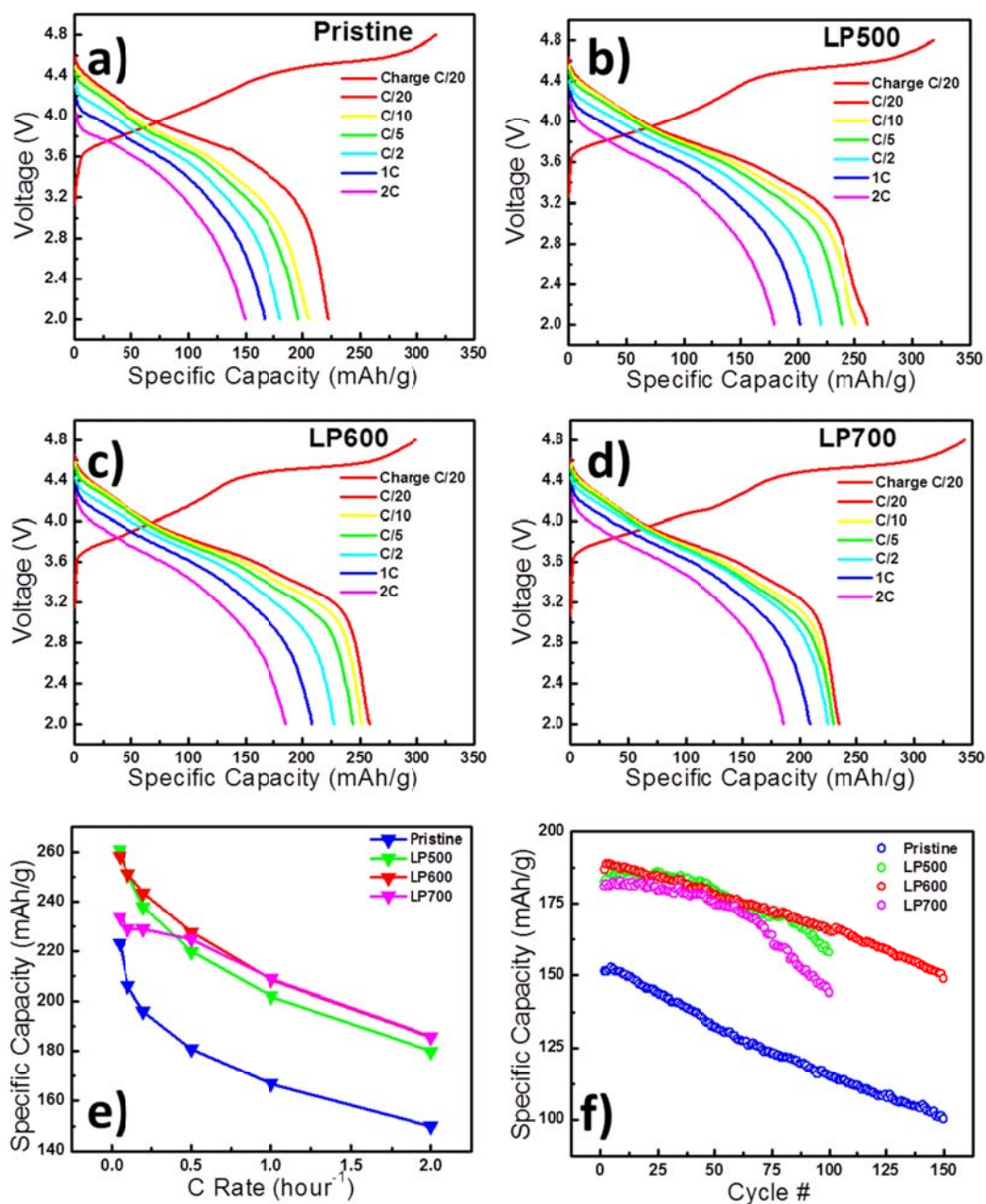
Figure 6.3 Comparison of electrochemical performances between LNMO and LPLNMOs: (a)-(d) voltage profiles under different current density; (e) discharge capacity under different current density; and (f) comparison of capacity upon cycling, the voltage range is 2.0−4.8 V at 1 C = 250 mA g^{-1}.
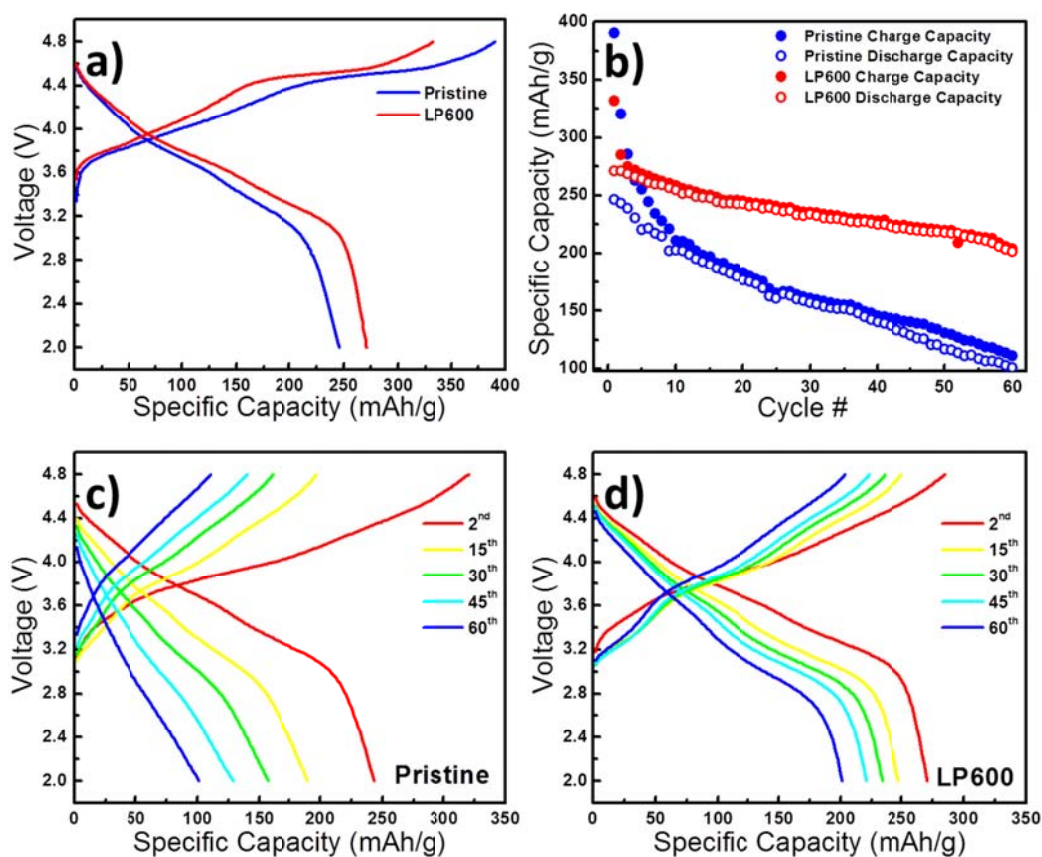
Figure 6.4 Comparison of electrochemical performances between LNMO and LP600 at 55 ℃: (a) first cycle voltage profile; (b) comparison of capacity over the course of 60 cycles; (c) and (d) voltage profiles at different cycles. The voltage range is 2.0−4.8 V at 1 C = 250 mA g^{-1}.

Chapter 7. A new O3-type layered oxide cathode with high energy / power density for rechargeable Na batteries

A new O3 - $Na_{0.78}Li_{0.18}Ni_{0.25}Mn_{0.583}O_w$ is prepared as the cathode material for Na-ion batteries, delivering exceptionally high energy density and superior rate performance. The single-slope voltage profile and ex situ synchrotron X-ray diffraction data demonstrate that no phase transformation happens through a wide range of sodium concentrations (up to 0.8 Na removed). Ni^{2+} / Ni^{4+} is suggested to be the main redox center. Further optimization could be realized by tuning the combination and ratio of transition metals.

7.1. Introduction

Na-ion batteries have recently gained increasing recognition as intriguing candidates for next-generation large scale energy storage systems, owing to significant cost advantages stemming from the high natural abundance and broad distribution of Na resources. Although in terms of absolute energy density, the currently available Na-ion battery materials are not competitive with their Li-ion systems which are one of the dominating energy technologies in this decade, there are studies suggesting that Na-ion systems should not be discarded.[187, 188] In particular, Na-ion batteries operating at room temperature could be suitable for applications where specific volumetric and gravimetric energy density requirements are not as stringent as in EVs, namely in electrical grid storage of intermittent energy produced via renewable sources.[189] This would also contribute to a significant reduction of the costs connected to the use of

renewable sources, which could then penetrate the energy market more easily and make Na-ion technology complementary to Li-ion batteries for stationary storage.[190-192]

For the past several years, a variety of novel materials have been explored as electrodes for Na-ion batteries. Since Na ion has a relatively larger ionic radius than that of the Li ion, materials with an open framework are required for facile Na ion insertion / extraction. Following this strategy, many breakthroughs in cathode materials have been achieved, such as layered and polyanion compounds.[193, 194] Among most of the Na cathode compounds reported to date, the P2 and O3 structured Na oxides (Na_xTMO_2, TM = Transition Metal) have drawn significant attentions, since their relatively opened structures are able to accommodate large Na ions providing spacious diffusion path as well as the structural stability. The research on the structural properties of Na_xTMO_2 was started in 70's by Delmas et al..[84, 195] Recently, various $P2-Na_xTMO_2$, and their binary or ternary derivatives, have been extensively investigated and some of them demonstrated superior electrochemical performances.[87, 196-201] On the other hand, O3 structured materials have also shown great progress. For example, $NaCrO_2$ was investigated by Komaba et al., and showed 120 mAh g^{-1} of specific capacity near 2.9 V.[202, 203] The $O3-NaNi_{0.5}Mn_{0.5}O_2$ electrodes delivered 105 mAh g^{-1} at 1C (240 mA g^{-1}) and 125 mAh g^{-1} at C/30 (8 mA g^{-1}) in the voltage range of 2.2 - 3.8 V and displayed 75% of the capacity after 50 cycles.[203, 204] The Fe-substituted $O3-Na[Ni_{1/3}Fe_{1/3}Mn_{1/3}]O_2$ exhibited the specific capacity of 100 mAh g^{-1} with average operating voltage at 2.75 V.[205] The isostructural

compound, $Na[Ni_{1/3}Mn_{1/3}Co_{1/3}]O_2$, showed reversible intercalation of 0.5 Na-ions leading to the specific capacity of 120 mAh g^{-1} in the voltage range of 2.0 - 3.75 V.[206] These relatively low capacity and limited cycling retention are presumably due to the fact that most of these materials undergo multiple phase transformations from O3 to O'3, P3, P'3 and then P''3 consecutively.[207] These transformations could be one of the major problems that limit the practical uses of Na-ion batteries since it deteriorates the cycle life and rate capabilities. Herein, to overcome this issue, a new O3 compound is prepared through Li-Na ion exchange, inspired by the idea in Li-ion batteries that Li-excess O3 compound has been demonstrated single slope voltage profile with significant improvement in capacity and cycling retention for Li layered electrodes.[208-210]

7.2. Experimental

A coprecipitation followed by two steps calcination was used for the synthesis of the O3 type Li-excess layered oxides.[65, 211] Transition metal (TM) nitrates, $Ni(NO_3)_2 \cdot 6H_2O$ (ARCROS, 99%), and $Mn(NO_3)_2 \cdot 4H_2O$ (Alfa Aesar, 98%) were dissolved into deionized water then titrated into $LiOH \cdot H_2O$ (Fisher) solution. The coprecipitated TM hydroxides were then filtered using vacuum filtration and washed three times with deionized water. The collected TM hydroxides were dried in an oven at 180°C for 10 h in air. The dried TM precursors were then mixed with a stoichiometric amount of $LiOH \cdot H_2O$ (Fisher) corresponding to the amount of $TM(OH)_2$ from the coprecipitation step. This mixture was ground for 30

min to ensure adequate mixing and then placed into a furnace at 480°C for 12 h. The precalcinated powders were then calcinated at 900 °C for 12 h in air.

Cathodes of as-prepared O3 type Li-excess layered oxides were prepared by mixing the active material with 10 wt % Super P carbon (TIMCAL) and 10 wt % poly(vinylidene fluoride) (PVDF) in N-methylpyrrolidone (NMP) solution. The slurry was cast onto an Al foil using a doctor blade and dried in a vacuum oven overnight at 80 °C. The electrode discs were punched and dried again at 80 °C for 6 h before storing them in an argon filled glovebox (H_2O level < 1 ppm). The average loading of active material is ~ 3 mg/cm^2. Then, the O3 type Na-excess layered oxides was prepared by ion-exchange. For example, the $Li_{1.133}Ni_{0.3}Mn_{0.567}O_w$ electrode which contains more lithium (y > 0.6) was charged with cut off voltage at 4.8 V (vs.Li metal, using 1M $LiPF_6$, 1:1 EC:DMC) and discharged with cut off voltage 1.5 V (vs.Na metal, using 1M $NaPF_6$, 1:1 EC:DEC), thus O3 type $Na_{0.8}Li_{0.14}Ni_{0.3}Mn_{0.567}O_w$ electrode which contains more sodium (x > 0.6) electrode was obtained.

For the full cell fabrication, we chose SnS_2/rGO as anode with ~ 10 % excess amount. The anode consisted of 80 wt % SnS_2/rGO, 10 wt % of conducting additive (acetylene black), and 10 wt % CMC binder. Before assembled into the full cell, the cathode was delithiated, and the anode was sodiated.

Electrochemical properties were measured on an Arbin battery cycler in galvanostatic mode between 4.2 and 1.5 V. The 2016 coin cells were prepared in the Argon filled glovebox (H_2O < 0.1 ppm) using sodium metal ribbon as an

anode and a 1 M $NaPF_6$ in a 1:1 ethylene carbonate/diethyl carbonate (EC:DEC) electrolyte solution. Glass fiber D separators were used as the separator. For full cell: Electrochemical properties were measured on an Arbin battery cycler in galvanostatic mode between 4.2 and 1 V. The 2032 coin cells were prepared in the Argon filled glovebox (H_2O < 0.1 ppm) using SnS_2/rGO as an anode and a 1 M $NaPF_6$ in a 1:1 ethylene carbonate/diethyl carbonate (EC:DEC) electrolyte solution. Glass fiber D separators were used as the separator. The cycled samples were recovered by disassembling cycled batteries in the same argon-filled glovebox. The cathode was washed with DMC 3 times and then allowed to dry in argon atmosphere overnight.

XAS measurements were carried out at the PNC-XSD bending magnet beamline (20-BM) of the Advanced Photon Source. Measurements at the Ni and Mn K- edge were performed in the transmission mode at room temperature using gas ionization chambers to monitor the incident and transmitted X-ray intensities. A third ionization chamber was used in conjunction with Mn / Ni-foil standards to provide internal calibration for the alignment of the edge position. Monochromatic X-rays were obtained using a fixed-exit Si (111) double crystal monochromator. Energy calibration was carried out using the first derivative of the spectra of the Ni and Mn metal foils. The data were analyzed and refined using the Ifeffit [212] and Horae [213] packages. The radial structure function was obtained by Fourier transform of the normalized k^2-weighted EXAFS spectra with a k range of 3.0 – 12.0 Å^{-1} for Ni and 2.0-12.0 Å^{-1} for Mn respectively.

The samples for XRD were obtained by disassembling cycled batteries in an argon-filled glovebox. The cathode was washed by battery grade dimethyl carbonate (DMC) 3 times and dried. The cathode film was sliced into thin pieces and mounted in the hermitically sealed capillary tubes for ex-situ XRD. Powder diffractions of all samples were taken using synchrotron XRD at the Advanced Photon Source (APS) at Argonne National Laboratory (ANL) on beamline 11-BM (λ = 0.459 Å). The beamline uses a sagittal focused X-ray beam with a high precision diffractometer circle and perfect Si(111) crystal analyzer detection for high sensitivity and resolution. XRD patterns were analyzed by Rietveld refinement method using FullProf software.[214]

7.3. Results and Discussion

The $Li_{1.133}Ni_{0.3}Mn_{0.567}O_2$ was synthesized by heating a mixture of $LiOH \cdot H_2O$ and $Ni_{0.346}Mn_{0.654}(OH)_2$. The obtained $Li_{1.133}Ni_{0.3}Mn_{0.567}O_2$ was firstly charged in the Li half cell to extract Li ions (the composition at this point is $Li_{0.073}Ni_{0.3}Mn_{0.567}O_w$) and then discharged in the Na half cell to prepare O3 – $Na_{0.719}Li_{0.073}Ni_{0.3}Mn_{0.567}O_w$. (Figure 7.1) To achieve higher capacity, the ratio among Li, Ni and Mn was further adjusted and the composition, $Li_{1.167}Ni_{0.25}Mn_{0.583}O_2$ was finally chosen, which improved the initial Na-insertion capacity from 220 mAh g^{-1} to 240 mAh g^{-1}. Figure 7.2 (a) illustrates the electrochemical profiles for the initial "delithiation" (Li-extraction) and "sodiation" (Na-extraction) processes for $Li_{1.167}Ni_{0.25}Mn_{0.583}O_2$. The initial "delithiation" of Li-excess material showed a long plateau at 4.5V which involved oxygen loss

(and/or oxidation). The stoichiometry for the ion-exchanged material is $Na_{0.78}Li_{0.18}Ni_{0.25}Mn_{0.583}O_w$, as determined by the electrochemical capacity and energy-dispersive X-ray spectroscopy. We used subscript w (0 < w <2) in the formula to describe the oxygen loss during initial charge. The as-prepared $Na_{0.78}Li_{0.18}Ni_{0.25}Mn_{0.583}O_w$ has particle size less than 500 nm, retaining same morphology with it parent material, $Li_{1.167}Ni_{0.25}Mn_{0.583}O_2$. (Figure 7.3) The cycling performance is tested between 1.5 and 4.2 V with current density at 125 mA g^{-1}. After 30 cycles, around 190 mAh g^{-1} capacity is well maintained as shown in Figure 7.2 (b). With 1.25 A g^{-1} current, the reversible capacity is still as high as 160 mAh g^{-1}, suggesting its high-power capability. (Figure 7.4) Figure 7.2 (c) compares capacity and energy density for most of the recent cathodes in Na-ion batteries (highest reversible value is selected.) The $Na_{0.78}Li_{0.18}Ni_{0.25}Mn_{0.583}O_w$ exhibits not only the highest capacity but also the highest energy density: 675 Wh kg^{-1} energy density is delivered by this materials during discharge, which is higher than recent results reported by Kataoka R. et. al. who used similar ion exchange method,[215] and even higher than $LiFePO_4$ (560 Wh kg^{-1}) and $LiCoO_2$ (560 Wh kg^{-1}) in Li-ion batteries.[216-218] More interestingly, as displayed in the inset of Figure 7.2 (b), no voltage steps are seen in the electrochemical profiles upon cycling. It indicates the no phase transformations happen for this O3 material even after all the Na ions are extracted. Besides, the voltage depression problem which is usually observed in its parent material, $Li_{1.167}Ni_{0.25}Mn_{0.583}O_2$ in Li-ion batteries,[219] is reduced to some degree in this ion-exchanged product in Na-ion batteries.

The synchrotron X-ray Diffraction (SXRD) was conducted at selected states of charge/discharge to detect the structural change. (Figure 7.5 (a)) The refined lattice parameters were summarized at Table 7.1. As shown with the black line in Figure 7.5 (a), the as-synthesized material, $Li_{1.167}Ni_{0.25}Mn_{0.583}O_2$, is well crystallized and can be indexed as R-3m space group. The diffraction pattern illustrates typical Li-excess features, which have been discussed by our previous work.[219] After initial delithiation (red line in Figure 7.5 (a)), the c lattice is slightly increased (Table 7.1) due to less screening effect between neighboured oxygen layers when Li ions are mostly removed from the host.[220] Upon initial sodiation (green line in Figure 7.5 (a)), the whole spectrum is significantly shifted to lower angle, such as (003) and (110) peak. The shift is resulted from the overall lattice expansion, as the inserted Na ions have much large ionic size than Li ions. Peak broadening is observed, which is probably ascribed to the stacking faults introduced during initial sodiation. The small reflection to the right of the (003) peak is probably the non-reacted residue Li compound phase. More work is undergoing to comprehensively investigate this process. It should be noted that although the diffraction peaks are moved systematically, all the peaks still belong to R-3m space group, in other words, O3 phase (Figure 7.5 (b)), proving that there is no change in the host structure during ion-exchange process. To further monitor the electrode structural change upon cycling in Na batteries, two ex-situ samples were characterized. When the electrode is charged to 4.2 V (pink line in Figure 7.5 (a)), the material is still maintained at O3 structure though the majority of Na ions are removed as suggested by charging capacity. Comparing with the

material after initial sodiation, it is interesting to notice the (003) peak is moved to higher angle, indicating that c lattice is reduced at this state. Moreover, all the peaks positions are close to those of the material after initial delithiation. Since Li moving to tetrahedral sites after first charge has been extensively observed in Li-ion batteries,[77, 219, 220] it is hypothesized that the tetrahedral Li would form similarly in our initial delithiation process as shown in Figure 7.5 (c). These tetrahedral Li ions play a critical role in stabilizing the O3 phase at subsequent cycles by locking the neighboured layer shifting. When the electrode is discharged to 1.5 V (blue line in Figure 7.5 (a)), the spectrum is back to the similar positions with the material after initial sodiation, suggesting that the Na ions are re-inserted back reversibility. And most importantly, the O3 phase is still well maintained.

In order to investigate the charge compensation mechanism during Na-ions extraction and insertion, X-ray absorption spectroscopy (XAS) measurements were conducted with Ni and Mn K-edges at different state of charge. Normalized Ni and Mn K-edge X-ray absorption near edge structure (XANES) spectra are shown in Figure 7.6 (a) and 7.6 (b), respectively. For the standards, Ni K-edge spectra of divalent Ni-ion (NiO) and Mn K-edge spectra of tetravalent Mn-ion (MnO_2) are included. It is evident that as-synthesized $Li_{1.167}Ni_{0.25}Mn_{0.583}O_2$ compound predominantly consists of Ni^{2+} and Mn^{4+}. Obvious changes are shown in the Ni XANES spectra upon the initial delithiation, sodiation, and followed charge and discharge process. The Ni K-edge absorption energy of initially delithiated electrode shifts to the higher energy region

compared to that of as-synthesized state. The amount of absorption energy shift is ~3 eV, suggesting that oxidation state of Ni after initial delithiation is close to Ni^{4+}.[219] After initial sodiation, the oxidation state of Ni ions returns back to divalent. The similar edge shift and recover are seen again between 4.2 V and 1.5 V ex-situ electrode samples suggesting that the Ni^{2+}/Ni^{4+} redox reaction is completely reversible in Na-ion batteries. In contrast to the Ni XANES, Mn K-edge XANES shows that Mn ions mainly stay at tetravalent state and no dramatic changes are occurred in the valence upon the charge and discharge. The subtle variations in edge shape and position in XANES could be attributed to surface reaction of the particle, which has been reported in its Li analogue[169] and requires more advanced characterization to investigate. Based on the Ni and Mn XANES, it is proved that Ni is the only electrochemically active species and Mn supports the structural stability in the absence of Jahn-Teller active Mn^{3+}. More details on local structural change are revealed by the extended X-ray absorption fine structure (EXAFS) spectra. Ni EXAFS clearly shows that interatomic distances of Ni-O and Ni-TM are shortened after the initial delithiation and after the charge in Na-ion batteries, indicating that the oxidation of Ni ions. After initial sodiation, the interatomic distances are systematically larger than the as-synthesized state, resulted from lattice expansion when Na ions are inserted. However, Mn EXAFS does not show any significant changes in the Mn-O interatomic distance (small changes may be due to the local environment changes), although the second shell corresponding to Mn-TM distance is varied with different voltages. This is ascribed to the changes in the Ni oxidation states,

which accordingly affect the distance among neighboured Mn-Ni.

To evaluate the practical application of $Na_{0.78}Li_{0.18}Ni_{0.25}Mn_{0.583}O_w$, the full cell was fabricated with $Na_{0.78}Li_{0.18}Ni_{0.25}Mn_{0.583}O_w$ as cathode and SnS_2 / rGO as anode. (Figure 7.7 (a)) The anode is reported by our previous work.[221] In our full cell configuration, both cathode material and anode material are casted on Al current collector, which will further reduce the cost and weight of Na ion battery. Upon charging, Na ions are extracted from the cathode and inserted into the anode. During discharge, Na ions are transferred reversely. By this process, the energy storage and released reversibly. Figure 7.7 (b) represents voltage profiles of the full cell which shows a discharge capacity of ~210 mAh / g (capacity based on cathode weight). The overall capacity of Na full cell using our advanced cathode and anode can reach 175 mAh / g (considering the weight of cathode and anode materials). The operation discharge voltage is on average 2.5 V. As a result, the total energy density for this Na full cell is as high as 430 Wh / kg, which is to our best knowledge the highest energy so far reported for Na full cells. Furthermore, the capacity is well maintained for this Na full cell. As shown in Figure 7.7 (c), after 50 cycles, more than 165 mAh g^{-1} is delivered reversibly.

In fact, the ion-exchanged electrode performance could be further adjusted by mixing with other TM, such as Co. As shown in Figure 7.8 (a), if the parent Li compound is designed with Co in the stoichiometry as $Li_{1.167}Ni_{0.166}Mn_{0.5}Co_{0.166}O_2$, the discharged capacity is further increased to 245 mAh g^{-1}. In addition, the direct synthesis route has been tried preliminarily. The as-synthesized material, $NaLi_{0.067}Co_{0.267}Ni_{0.267}Mn_{0.4}O_2$, has demonstrated pure

O3 phase. However, the direct synthesis by co-precipitation method will be hard to create tetrahedral Li, we can not exclude the possibilities from other method, more efforts are under development now.

7.4. Conclusions

In conclusion, a new O3 - $Na_{0.78}Li_{0.18}Ni_{0.25}Mn_{0.583}O_w$ is obtained by the electrochemical Na-Li ion exchange process of $Li_{1.167}Ni_{0.25}Mn_{0.583}O_2$. The new material shows exceptionally high discharge capacity of 240 mAh g^{-1} in the voltage range of 1.5-4.5 V, thus the total energy density at the materials level reaches 675 Wh kg^{-1}. It is the highest capacity as well as highest energy density so far among all the reported cathodes in Na-ion batteries. When cycled between 1.5-4.2 V, the discharge capacity is well maintained around 190 mAh g^{-1} after 30 cycles. The O3 phase is kept through ion-exchange and cycling process, as confirmed by SXRD. The stabilized O3 phase could be related to the tetrahedral Li formed upon initial lithiation, and breaks through the critical limitation for most of the O3 compounds. XAS results show that Ni^{2+}/Ni^{4+} is the main active redox couple during cycling while Mn ions basically stay at tetravalent state. The Na full cell utilizing $Na_{0.78}Li_{0.18}Ni_{0.25}Mn_{0.583}O_w$ as cathode delivers Wh kg^{-1} energy density, shedding light on the future of the Na-ion technologies. Future improvement could be realized through fine tuning the combination and ratio among TMs, and making the material by direct synthesis, which will be reported very soon.

Chapter 7, in part, is a reprint of the material "A new O3-type layered oxide cathode with high energy / power density for rechargeable Na batteries" as it appears in the Chemical Communications, Haodong Liu, Jing Xu, Chuze Ma, Ying Shirley Meng, Chemical Communications, 2015, 51,4693. The dissertation author was the primary investigator and author of this paper. All experiments and data analysis were performed by the author except for the XAS part, SXRD data collection, and SnS_2/rGO anode preparation.
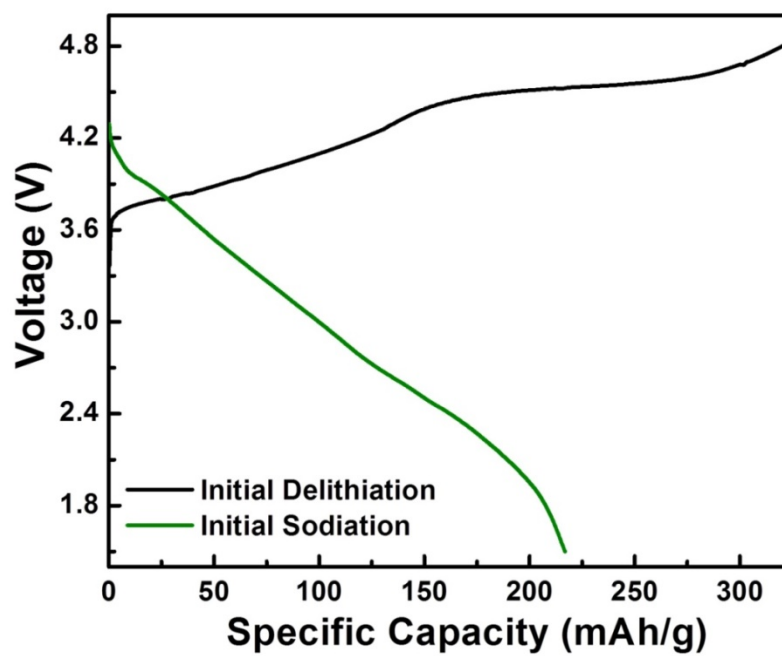
Figure 7.1   Electrochemical   profile   for $Li_{1.133}Ni_{0.3}Mn_{0.567}O_2$ during   initial delithiation and initial sodiation.
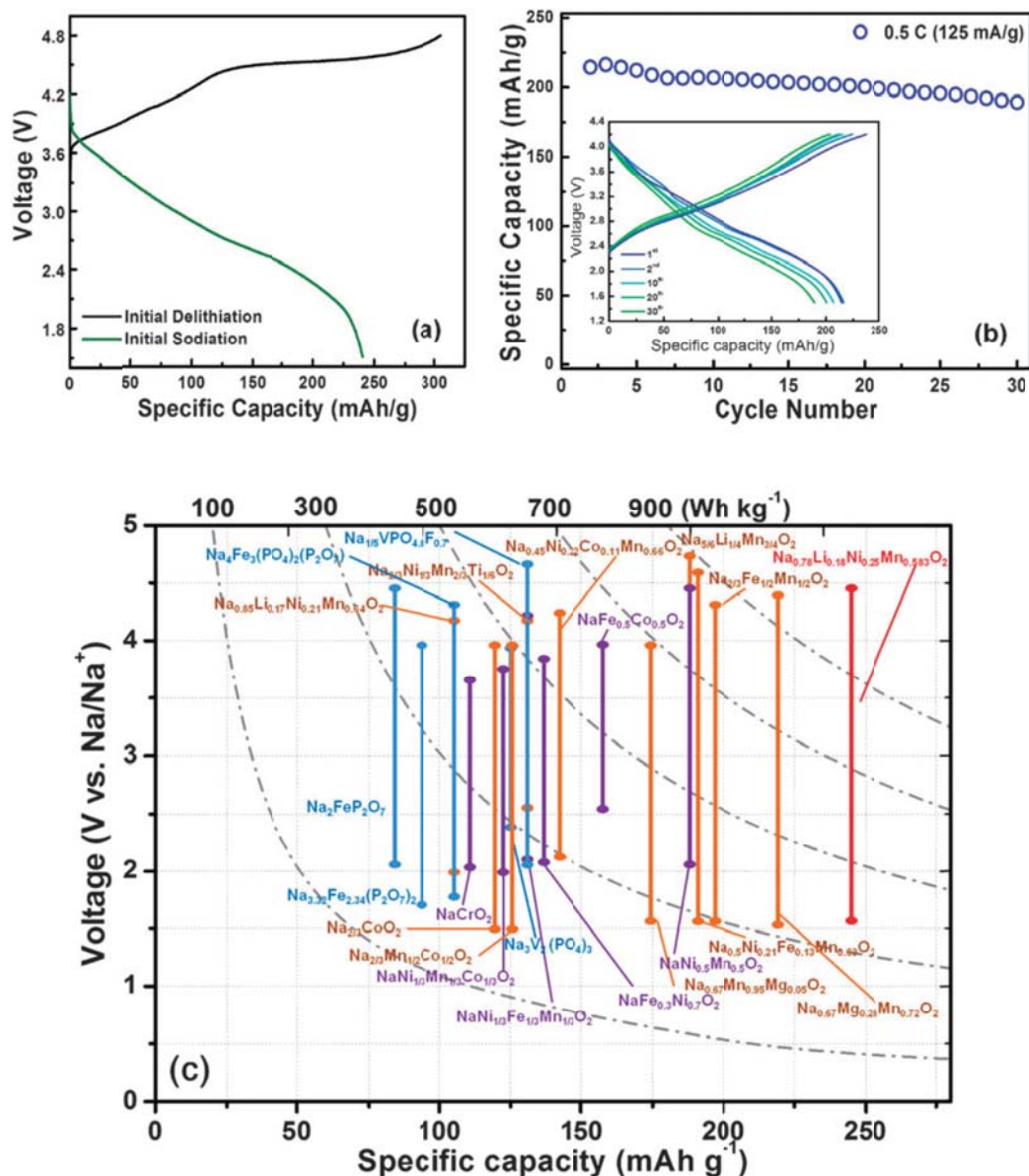
Figure 7.2 (a) Electrochemical profiles of initial delithiation and initial sodiation for $Na_{0.78}Li_{0.18}Ni_{0.25}Mn_{0.583}O_w$ in half cell. (b) Cycling performance for $Na_{0.78}Li_{0.18}Ni_{0.25}Mn_{0.583}O_w$ with 125 mA g^{-1} current density. Inset is the corresponding electrochemical profile of $Na_{0.78}Li_{0.18}Ni_{0.25}Mn_{0.583}O_w$ during the 1st, 2nd, 10th, 20th, 30th cycles in Na-ion batteries. (c) Comparison of reversible capacities for the intercalation-based Na cathodes.[199, 206, 222-241]
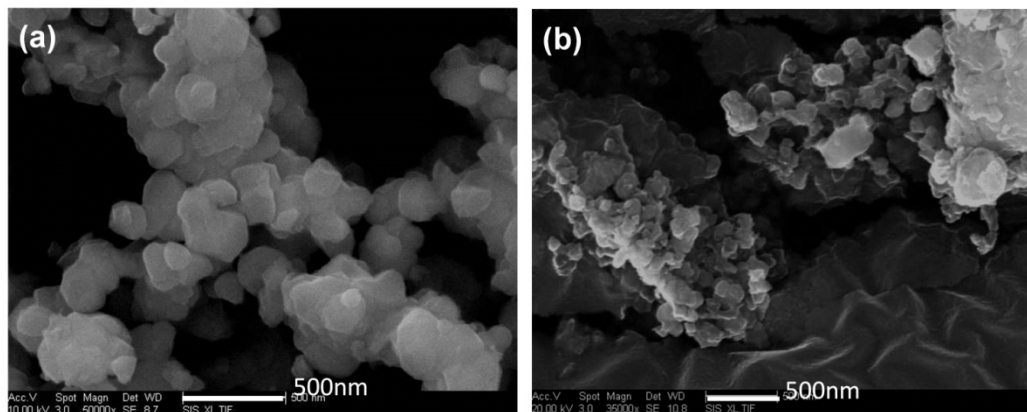
Figure 7.3   SEM images for (a) as-synthesized $Li_{1.167}Ni_{0.25}Mn_{0.583}O_2$ and (b) $Na_{0.78}Li_{0.18}Ni_{0.25}Mn_{0.583}O_w$.
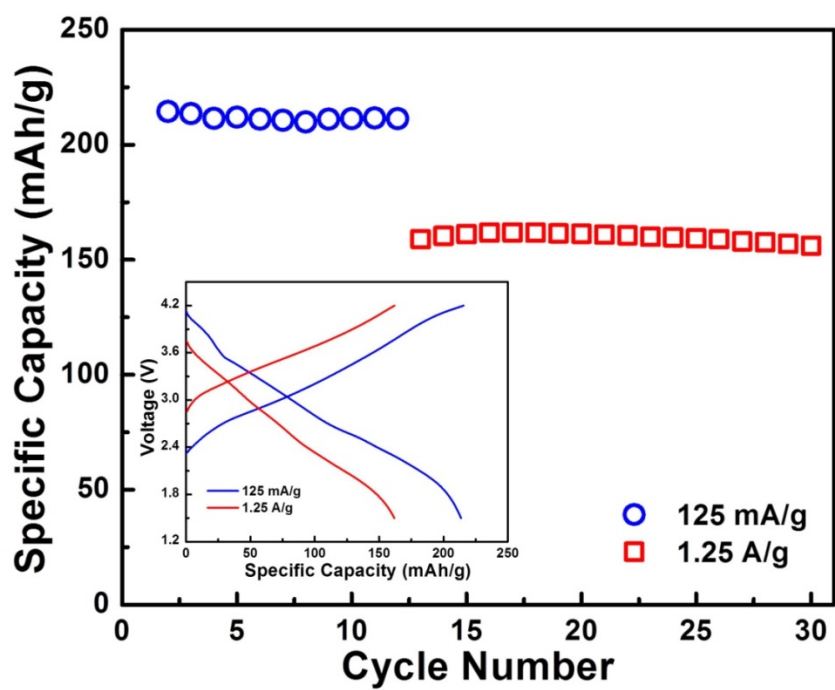
Figure 7.4 Rate performance for $Na_{0.78}Li_{0.18}Ni_{0.25}Mn_{0.583}O_w$.
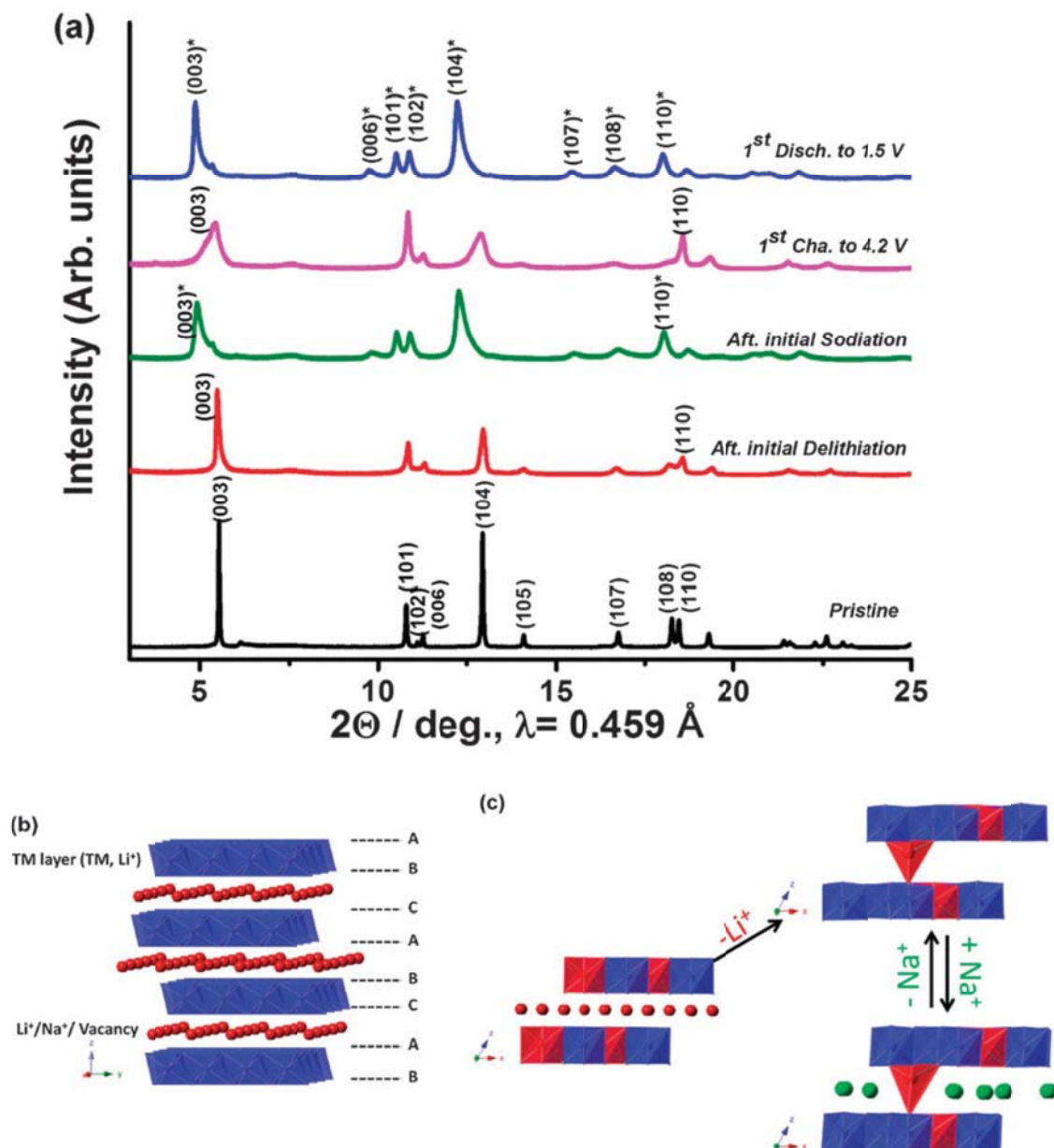
Figure 7.5 (a) Ex situ SXRD for $Li_{1.167}Ni_{0.25}Mn_{0.583}O_2$ and $Na_{0.78}Li_{0.18}Ni_{0.25}Mn_{0.583}O_w$ at different states. (b) Schematic of the typical O3 structure. (c) Schematic of the proposed mechanism for sodiation. (In the schematic, transition metal ions are blue, Li^+ is red, and Na^+ is green.)
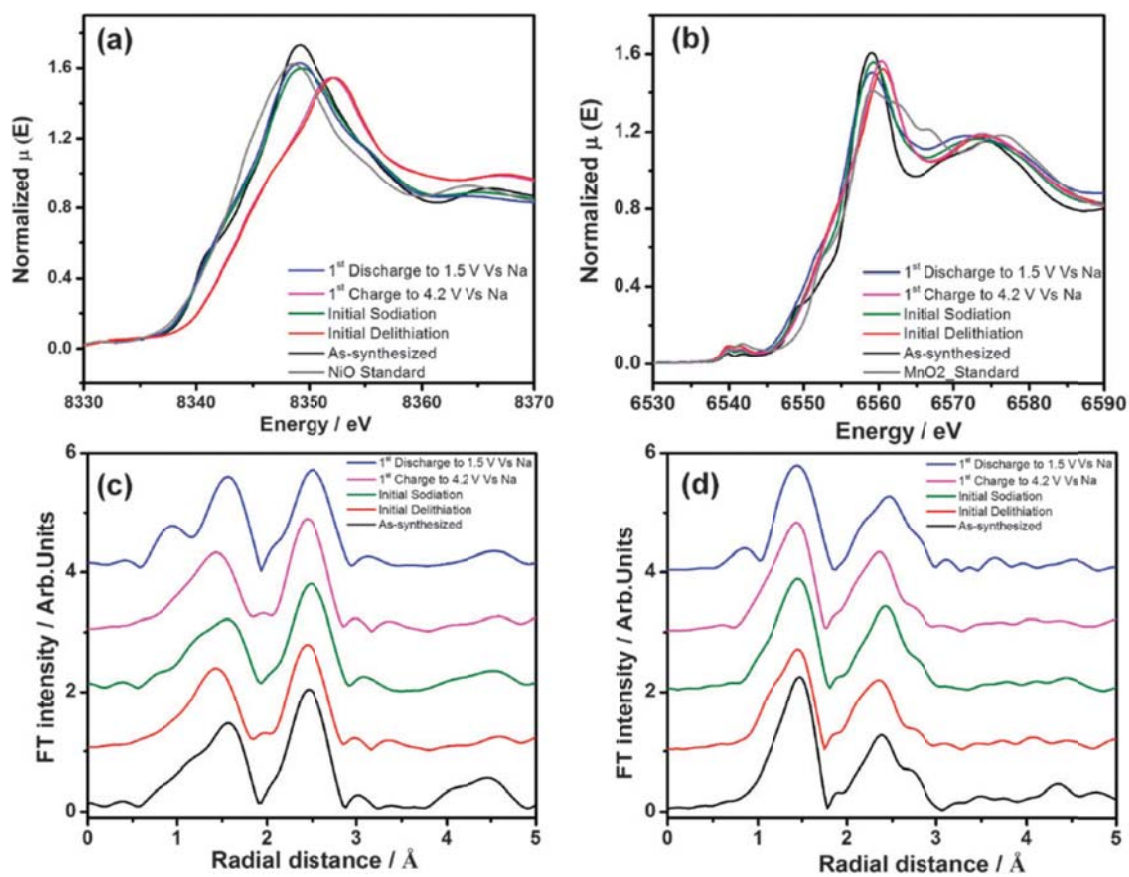
Figure 7.6 XAS analysis for $Li_{1.167}Ni_{0.25}Mn_{0.583}O_2$ and $Na_{0.78}Li_{0.18}Ni_{0.25}Mn_{0.583}O_w$ at different states. XANES spectra for (a) Ni and (b) Mn K-edge respectively. EXAFS spectra for (c) Ni and (d) Mn K-edge respectively.
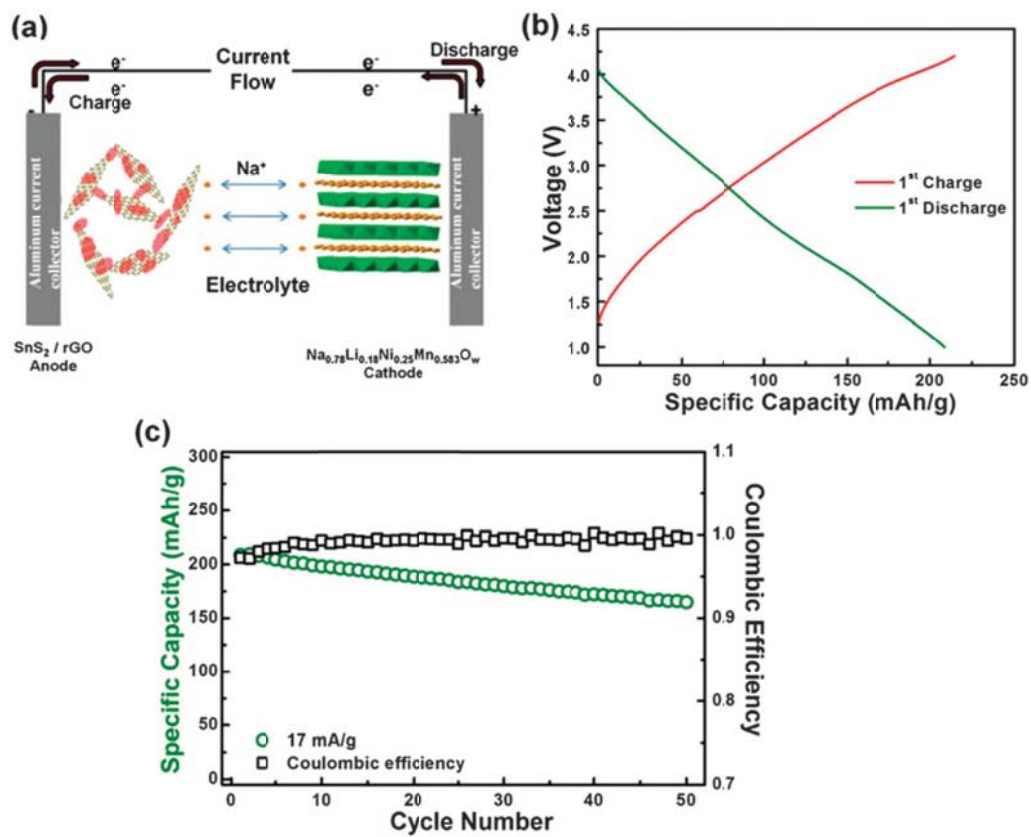
Figure 7.7 (a) Schematic of Na full cell. (b) The electrochemical profile at 1st cycle and (c) cycling performance for the Na full cell.
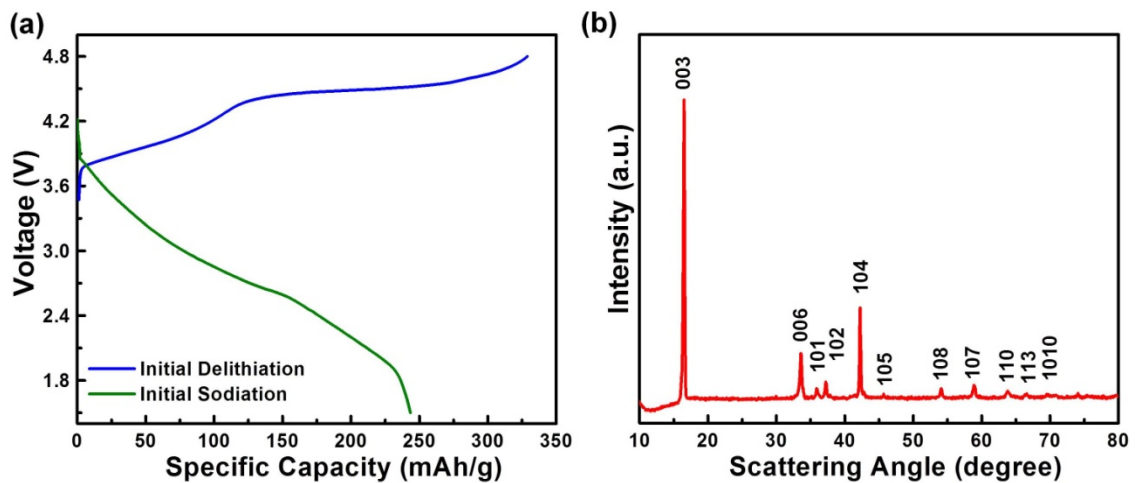
Figure 7.8 (a) The electrochemical profile for $Li_{1.167}Ni_{0.166}Mn_{0.5}Co_{0.166}O_2$ during initial delithiation and initial sodiation. (b) XRD for as-synthesized $NaLi_{0.067}Co_{0.267}Ni_{0.267}Mn_{0.4}O_2$.

Table 7.1   Refined lattice parameter for $Li_{1.167}Ni_{0.25}Mn_{0.583}O_2$ and $Na_{0.78}Li_{0.18}Ni_{0.25}Mn_{0.583}O_w$ at different states.

	a (Å)	c (Å)
1st discharge	2.9343	16.2007
1st charge	2.8484	14.4783
Initial Sodiation	2.9316	16.0590
Initial Delithiation	2.8485	14.3886
As-synthesized	2.8643	14.2588

Chapter 8. Exploring Li substituted O3-structured layered oxides NaLi$_x$Ni$_{1/3-x}$Mn$_{1/3+x}$Co$_{1/3-x}$O$_2$ (x= 0.07, 0.13, and 0.2) as promising cathode materials for rechargeable Na batteries

A series of new O3 cathode materials, NaLi$_x$Ni$_{1/3-x}$Mn$_{1/3+x}$Co$_{1/3-x}$O$_2$ (x= 0.07, 0.13, and 0.2), are explored by substituting Li in the layered structure. Single phase is achieved at low Li content (x = 0.07) while the increase in the amount of Li leads to impurity phase. The optimized composition, NaLi$_{0.07}$Ni$_{0.26}$Mn$_{0.4}$Co$_{0.26}$O$_2$, demonstrates good capacity retention and excellent rate performance. *Ex-situ* synchrotron XRD suggests that the O3 phase is maintained upon cycling, thus results in the excellent performance. X-ray Absorption Spectroscopy data shows that Ni^{2+} / Ni^{4+} is the main redox couple while Co^{3+} / Co^{4+} partially contributes to balancing the charge.

8.1. Introduction

Rechargeable Na batteries have recently drawn increasing attention as promising candidates for large scale stationary energy storage systems, due to the broad distribution and high natural abundance of sodium raw materials. Among most of the Na cathodes reported to date, the O3 structured Na oxides (Na$_x$MO$_2$, M = Transition Metal) have attracted considerable interest, because their structures are able to accommodate large Na ions and provide spacious

diffusion path.[87, 93, 198, 201, 242-246] Although significant improvement has been achieved, the O3 structure materials still suffer from multiple phase transformations from O3 to O'3, P3, P'3 and then P''3 consecutively, that severely deteriorates the structural integrity and performance reversibility.[247] To overcome these issues, novel cathode materials are needed. Considering for P2-structured cathodes which are another family of layered material as electrode candidates for Na-ion batteries, several Li-substituted materials have been reported with the suppressed phase transformation.[87, 248, 249] Furthermore, our group has shown that the excess Li ions also play a significant role in improving the capacity of traditional layered oxides as cathode for Li-ion batteries.[250] Herein, in this work we substitute Li in the O3-structured Na oxides to explore its effect on the battery performance. The materials with good capacity retention / rate performances are obtained. The crystal and electronic structural changes upon cycling are characterized.

8.2. Experimental

A co-precipitation method was used for the synthesis of transition metal hydroxides as precursor for the O3 type Li substituted Na layered oxides.[251] The obtained TM hydroxides were then mixed with Na_2CO_3 (Fisher, 5% excess) and Li_2CO_3 (Fisher) by the stoichiometric ratio and calcinated at 1000 °C for 24h in air. Electrochemical measurement, XAS and XRD characterization are described with details in our previous work.[146]

8.3. Results and discussions

A series of Li substituted Na layered oxides were synthesized. The XRD patterns in Figure 8.1 (a) compare the crystal structures of different compositions. All the major peaks adopted to the parent hexagonal structure with R$\bar{3}$m space group.[146] For the compounds with high Li content, NaLi$_{0.2}$ (in black) and NaLi$_{0.13}$ (in red), extra peaks are observed around 18º, suggesting some impure phases presumably due to large amount of excess Li, which may be associate with LiTMO$_x$. We decreased the Li amount during synthesis, then achieved phase pure NaLi$_{0.07}$Ni$_{0.26}$Mn$_{0.4}$Co$_{0.26}$O$_2$. In the O3 structure (Figure 8.1 (b)), all the cations sit in octahedral sites, coordinated by 6 nearest oxygen ions. The Na layers and TM layers are alternatively located between two neighboring oxygen layers. Considering the size similarity between Li ion and TM ions, we propose these substituted Li ions are located in TM layers.[146] The SEM image in Figure 8.1 (c) illustrates that the as-synthesized NaLi$_{0.07}$Ni$_{0.26}$Mn$_{0.4}$Co$_{0.26}$O$_2$ agglomerates into plate-like secondary particles.

The pure phase NaLi$_{0.07}$Ni$_{0.26}$Mn$_{0.4}$Co$_{0.26}$O$_2$ was selected to explore the electrochemical performances. The first cycle of this material was performed between 1.5V to 4.5V at 25 mA g^{-1} current density. The material delivers a capacity of 181 mAh g^{-1} in the first charging, followed by 147 mAh g^{-1} in the first discharging. The irreversible capacity in the first cycle is believed to be related to the oxygen evolution, as suggested by the electrochemical profile. (Figure 8.1 (d)) The long, irreversible plateau at 4.2 V (vs Na anode) in the first charging process

has been observed in most Li-excess cathodes (4.5V in Li-excess cathode vs Li anode) for LIBs, which were mainly attributed to the oxygen loss from the lattice.[66, 251] After 50 cycles, the capacity is well maintained at 128 mAh g^{-1}. When the battery is tested at 125 mA g^{-1}, the material could still deliver around 110 mAh g^{-1} and the capacity retention is above 98 % after 50 cycles. (Figure 8.1 (e)) In addition to the good performance retention, superior rate capabilities are obtained as well: as shown in the Figure 1e inset, even with 500 mA g^{-1} current, the reversible capacity is still as high as 80 mAh g^{-1}, suggesting its high-power capability. More interestingly, we don't see any pronounced voltage steps in its electrochemical profiles (Figure 8.1 (d)) as observed in majority of O3-structred cathodes. It indicates that the phase transformations are partially suppressed for this O3 material even up to 4.5V. Its cycling stability within a wide voltage window surpasses most of other Na layered O3 oxides due to the existence of substituted Li in the lattice stabilizing the structure through cycling.

The synchrotron X-ray Diffraction (SXRD) was collected at selected states along voltage profiles to characterize the structural change. As shown with the red line in Figure 8.2, the as-synthesized material, $NaLi_{0.07}Ni_{0.26}Mn_{0.4}Co_{0.26}O_2$, has good crystallinity. Before 4.2V, no flat voltage plateau is observed indicating there is no first-order phase transformation. When the electrode is charged to 4.2V (orange line in Figure 8.2), both hydrated and non-hydrated O3 phase are observed. The hydrated O3 phase is happened during XRD measurement, and facilitated by c lattice expansion due to less screening effect between neighbored oxygen layers when most Na ions are extracted.[251] At the end of first charge

(4.5 V), the hydrated O3 phase dominates the structure. Upon the first discharge (green line in Figure 8.2), the whole spectrum is systematically shifted back to higher angle than the fully charged state, such as (003); and we only observed the O3 Li-substituted Na phase. When the electrode is charged to 4.5 V in the second cycle, the hydrated O3 phase appears again. After discharging to 1.5 V, the O3 Li-substituted Na phase is observed at the end of second cycle and even after 50 cycles. All the peaks positions are close to those of the pristine material. Such good phase stability is the main reason for our excellent capacity retention and rate performance. In addition, although small plateaus are seen in the electrochemical profiles, no phase changes are detected by SXRD during cycling. Thus those small steplike features could be resulted from transitions between different Na-ion in-plane orderings, which have been broadly noticed in most Na layered materials. As known to all that some Li atoms moving to tetrahedral sites after first charging has been in layered cathode materials for Li-ion batteries, it is hypothesized that the tetrahedral Li would form likewise in our first charge.[250] These tetrahedral Li ions have essential effect in stabilizing the O3 phase at subsequent cycles by pinning down the neighbored layers.

To understand the charge compensation mechanism upon cycling, X-ray absorption spectroscopy (XAS) measurements were conducted at selected states of charge. Normalized Ni, Co and Mn K-edge X-ray absorption near edge structure (XANES) spectra are plotted in Figure 8.3 (a), 8.3 (b) and 8.3 (c), respectively. It is clear that the pristine $NaLi_{0.07}Ni_{0.26}Mn_{0.4}Co_{0.26}O_2$ compound predominantly consists of mixed Ni^{2+} and Ni^{3+} (small amount of Ni^{3+} exists due to

the Na loss during high temperature calcination), Co^{3+} and Mn^{4+}. There are systematic changes in the Ni XANES spectra with different voltages along the electrochemical profile. In the first charge, the Ni K-edge absorption energy shifts to the higher energy than that at the as-synthesized state, suggesting that oxidation state of Ni after first desodiation is close to Ni^{4+}.[97, 248, 250] After first full cycle, the oxidation state of Ni ions returns back to divalent. The similar edge shift and recover are observed in the second cycle consistently, demonstrating that the Ni^{2+}/Ni^{4+} redox reaction is reversible. The Co K-edge moves to higher energy towards the end of charge and returns back after discharge, while Mn K-edge XANES proves that Mn ions are maintained at tetravalent state upon cycling. Based on theses, we could conclude that Ni and Co are the electrochemically active species and Mn assists the structural stability owing to the absence of Jahn-Teller distortion from Mn^{3+}. Another point which should be noted is that in the first cycle, the edge positions for Ni, Co and Mn have no evident change above 4.2 V. This is consistent with our hypothesis that the irreversible capacity could result from the oxygen loss from the lattice. Similar phenomenon has been reported for Li-excess cathodes in Li-ion batteries as well.[66, 251] Further investigation on oxygen evolution in Na cathodes is still undergoing.

Based on the above discussions, the substituted Li in the structure helps to prevent phase transformation, thus minimize the structure degradation. Although the underlying role of Li in stabilizing the P2 structure has been revealed,[248] the exact mechanism in O3 cathodes is still unclear, given that the

phase transformation routes and cation sites are intrinsically different between P2 and O3 and structures. For future work, a suite of advanced characterization tools should be applied to understand Li contribution, including identifying the site variation of Li, monitoring the content of Li, and detecting the Li local environment and distribution upon charge / discharge. At the same time, more effort should be spent to develop Co free Li-substituted O3 cathodes for rechargeable Na batteries, in order to further reduce the cost of raw materials.

8.4. Conclusion

A new Li substituted Na layered oxide with pure O3 phase, $NaLi_{0.07}Ni_{0.26}Mn_{0.4}Co_{0.26}O_2$, is successfully achieved, demonstrating a considerably high reversible capacity of 147 mAh g^{-1} and excellent rate performance. The phase is stabilized throughout the cycling, which could be the main reason for its good electrochemical properties. Ni^{2+} / Ni^{4+} is the main active redox couple during cycling, and Co^{3+} / Co^{4+} partially contributes to the charge compensation. The findings would contribute to the future improvement and design of practical cathode materials for Na-ion batteries.

Chapter 8, in full, is a reprint of the material "Exploring Li substituted O3-structured layered oxides $NaLi_xNi_{1/3-x}Mn_{1/3+x}Co_{1/3-x}O_2$ (x= 0.07, 0.13, and 0.2) as promising cathode materials for rechargeable Na batteries" as it appears in the Electrochemistry Communications, Jing Xu, Haodong Liu, and Ying Shirley Meng, Electrochemistry Communications, 2015, 60, 13. The dissertation author was the co-primary investigator and co-author of this paper. All experiments and data

analysis were performed by the author except for the XAS part, and SXRD data collection.
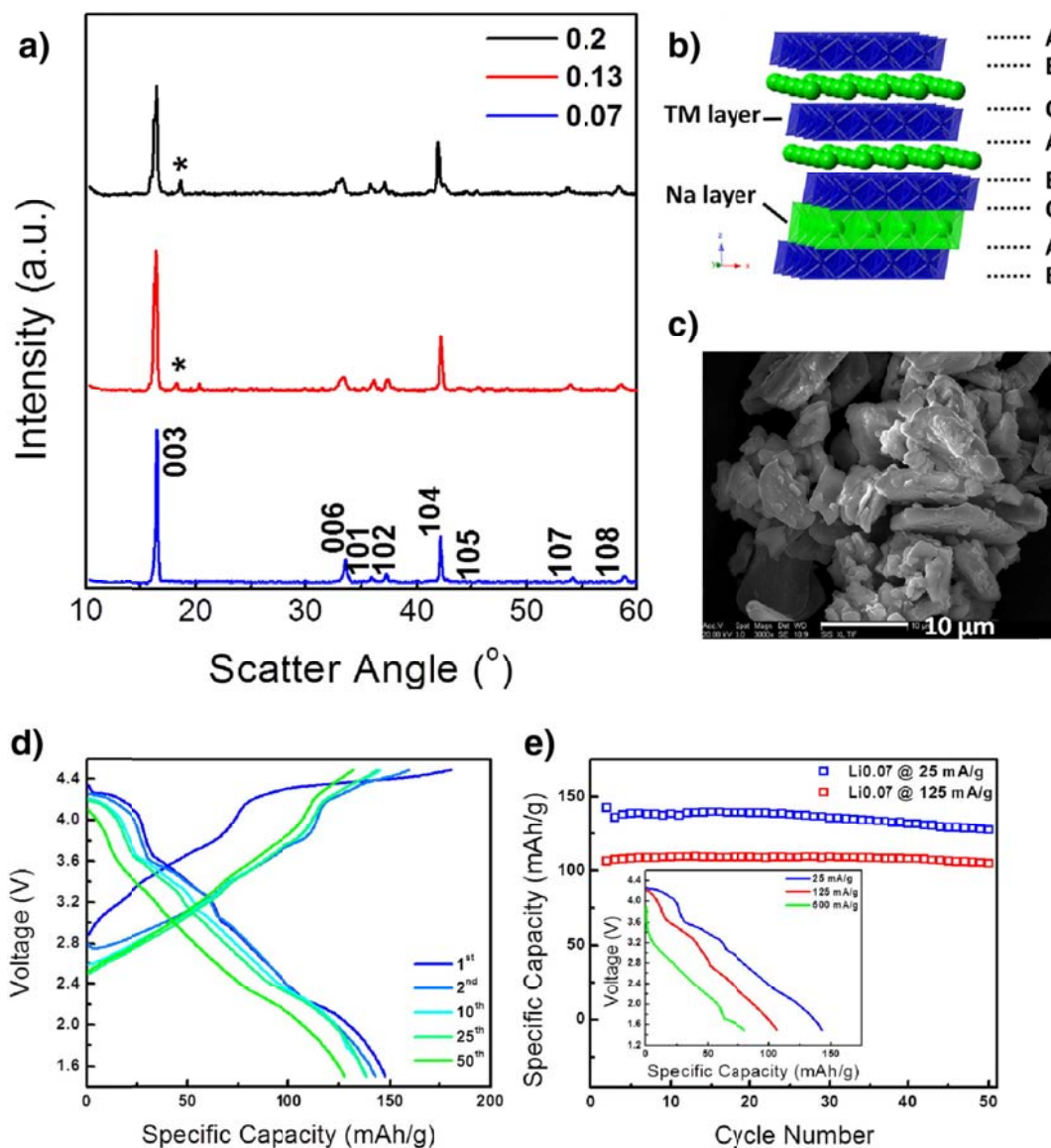
Figure 8.1 (a) Powder XRD for NaLi$_x$Ni$_{1/3-x}$Mn$_{1/3+x}$Co$_{1/3-x}$O$_2$ (x= 0.07, 0.13, and 0.2). (* is the peak from impurity phase) (b) Schematic of the typical O3 structure. (c) SEM of the NaLi$_{0.07}$Ni$_{0.26}$Mn$_{0.4}$Co$_{0.26}$O$_2$. (d) Electrochemical profiles of NaLi$_{0.07}$Ni$_{0.26}$Mn$_{0.4}$Co$_{0.26}$O$_2$ in half cell. (e) Cycling performance for NaLi$_{0.07}$Ni$_{0.26}$Mn$_{0.4}$Co$_{0.26}$O$_2$ at different current densities. Inset is the electrochemical profiles of NaLi$_{0.07}$Ni$_{0.26}$Mn$_{0.4}$Co$_{0.26}$O$_2$ at 25 mA g^{-1}, 125 mA g^{-1}, and 500 mA g^{-1} current density.
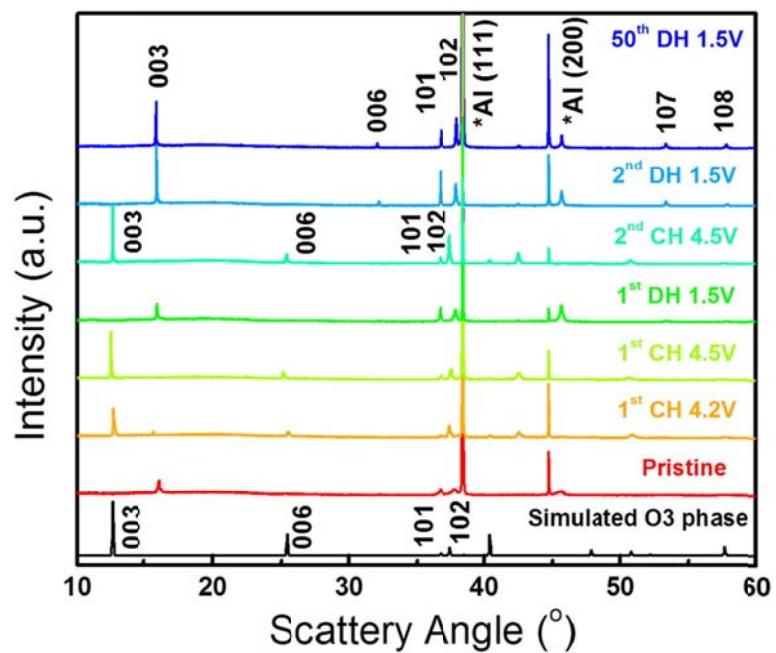
Figure 8.2 *Ex-situ* SXRD for NaLi$_{0.07}$Ni$_{0.26}$Mn$_{0.4}$Co$_{0.26}$O$_2$ at different states.
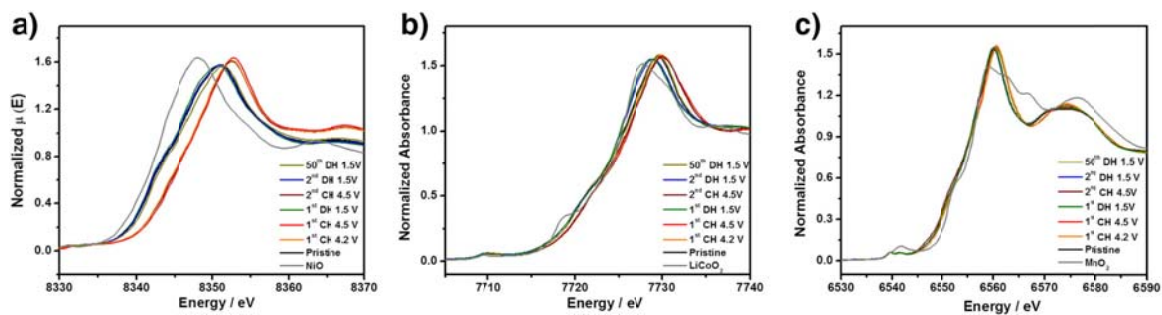
Figure 8.3 *Ex-situ* XAS analysis for $NaLi_{0.07}Ni_{0.26}Mn_{0.4}Co_{0.26}O_2$ at different states. XANES spectra for (a) Ni, (b) Co and (c) Mn K-edge respectively.

Chapter 9. Summary and future work

The focus of this research is to diagnose, optimize and design Ni and Mn based layered oxides as cathode materials for next generation Li-ion batteries and Na-ion batteries. The layered oxides system possesses great potential as high energy density cathodes, since their theoretical capacity has not been achieved yet. Replacing the Co in the layered oxides by Ni and Mn will even lower the cost of the cathodes. The *operando* neutron diffraction technique is chosen as an advanced characterization tool, which is very powerful to investigate the structural changes and Li dynamics of cathode materials during battery charge/discharge cycling. The surface modification is widely used in the material developments, however the role of surface modification is not well studied in the reported literatures. By combining different surface sensitive techniques, roles of each surface modification strategy on the enhanced performance are fully understood. Na-ion battery has similar working principles with Li-ion battery: the Na ions travels between cathode and anode during electrochemical cycling. Inspired by the working mechanism of Li-rich cathode material, a series of new layered oxide cathodes are explored for Na-ion batteries, which shows high capacity, high energy density, and high stability.

In the first part of this thesis, the work focus on developing *operando* neutron diffraction technique to study the dynamic structural changes in Li-excess layered oxides during its first cycle. Since neutron diffraction requires

large quantity of materials exposed to the beam. In addition, all the battery components contribute to the neutron diffraction patterns, which reduces the signal to noise ratio of the Li-rich cathode. In order to overcome these problems, a battery with special configuration for *operando* neutron study has to be designed.

The first experiment is based on a lab pouch cell, which contains only one layer $Li_{1.2}Ni_{0.18}Mn_{0.53}Co_{0.1}O_2$ cathode and graphite anode. This setup allows for the simultaneous observation of the anode material. Our observation shows a phase transformation in the anode at end of charge and start of discharge. The reversible change of structure and phase transformation shows good reversibility performance of the graphite anode. However, due to the low statistics from cathode, only the (102) peak from $Li_{1.2}Ni_{0.18}Mn_{0.53}Co_{0.1}O_2$ has been observed, which shows an irreversible expansion after the first cycle which is most likely caused by oxygen loss from the structure.

Later, a thick pouch cell with twelve layers was designed to increase the amount of cathode material in the scattering volume, which achieves better signal than the previous single layer cell. The strong scattering from graphite anode apparently lowers the contribution of the cathode signal to the neutron pattern. In addition, there are some peaks from the cathode overlapping with graphite peaks at < 1.3 Å d-spacing region. The graphite anode also undergoes a complicated phase transformation during charge/ discharge, which will introduce two more phases to the refinement. Those factors will reduce the reliability of

refined structure for cathode with increasing floating parameters, limiting refinement of atom occupancy and position.

The multi-layered pouch cell was redesigned by replacing the graphite anode with an amorphous silicon anode. For the Li-rich / Si cell, the evolution of (110), (108), (107), (104), (102), and (006) peaks from cathode can be clearly distinguished when compared to the LR / graphite cell. This o*perando* neutron diffraction on high Li-rich $Li[Li_{x/3}Ni_{(3/8-3x/8)}Co_{(1/4-x/4)}Mn_{(3/8+7x/24)}]O_2$ (x=0.6, HLR) and low Li-rich $Li[Li_{x/3}Ni_{(1/3-x/3)}Co_{(1/3-x/3)}Mn_{(1/3+x/3)}]O_2$ (x=0.24, LLR) cathode were performed during battery operation using a custom 1 Ah pouch battery with amorphous silicon to isolate structural changes for the cathode. Evolution of the lattice parameters and oxygen position revealed large lattice contractions occuring for the low Li-rich cathode and a largely delayed change in the high Li-rich cathode at higher voltages. Lithium dynamics were observed and quantified. It is revealed for the first time that lithium migration rates at different sites are highly dependent on the different voltage regions that exhibit different battery characteristics. First, the extraction of lithium at the slope region is largely dominated by migration within lithium layers. During the plateau region, lithium migration within lithium layers slows down and migration from the transition metal layer occurs. Upon discharge, lithium from the transition metal layer is largely irreversible with only lithium reinsertion occuring within lithium layers. These results provide new insights into the lithium migration behavior in lithium rich layered oxides and demonstrate the unique capabilities to observe light elements in the bulk under *operando* conditions via neutron diffraction.

Although the oxygen positions stay constant during plateau as a result of the anion evolution has been observed. More work will be done to quantify the oxygen vacancies in the bulk via *operando* neutron diffraction. Identification of the cation migration and oxygen vacancy evolution might explain the voltage degradation in this series of Li-rich layered compounds.

Although many surface modifications improved the electrochemical performance of Li-rich, the fundamental role in terms of their chemical and structural effects, are still not well understood. In this work, we prepared Li-excess layered oxide with composition of $Li_{1.2}Ni_{0.2}Mn_{0.6}O_2$ (LNMO) using a routine hydroxide co-precipitation method. A mild acid, NH_4F, and metal precipitant, Al^{3+}, were used together to modify the surface of Li-rich. First, the bulk crystal structures and morphologies of these materials were examined. Then, a series of surface sensitive characterizations were carried out to investigate the chemical and structural changes after surface co-modification. We reveal that the surface chemistry of cathode materials will significantly affect the uniformity and chemistry of coating layer. The surface co-modifications brought changes to the material's surface, from both a structural and chemical aspect. In order to identify these sophisticated changes, multi-modality surface sensitive tools was applied in an attempt to obtain a complete picture. The NH_4F promoted the transformation of a surface spinel-like phase, as well as the formation of isolated nanoislands of active material, which facilitated the activation of the cathode material, leading to higher discharge capacity. At the same time, amorphous Al_2O_3 surface coating reduced the side reaction between electrode and

electrolyte, and also irreversible oxygen loss, thus reducing the irreversible capacity. In particular, while the Mn^{3+} / Mn^{4+} redox pair still showed to increase indicating destabilization, the surface co-modification stabilized the Ni^{2+} / Ni^{4+} region in terms of capacity and voltage. These findings help us understand the working mechanisms of surface modifications which will shed lights on designing reasonable surface modifications for high voltage cathode materials in the future.

We developed nanoscale self-regulated Li_3PO_4-based surface amorphous films to Li-rich layered oxide $Li_{1.13}Ni_{0.3}Mn_{0.57}O_2$ via a facile method. The mixture of 2 wt.% Li_3PO_4 and $Li_{1.13}Ni_{0.3}Mn_{0.57}O_2$ annealed at 600 °C shows significantly improved coulombic efficiency in first cycle, rate capability, and cycling stability of Li-rich. These improvements are valid even at an elevated temperature. We expect that this scalable method will also work for other high voltage cathode materials for lithium ion batteries.

Since the high capacity of Li-excess layered oxide cathode is dominated by the oxygen behavior. The future research aims to develop advanced microscopy and spectroscopy tools to probe, understand, and optimize the anion redox and oxygen evolution that govern the performance limitations of Li-excess transition metal (Ni,Co,Mn, etc.) oxide cathode materials which offer more energy density than do classical layered materials. However, these materials suffer from: (1) voltage instabilities, (2) first cycle irreversible capacity due to oxygen evolution which lead to structural instability, and (3) interface chemical changes due to anion redox and oxygen evolution which make the cathode electrolyte interface unstable. One promising approach intends to investigate the anion

activities in single particle Li-excess cathode materials using *operando* Bragg Coherent Diffraction Imaging (BCDI), scanning transmission electron microscopy (STEM) imaging, electron energy loss spectroscopy (EELS), and by quantum mechanics based simulation code Wien2K to decipher the complexity of anion activities during electrochemical cycling. To validate the single particle diagnosis data, the data should be complemented through the use of a series of well-developed characterization techniques such as ex-situ X-ray photoelectron spectroscopy (XPS), ex-situ soft X-ray absorption spectroscopy (XAS), and in-situ Differential electrochemical mass spectroscopy (DEMS) which will give a more comprehensive understanding of the materials. This unique and powerful suite of characterization tools for the bulk and surface of the electrode materials will be utilized to specify the causes for instabilities at the surfaces (1-2nm) and sub-surfaces (5-10nm) of the materials exposed to high voltages and could be extended to anode materials. Therefore, the proposed diagnostic tools will ultimately lead to careful manipulation of the anion activities (anion redox and oxygen evolution) in this class of materials to optimize and stabilize the voltage operation, structure, and chemical interface.

The relatively low capacity and limited cycling retention are presumably due to the fact that most of these materials undergo multiple phase transformations. These transformations could be one of the major problems that limit the practical uses of Na-ion batteries since it deteriorates the cycle life and rate capabilities. Herein, to overcome this issue, a new O3 compound is prepared through Li-Na ion exchange, inspired by the idea in Li-ion batteries that

Li-rich O3 compound has been demonstrated single slope voltage profile with significant improvement in capacity and cycling retention for Li layered electrodes. A new O3 - $Na_{0.78}Li_{0.18}Ni_{0.25}Mn_{0.583}O_w$ is obtained by the electrochemical Na-Li ion exchange process of $Li_{1.167}Ni_{0.25}Mn_{0.583}O_2$. The new material shows exceptionally high discharge capacity of 240 mAh g^{-1} in the voltage range of 1.5-4.5 V, thus the total energy density at the materials level reaches 675 Wh kg^{-1}. It is the highest capacity as well as highest energy density so far among all the reported cathodes in Na-ion batteries. The O3 phase is kept through ion-exchange and cycling process, as confirmed by SXRD. The stabilized O3 phase could be related to the tetrahedral Li formed upon initial lithiation, and breaks through the critical limitation for most of the O3 compounds. XAS results show that Ni^{2+}/Ni^{4+} is the main active redox couple during cycling while Mn ions basically stay at tetravalent state. The Na full cell utilizing $Na_{0.78}Li_{0.18}Ni_{0.25}Mn_{0.583}O_w$ as cathode delivers 430 Wh kg^{-1} energy density, shedding light on the future of the Na-ion technologies.

As a following up work, a new Li substituted Na layered oxide with pure O3 phase, $NaLi_{0.07}Ni_{0.26}Mn_{0.4}Co_{0.26}O_2$, is successfully achieved, demonstrating a considerably high reversible capacity of 147 mAh g^{-1} and excellent rate performance. The phase is stabilized throughout the cycling, which could be the main reason for its good electrochemical properties. Ni^{2+} / Ni^{4+} is the main active redox couple during cycling, and Co^{3+} / Co^{4+} partially contributes to the charge compensation.

The Li substituted O3 layered oxides for Na-ion batteries are first introduced in this work. It shows great potential for high energy density, low cost large scale stationary energy storage systems. For the future study, the composition and synthesis process should be optimized. More important, the working mechanism of these series of materials should be revealed for guiding the better design of the high energy density materials in the future.

References

1. J. B. Goodenough and K. S. Park, *J Am Chem Soc*, 2013, **135**, 1167-1176.

2. A. Manthiram, *J Phys Chem Lett*, 2011, **2**, 176-184.

3. B. Xu, D. Qian, Z. Wang and Y. S. Meng, *Materials Science and Engineering: R: Reports*, 2012.

4. M. D. Slater, D. Kim, E. Lee and C. S. Johnson, *Adv Funct Mater*, 2013, **23**, 947-958.

5. N. Sharma, W. K. Pang, Z. P. Guo and V. K. Peterson, *Chemsuschem*, 2015, **8**, 2826-2853.

6. M. S. Whittingham, R. F. Savinell and T. Zawodzinski, *Chemical Reviews*, 2004, **104**, 4243-4244.

7. M. S. Whittingham, *Chemical Reviews*, 2014, **114**, 11414-11443.

8. M. S. Whittingham, *Chemical Reviews*, 2004, **104**, 4271-4301.

9. P. Arora and Z. M. Zhang, *Chemical Reviews*, 2004, **104**, 4419-4462.

10. V. Etacheri, R. Marom, R. Elazari, G. Salitra and D. Aurbach, *Energ Environ Sci*, 2011, **4**, 3243-3262.

11. K. Xu, *Chemical Reviews*, 2014, **114**, 11503-11618.

12. B. Nykvist and M. Nilsson, *Nature Climate Change*, 2015, **5**, 329-332.

13. DOE Annual Merit Review 2015, http://www.annualmeritreview.energy.gov/.

14. T. Ohzuku, M. Nagayama, K. Tsuji and K. Ariyoshi, *Journal of Materials Chemistry*, 2011, **21**, 10179.

15. M. H. Rossouw and M. M. Thackeray, *Materials Research Bulletin*, 1991, **26**, 463-473.

16. K. Naoi, D. Yonekura, S. Moriyama, H. Goto, E. Iwama, S. Kubota, S. Ishimoto and W. Naoi, *Journal of Alloys and Compounds*, 2014, **605**, 137-141.

17. S. Hy, H. Liu, M. Zhang, D. Qian, B.-J. Hwang and Y. S. Meng, *Energ Environ Sci*, 2016, **9**, 1931-1954.

18. L. Ghadbeigi, J. K. Harada, B. R. Lettiere and T. D. Sparks, *Energy Environ. Sci.*, 2015, **8**, 1640-1650.

19. M. Kunduraci and G. G. Amatucci, *Electrochimica Acta*, 2008, **53**, 4193-4199.

20. X. Yan, G. Yang, J. Liu, Y. Ge, H. Xie, X. Pan and R. Wang, *Electrochimica Acta*, 2009, **54**, 5770-5774.

21. S. Meng, G. Ceder, C. P. Grey, W.-S. Yoon, M. Jiang, J. Bre ́ger and Y. Shao-Horn, *Chem Mater*, 2005.

22. Z. Lu, D. D. MacNeil and J. R. Dahn, *Electrochemical and Solid-State Letters*, 2001, **4**, A191.

23. M. M. Thackeray, C. S. Johnson, J. T. Vaughey, N. Li and S. A. Hackney, *Journal of Materials Chemistry*, 2005, **15**, 2257.

24. M. M. Thackeray, S.-H. Kang, C. S. Johnson, J. T. Vaughey, R. Benedek and S. A. Hackney, *Journal of Materials Chemistry*, 2007, **17**, 3112.

25. C. H. Lei, J. Bareño, J. G. Wen, I. Petrov, S. H. Kang and D. P. Abraham, *Journal of Power Sources*, 2008, **178**, 422-433.

26. J. Bareño, M. Balasubramanian, S. H. Kang, J. G. Wen, C. H. Lei, S. V. Pol, I. Petrov and D. P. Abraham, *Chem Mater*, 2011, **23**, 2039-2050.

27. J. Bareno, C. H. Lei, J. G. Wen, S. H. Kang, I. Petrov and D. P. Abraham, *Advanced Materials*, 2010, **22**, 1122-1127.

28. K. A. Jarvis, Z. Deng, L. F. Allard, A. Manthiram and P. J. Ferreira, *Chem Mater*, 2011, **23**, 3614-3621.

29. Z. Lu, L. Y. Beaulieu, R. A. Donaberger, C. L. Thomas and J. R. Dahn, *Journal of the Electrochemical Society*, 2002, **149**, A778.

30. H. Yu, R. Ishikawa, Y. G. So, N. Shibata, T. Kudo, H. Zhou and Y. Ikuhara, *Angewandte Chemie*, 2013, **52**, 5969-5973.

31. A. Devaraj, M. Gu, R. Colby, P. Yan, C. M. Wang, J. M. Zheng, J. Xiao, A. Genc, J. G. Zhang, I. Belharouak, D. Wang, K. Amine and S. Thevuthasan, *Nature Communications*, 2015, **6**, 8014.

32. A. K. Shukla, Q. M. Ramasse, C. Ophus, H. Duncan, F. Hage and G. Chen, *Nature Communications*, 2015, **6**, 8711.

33. E. McCalla, C. M. Lowartz, C. R. Brown and J. R. Dahn, *Chem Mater*, 2013, **25**, 912-918.

34. E. McCalla, A. W. Rowe, J. Camardese and J. R. Dahn, *Chem Mater*, 2013, **25**, 2716-2721.

35. E. McCalla, A. W. Rowe, R. Shunmugasundaram and J. R. Dahn, *Chem Mater*, 2013, **25**, 989-999.

36. J. Zheng, M. Gu, A. Genc, J. Xiao, P. Xu, X. Chen, Z. Zhu, W. Zhao, L. Pullan, C. Wang and J. G. Zhang, *Nano letters*, 2014, **14**, 2628-2635.

37. M. Gu, I. Belharouak, A. Genc, Z. Wang, D. Wang, K. Amine, F. Gao, G. Zhou, S. Thevuthasan, D. R. Baer, J. G. Zhang, N. D. Browning, J. Liu and C. Wang, *Nano letters*, 2012, **12**, 5186-5191.

38. C. R. Brown, E. McCalla, C. Watson and J. R. Dahn, *ACS combinatorial science*, 2015, **17**, 381-391.

39. R. Shunmugasundaram, R. Senthil Arumugam and J. R. Dahn, *Chem Mater*, 2015, **27**, 757-767.

40. M. Gu, A. Genc, I. Belharouak, D. Wang, K. Amine, S. Thevuthasan, D. R. Baer, J.-G. Zhang, N. D. Browning, J. Liu and C. Wang, *Chem Mater*, 2013, **25**, 2319-2326.

41. A. R. Armstrong, M. Holzapfel, P. Novak, C. S. Johnson, S. H. Kang, M. M. Thackeray and P. G. Bruce, *Journal of the American Chemical Society*, 2006, **128**, 8694-8698.

42. S. Hy, F. Felix, J. Rick, W. N. Su and B. J. Hwang, *Journal of the American Chemical Society*, 2014, **136**, 999-1007.

43. H. D. Liu, C. R. Fell, K. An, L. Cai and Y. S. Meng, *Journal of Power Sources*, 2013, **240**, 772-778.

44. N. Yabuuchi, K. Yoshii, S. T. Myung, I. Nakai and S. Komaba, *Journal of the American Chemical Society*, 2011, **133**, 4404-4419.

45. H. Koga, L. Croguennec, M. Menetrier, P. Mannessiez, F. Weill and C. Delmas, *Journal of Power Sources*, 2013, **236**, 250-258.

46. J. M. Zheng, Z. R. Zhang, X. B. Wu, Z. X. Dong, Z. Zhu and Y. Yang, *Journal of the Electrochemical Society*, 2008, **155**, A775.

47. B. Xu, C. R. Fell, M. Chi and Y. S. Meng, *Energ Environ Sci*, 2011, **4**, 2223.

48. D. Qian, B. Xu, M. Chi and Y. S. Meng, *Physical chemistry chemical physics : PCCP*, 2014, **16**, 14665-14668.

49. J. R. Croy, D. Kim, M. Balasubramanian, K. Gallagher, S. H. Kang and M. M. Thackeray, *Journal of the Electrochemical Society*, 2012, **159**, A781.

50. K. A. Jarvis, Z. Deng, L. F. Allard, A. Manthiram and P. J. Ferreira, *Journal of Materials Chemistry*, 2012, **22**, 11550-11555.

51. F. Dogan, B. R. Long, J. R. Croy, K. G. Gallagher, H. Iddir, J. T. Russell, M. Balasubramanian and B. Key, *Journal of the American Chemical Society*, 2015, **137**, 2328-2335.

52. Z. Lu and J. R. Dahn, *Journal of the Electrochemical Society*, 2002, **149**, A815.

53. M. Sathiya, G. Rousse, K. Ramesha, C. P. Laisa, H. Vezin, M. T. Sougrati, M. L. Doublet, D. Foix, D. Gonbeau, W. Walker, A. S. Prakash, M. Ben Hassine, L. Dupont and J. M. Tarascon, *Nature materials*, 2013, **12**, 827-835.

54. M. Sathiya, J. B. Leriche, E. Salager, D. Gourier, J. M. Tarascon and H. Vezin, *Nat Commun*, 2015, **6**, 6276.

55. J. Hong, H.-D. Lim, M. Lee, S.-W. Kim, H. Kim, S.-T. Oh, G.-C. Chung and K. Kang, *Chem Mater*, 2012, **24**, 2692-2697.

56. A. Boulineau, L. Simonin, J. F. Colin, E. Canevet, L. Daniel and S. Patoux, *Chem Mater*, 2012, **24**, 3558-3566.

57. M. Oishi, T. Fujimoto, Y. Takanashi, Y. Orikasa, A. Kawamura, T. Ina, H. Yamashige, D. Takamatsu, K. Sato, H. Murayama, H. Tanida, H. Arai, H. Ishii, C. Yogi, I. Watanabe, T. Ohta, A. Mineshige, Y. Uchimoto and Z. Ogumi, *Journal of Power Sources*, 2013, **222**, 45-51.

58. K. J. Carroll, D. Qian, C. Fell, S. Calvin, G. M. Veith, M. Chi, L. Baggetto and Y. S. Meng, *Physical chemistry chemical physics : PCCP*, 2013, **15**, 11128-11138.

59. S. Hy, W.-N. Su, J.-M. Chen and B.-J. Hwang, *The Journal of Physical Chemistry C*, 2012, **116**, 25242-25247.

60. P. Yan, A. Nie, J. Zheng, Y. Zhou, D. Lu, X. Zhang, R. Xu, I. Belharouak, X. Zu, J. Xiao, K. Amine, J. Liu, F. Gao, R. Shahbazian-Yassar, J. G. Zhang and C. M. Wang, *Nano letters*, 2015, **15**, 514-522.

61. M. Gu, I. Belharouak, J. M. Zheng, H. M. Wu, J. Xiao, A. Genc, K. Amine, S. Thevuthasan, D. R. Baer, J. G. Zhang, N. D. Browning, J. Liu and C. M. Wang, *Acs Nano*, 2013, **7**, 760-767.

62. J. Zheng, M. Gu, J. Xiao, P. Zuo, C. Wang and J. G. Zhang, *Nano letters*, 2013, **13**, 3824-3830.

63. P. J. Phillips, J. Bareño, Y. Li, D. P. Abraham and R. F. Klie, *Adv Energy Mater*, 2015, n/a-n/a.

64. A. Boulineau, L. Simonin, J. F. Colin, C. Bourbon and S. Patoux, *Nano letters*, 2013, **13**, 3857-3863.

65. C. R. Fell, K. J. Carroll, M. Chi and Y. S. Meng, *Journal of the Electrochemical Society*, 2010, **157**, A1202.

66. M. G. Verde, H. D. Liu, K. J. Carroll, L. Baggetto, G. M. Veith and Y. S. Meng, *ACS applied materials & interfaces*, 2014, **6**, 18868-18877.

67. H. Liu, D. Qian, M. G. Verde, M. Zhang, L. Baggetto, K. An, Y. Chen, K. J. Carroll, D. Lau, M. Chi, G. M. Veith and Y. S. Meng, *ACS applied materials & interfaces*, 2015, **7**, 19189-19200.

68. M. Gu, I. Belharouak, J. Zheng, H. Wu, J. Xiao, A. Genc, K. Amine, S. Thevuthasan, D. R. Baer, J. G. Zhang, N. D. Browning, J. Liu and C. Wang, *Acs Nano*, 2013, **7**, 760-767.

69. J. R. Croy, M. Balasubramanian, K. G. Gallagher and A. K. Burrell, *Accounts of chemical research*, 2015.

70. S. Hy, J.-H. Cheng, J.-Y. Liu, C.-J. Pan, J. Rick, J.-F. Lee, J.-M. Chen and B. J. Hwang, *Chem Mater*, 2014, **26**, 6919-6927.

71. M. Sathiya, A. M. Abakumov, D. Foix, G. Rousse, K. Ramesha, M. Saubanere, M. L. Doublet, H. Vezin, C. P. Laisa, A. S. Prakash, D. Gonbeau, G. VanTendeloo and J. M. Tarascon, *Nature materials*, 2015, **14**, 230-238.

72. M. Bettge, Y. Li, K. Gallagher, Y. Zhu, Q. Wu, W. Lu, I. Bloom and D. P. Abraham, *Journal of the Electrochemical Society*, 2013, **160**, A2046-A2055.

73. J. R. Croy, K. G. Gallagher, M. Balasubramanian, Z. Chen, Y. Ren, D. Kim, S.-H. Kang, D. W. Dees and M. M. Thackeray, *The Journal of Physical Chemistry C*, 2013, **117**, 6525-6536.

74. K. G. Gallagher, J. R. Croy, M. Balasubramanian, M. Bettge, D. P. Abraham, A. K. Burrell and M. M. Thackeray, *Electrochemistry Communications*, 2013, **33**, 96-98.

75. D. Kim, J. R. Croy and M. M. Thackeray, *Electrochemistry Communications*, 2013, **36**, 103-106.

76. M. Jiang, B. Key, Y. S. Meng and C. P. Grey, *Chem Mater*, 2009, **21**, 2733-2745.

77. D. Mohanty, J. L. Li, D. P. Abraham, A. Huq, E. A. Payzant, D. L. Wood and C. Daniel, *Chem Mater*, 2014, **26**, 6272-6280.

78. D. Mohanty, J. Li, D. P. Abraham, A. Huq, E. A. Payzant, D. L. Wood and C. Daniel, *Chem Mater*, 2014, **26**, 6272-6280.

79. C. Genevois, H. Koga, L. Croguennec, M. Ménétrier, C. Delmas and F. Weill, *The Journal of Physical Chemistry C*, 2015, **119**, 75-83.

80. Z. G. Yang, J. L. Zhang, M. C. W. Kintner-Meyer, X. C. Lu, D. W. Choi, J. P. Lemmon and J. Liu, *Chemical Reviews*, 2011, **111**, 3577-3613.

81. M. S. Whittingham, *Prog Solid State Ch*, 1978, **12**, 41-99.

82. C. Delmas, J. J. Braconnier, C. Fouassier and P. Hagenmuller, *Solid State Ionics*, 1981, **3-4**, 165-169.

83. J. M. Tarascon, *Solid State Ionics*, 1986, **18-9**, 768-772.

84. C. Delmas, C. Fouassier and P. Hagenmuller, *Physica B & C*, 1980, **99**, 81-85.

85. Z. H. Lu and J. R. Dahn, *Journal of The Electrochemical Society*, 2001, **148**, A1225-A1229.

86. Z. H. Lu and J. R. Dahn, *Journal of The Electrochemical Society*, 2001, **148**, A710-A715.

87. D. Kim, S. H. Kang, M. Slater, S. Rood, J. T. Vaughey, N. Karan, M. Balasubramanian and C. S. Johnson, *Adv Energy Mater*, 2011, **1**, 333-336.

88. A. Caballero, L. Hernan, J. Morales, L. Sanchez, J. S. Pena and M. A. G. Aranda, *Journal of Materials Chemistry*, 2002, **12**, 1142-1147.

89. N. Yabuuchi, M. Kajiyama, J. Iwatate, H. Nishikawa, S. Hitomi, R. Okuyama, R. Usui, Y. Yamada and S. Komaba, *Nature materials*, 2012, **11**, 512-517.

90.   S. Komaba, C. Takei, T. Nakayama, A. Ogata and N. Yabuuchi, *Electrochemistry Communications*, 2010, **12**, 355-358.

91.   C. Didier, M. Guignard, C. Denage, O. Szajwaj, S. Ito, I. Saadoune, J. Darriet and C. Delmas, *Electrochem Solid St*, 2011, **14**, A75-A78.

92.   S. Komaba, W. Murata, T. Ishikawa, N. Yabuuchi, T. Ozeki, T. Nakayama, A. Ogata, K. Gotoh and K. Fujiwara, *Adv Funct Mater*, 2011, **21**, 3859-3867.

93.   M. Sathiya, K. Hemalatha, K. Ramesha, J. M. Tarascon and A. S. Prakash, *Chem Mater*, 2012, **24**, 1846-1853.

94.   T. Ohzuku and Y. Makimura, *Chem Lett*, 2001, 642-643.

95.   N. Yabuuchi and T. Ohzuku, *Journal of Power Sources*, 2003, **119**, 171-174.

96.   S. C. Yin, Y. H. Rho, I. Swainson and L. F. Nazar, *Chem Mater*, 2006, **18**, 1901-1910.

97.   W. S. Yoon, S. Iannopollo, C. P. Grey, D. Carlier, J. Gorman, J. Reed and G. Ceder, *Electrochem Solid St*, 2004, **7**, A167-A171.

98.   P. Strobel and B. Lambertandron, *J Solid State Chem*, 1988, **75**, 90-98.

99.   C. S. Johnson, J. S. Kim, C. Lefief, N. Li, J. T. Vaughey and M. M. Thackeray, *Electrochemistry Communications*, 2004, **6**, 1085-1091.

100.   A. R. Armstrong, M. Holzapfel, P. Novak, C. S. Johnson, S. H. Kang, M. M. Thackeray and P. G. Bruce, *J Am Chem Soc*, 2006, **128**, 8694-8698.

101.   A. D. Robertson and P. G. Bruce, *Electrochemical and Solid-State Letters*, 2004, **7**, A294.

102.   C. R. Fell, M. Chi, Y. S. Meng and J. L. Jones, *Solid State Ionics*, 2012, **207**, 44-49.

103.   A. Ito, Y. Sato, T. Sanada, M. Hatano, H. Horie and Y. Ohsawa, *Journal of Power Sources*, 2011, **196**, 6828-6834.

104.   N. Sharma and V. K. Peterson, *Journal of Solid State Electrochemistry*, 2011, **16**, 1849-1856.

105.   N. Sharma, V. K. Peterson, M. M. Elcombe, M. Avdeev, A. J. Studer, N. Blagojevic, R. Yusoff and N. Kamarulzaman, *Journal of Power Sources*, 2010, **195**, 8258-8266.

106.   H. Berg, H. Rundlov and J. O. Thomas, *Solid State Ionics*, 2001, **144**, 65-69.

107.   L. Cai, K. An, Z. Feng, C. Liang and S. J. Harris, *Journal of Power Sources*, 2013, **236**, 163-168.

108.   J. F. Colin, V. Godbole and P. Novak, *Electrochemistry Communications*, 2010, **12**, 804-807.

109.   X. L. Wang, K. An, L. Cai, Z. L. Feng, S. E. Nagler, C. Daniel, K. J. Rhodes, A. D. Stoica, H. D. Skorpenske, C. D. Liang, W. Zhang, J. Kim, Y. Qi and S. J. Harris, *Scientific reports*, 2012, **2**.

110.   K. An, H. D. Skorpenske, A. D. Stoica, D. Ma, X. L. Wang and E. Cakmak, *Metall Mater Trans A*, 2011, **42A**, 95-99.

111.   K. An, X. L. Wang and A. D. Stoica, 2012.

112.   A. C. Larson and R. B. V. Dreele, *Los Alamos National Laboratory Report (LAUR)*, 2004, **86-748**.

113.   V. O. Garlea, B. C. Chakoumakos, S. A. Moore, G. B. Taylor, T. Chae, R. G. Maples, R. A. Riedel, G. W. Lynn and D. L. Selby, *Appl Phys a-Mater*, 2010, **99**, 531-535.

114.   B. H. Toby, *J Appl Crystallogr*, 2001, **34**, 210-213.

115.   W. Senaratne, K. Takada, R. Das, J. Cohen, B. Baird, H. D. Abruna and C. K. Ober, *Biosensors & bioelectronics*, 2006, **22**, 63-70.

116.   J.-M. Kim and H.-T. Chung, *Electrochimica Acta*, 2004, **49**, 937-944.

117.   M. A. Rodriguez, D. Ingersoll, S. C. Vogel and D. J. Williams, *Electrochem Solid St*, 2004, **7**, A8-A10.

118.   M. Winter, J. O. Besenhard, M. E. Spahr and P. Novak, *Advanced Materials*, 1998, **10**, 725-763.

119.   D. Guerard and A. Herold, *Carbon*, 1975, **13**, 337-345.

120.   Y. S. Meng, G. Ceder, C. P. Grey, W. S. Yoon and Y. Shao-Horn, *Electrochemical and Solid-State Letters*, 2004, **7**, A155.

121.   A. R. Armstrong, M. Holzapfel, P. Novak, C. S. Johnson, S. H. Kang, M. M. Thackeray and P. G. Bruce, *J Am Chem Soc*, 2006, **128**, 8694-8698.

122. C. R. Fell, D. N. Qian, K. J. Carroll, M. F. Chi, J. L. Jones and Y. S. Meng, *Chem Mater*, 2013, **25**, 1621-1629.

123. J. B. Goodenough and K.-S. Park, *Journal of the American Chemical Society*, 2013, **135**, 1167-1176.

124. D. Andre, S.-J. Kim, P. Lamp, S. F. Lux, F. Maglia, O. Paschos and B. Stiaszny, *Journal of Materials Chemistry A*, 2015, **3**, 6709-6732.

125. M. S. Whittingham, *Chemical Reviews*, 2014.

126. J. J. Huang and J. Luo, *Physical chemistry chemical physics : PCCP*, 2014, **16**, 7786-7798.

127. H. Koga, L. Croguennec, M. Ménétrier, K. Douhil, S. Belin, L. Bourgeois, E. Suard, F. Weill and C. Delmas, *Journal of the Electrochemical Society*, 2013, **160**, A786-A792.

128. H. Koga, L. Croguennec, M. Ménétrier, P. Mannessiez, F. Weill and C. Delmas, *Journal of Power Sources*, 2013, **236**, 250-258.

129. F. Rosciano, M. Holzapfel, W. Scheifele and P. Novak, *J Appl Crystallogr*, 2008, **41**, 690-694.

130. J. J. Biendicho, M. Roberts, C. Offer, D. Noreus, E. Widenkvist, R. I. Smith, G. Svensson, K. Edstrom, S. T. Norberg, S. G. Eriksson and S. Hull, *Journal of Power Sources*, 2014, **248**, 900-904.

131. W. K. Pang, V. K. Peterson, N. Sharma, J. J. Shiu and S. H. Wu, *Chem Mater*, 2014, **26**, 2318-2326.

132. B. Vadlamani, K. An, M. Jagannathan and K. S. R. Chandran, *Journal of The Electrochemical Society*, 2014, **161**, A1731-A1741.

133. US 8741485 B2, 2014.

134. US 8394534 B2, 2013.

135. US 8389160 B2, 2013.

136. J. Xu, H. Liu and Y. S. Meng, *Electrochemistry Communications*, 2015, **60**, 13-16.

137. G. Kresse and D. Joubert, *Phys Rev B*, 1999, **59**, 1758-1775.

138. G. Kresse and J. Hafner, *Phys Rev B*, 1994, **49**, 14251-14269.

139.   G. Kresse and J. Furthmuller, *Phys Rev B,* 1996, **54**, 11169-11186.

140.   J. P. Perdew, K. Burke and Y. Wang, *Phys Rev B*, 1996, **54**, 16533-16539.

141.   P. H. Gamlen and J. W. White, *J Chem Soc Farad T 2*, 1976, **72**, 446-455.

142.   A. Bourbia, M. Draissia, H. Bedboudi, S. Boulkhessaim and M. Y. Debili, *J X-Ray Sci Technol*, 2010, **18**, 201-219.

143.   I. K. Suh, H. Ohta and Y. Waseda, *J Mater Sci*, 1988, **23**, 757-760.

144.   Z. H. Lu and J. R. Dahn, *Journal of The Electrochemical Society*, 2002, **149**, A815-A822.

145.   S. Hy, F. Felix, J. Rick, W. N. Su and B. J. Hwang, *J Am Chem Soc*, 2014, **136**, 999-1007.

146.   H. D. Liu, J. Xu, C. Z. Ma and Y. S. Meng, *Chemical communications*, 2015, **51**, 4693-4696.

147.   L. Simonin, J. F. Colin, V. Ranieri, E. Canevet, J. F. Martin, C. Bourbon, C. Baehtz, P. Strobel, L. Daniel and S. Patoux, *Journal of Materials Chemistry*, 2012, **22**, 11316-11322.

148.   I. E. Roberts, *Physica Scripta*, 2015, **90**, 094012.

149.   D. N. Qian, B. Xu, M. F. Chi and Y. S. Meng, *Physical chemistry chemical physics : PCCP*, 2014, **16**, 14665-14668.

150.   M. M. Thackeray, S. H. Kang, C. S. Johnson, J. T. Vaughey, R. Benedek and S. A. Hackney, *Journal of Materials Chemistry*, 2007, **17**, 3112-3125.

151.   F. Lin, I. M. Markus, D. Nordlund, T.-C. Weng, M. D. Asta, H. L. Xin and M. M. Doeff, *Nat Commun*, 2014, **5**.

152.   H. J. Yu and H. S. Zhou, *J Phys Chem Lett*, 2013, **4**, 1268-1280.

153.   Y. Wu and A. Manthiram, *Solid State Ionics*, 2009, **180**, 50-56.

154.   J. M. Zheng, J. Li, Z. R. Zhang, X. J. Guo and Y. Yang, *Solid State Ionics*, 2008, **179**, 1794-1799.

155.   J. Liu, Q. Wang, B. Reeja-Jayan and A. Manthiram, *Electrochemistry Communications*, 2010, **12**, 750-753.

156.   J. Liu, B. Reeja-Jayan and A. Manthiram, *J Phys Chem C*, 2010, **114**, 9528-9533.

157. S. K. Martha, J. Nanda, Y. Kim, R. R. Unocic, S. Pannala and N. J. Dudney, *Journal of Materials Chemistry A*, 2013, **1**, 5587-5595.

158. Q. Fu, F. Du, X. Bian, Y. Wang, X. Yan, Y. Zhang, K. Zhu, G. Chen, C. Wang and Y. Wei, *Journal of Materials Chemistry A*, 2014, **2**, 7555-7562.

159. S.-H. Kang and M. M. Thackeray, *Electrochemistry Communications*, 2009, **11**, 748-751.

160. J. C. Li, L. Baggetto, S. K. Martha, G. M. Veith, J. Nanda, C. D. Liang and N. J. Dudney, *Adv Energy Mater*, 2013, **3**, 1275-1278.

161. I. T. Kim, J. C. Knight, H. Celio and A. Manthiram, *Journal of Materials Chemistry A*, 2014.

162. S. H. Kang and M. M. Thackeray, *Journal of The Electrochemical Society*, 2008, **155**, A269-A275.

163. S. J. Pennycook, *Ultramicroscopy*, 1989, **30**, 58-69.

164. E. M. James and N. D. Browning, *Ultramicroscopy*, 1999, **78**, 125-139.

165. Z. L. Wang, J. S. Yin and Y. D. Jiang, *Micron*, 2000, **31**, 571-580.

166. L. Cai, Z. C. Liu, K. An and C. D. Liang, *Journal of The Electrochemical Society*, 2012, **159**, A924-A928.

167. Y. S. Meng, G. Ceder, C. P. Grey, W. S. Yoon, M. Jiang, J. Breger and Y. Shao-Horn, *Chem Mater*, 2005, **17**, 2386-2394.

168. J. Breger, M. Jiang, N. Dupre, Y. S. Meng, Y. Shao-Horn, G. Ceder and C. P. Grey, *J Solid State Chem*, 2005, **178**, 2575-2585.

169. K. J. Carroll, D. Qian, C. Fell, S. Calvin, G. M. Veith, M. F. Chi, L. Baggetto and Y. S. Meng, *Physical chemistry chemical physics : PCCP*, 2013, **15**, 11128-11138.

170. N. Yabuuchi, K. Yoshii, S. T. Myung, I. Nakai and S. Komaba, *J Am Chem Soc*, 2011, **133**, 4404-4419.

171. H. Kurata and C. Colliex, *Phys Rev B*, 1993, **48**, 2102-2108.

172. T. Riedl, T. Gemming and K. Wetzig, *Ultramicroscopy*, 2006, **106**, 284-291.

173. L. Baggetto, N. J. Dudney and G. M. Veith, *Electrochimica Acta*, 2013, **90**, 135-147.

174. S. A. C. Carabineiro, S. S. T. Bastos, J. J. M. Orfao, M. F. R. Pereira, J. J. Delgado and J. L. Figueiredo, *Catal Lett*, 2010, **134**, 217-227.

175. K. M. Shaju, G. V. S. Rao and B. V. R. Chowdari, *Electrochimica Acta*, 2003, **48**, 1505-1514.

176. G. C. Allen, S. J. Harris, J. A. Jutson and J. M. Dyke, *Appl Surf Sci*, 1989, **37**, 111-134.

177. Y. K. Sun, M. J. Lee, C. S. Yoon, J. Hassoun, K. Amine and B. Scrosati, *Advanced Materials*, 2012, **24**, 1192-1196.

178. K. J. Rosina, M. Jiang, D. Zeng, E. Salager, A. S. Best and C. P. Grey, *Journal of Materials Chemistry*, 2012, **22**, 20602.

179. H. Koga, L. Croguennec, M. Menetrier, P. Mannessiez, F. Weill, C. Delmas and S. Belin, *J Phys Chem C*, 2014, **118**, 5700-5709.

180. J. R. Croy, D. Kim, M. Balasubramanian, K. Gallagher, S. H. Kang and M. M. Thackeray, *Journal of The Electrochemical Society*, 2012, **159**, A781-A790.

181. H. Liu, Y. Chen, S. Hy, K. An, S. Venkatachalam, D. Qian, M. Zhang and Y. S. Meng, *Advanced Energy Materials*, 2016, n/a-n/a.

182. S. Hy, Felix, Y. H. Chen, J. Y. Liu, J. Rick and B. J. Hwang, *J Power Sources*, 2014, **256**, 324-328.

183. X. F. Bian, Q. Fu, X. F. Bie, P. L. Yang, H. L. Qiu, Q. Pang, G. Chen, F. Du and Y. J. Wei, *Electrochim Acta*, 2015, **174**, 875-884.

184. J. Zheng, M. Gu, J. Xiao, B. J. Polzin, P. Yan, X. Chen, C. Wang and J.-G. Zhang, *Chem Mater*, 2014, **26**, 6320-6327.

185. H. Konishi, K. Suzuki, S. Taminato, K. Kim, Y. M. Zheng, S. Kim, J. Lim, M. Hirayama, J. Y. Son, Y. T. Cui and R. Kanno, *J Power Sources*, 2014, **269**, 293-298.

186. J. M. Zheng, P. H. Xu, M. Gu, J. Xiao, N. D. Browning, P. F. Yan, C. M. Wang and J. G. Zhang, *Chem Mater*, 2015, **27**, 1381-1390.

187. J. M. Tarascon, *Philos. Trans. R. Soc. A-Math. Phys. Eng. Sci.*, 2010, **368**, 3227-3241.

188. S. P. Ong, V. L. Chevrier, G. Hautier, A. Jain, C. Moore, S. Kim, X. H. Ma and G. Ceder, *Energ Environ Sci*, 2011, **4**, 3680-3688.

189.   B. L. Ellis and L. F. Nazar, *Curr Opin Solid St M*, 2012, **16**, 168-177.

190.   H. L. Pan, Y. S. Hu and L. Q. Chen, *Energ Environ Sci*, 2013, **6**, 2338-2360.

191.   V. Palomares, M. Casas-Cabanas, E. Castillo-Martinez, M. H. Han and T. Rojo, *Energ Environ Sci*, 2013, **6**, 2312-2337.

192.   M. Valvo, F. Lindgren, U. Lafont, F. Bjorefors and K. Edstrom, *Journal of Power Sources*, 2014, **245**, 967-978.

193.   J. Xu, D. H. Lee and Y. S. Meng, *Funct Mater Lett*, 2013, **6**.

194.   M. R. Palacin, *Chemical Society Reviews*, 2009, **38**, 2565-2575.

195.   C. Fouassier, C. Delmas and P. Hagenmuller, *Materials Research Bulletin*, 1975, **10**, 443–449.

196.   J. Xu, D. H. Lee and Y. S. Meng, *Functional materials letters*, 2013, **6**, 1330001.

197.   R. Berthelot, D. Carlier and C. Delmas, *Nature materials*, 2011, **10**, 74-U73.

198.   D. H. Lee, J. Xu and Y. S. Meng, *Physical chemistry chemical physics : PCCP*, 2013, **15**, 3304-3312.

199.   H. Yoshida, N. Yabuuchi, K. Kubota, I. Ikeuchi, A. Garsuch, M. Schulz-Dobrick and S. Komaba, *Chemical communications*, 2014, **50**, 3677-3680.

200.   Z. Jie, X. Jing, L. Dae Hoe, N. Dimov, Y. S. Meng and S. Okada, *Journal of Power Sources*, 2014, **264**, 235-239.

201.   S. W. Kim, D. H. Seo, X. H. Ma, G. Ceder and K. Kang, *Adv Energy Mater*, 2012, **2**, 710-721.

202.   S. Komaba, C. Takei, T. Nakayama, A. Ogata and N. Yabuuchi, *Electrochemistry Communications*, 2010, **12**, 355-358.

203.   S. Komaba, T. Nakayama, A. Ogata, T. Shimizu, C. Takei, S. Takada, A. Hokura and I. Nakai, *ECS Transactions*, 2009, **16**, 43-55.

204.   S. Komaba, N. Yabuuchi, T. Nakayama, A. Ogata, T. Ishikawa and I. Nakai, *Inorganic Chemistry*, 2012, **51**, 6211–6220.

205.   D. Kim, E. Lee, M. Slater, W. Lu, S. Rood and C. S. Johnson, *Electrochemistry Communications*, 2012, **18**, 66-69.

206. M. Sathiya, K. Hemalatha, K. Ramesha, J.-M. Tarascon and A. S. Prakash, *Chem Mater*, 2012, **24**, 1846–1853.

207. M. Ati, L. Dupont, N. Recham, J. N. Chotard, W. T. Walker, C. Davoisne, P. Barpanda, V. Sarou-Kanian, M. Armand and J. M. Tarascon, *Chem Mater*, 2010, **22**, 4062-4068.

208. Y. Gao and J. R. Dahn, *Journal of the Electrochemical Society*, 1996, **143**, 100-114.

209. J. S. Kim, C. S. Johnson, J. T. Vaughey, M. M. Thackeray and S. A. Hackney, *Chem Mater*, 2004, **16**, 1996-2006.

210. N. Yabuuchi, K. Yoshii, S. T. Myung, I. Nakai and S. Komaba, *Journal of the American Chemical Society*, 2011, **133**, 4404-4419.

211. H. Liu, C. R. Fell, K. An, L. Cai and Y. S. Meng, *Journal of Power Sources*, 2013, **240**, 772-778.

212. M. Newville, *Journal of Synchrotron Radiation*, 2001, **8**, 322-324.

213. B. Ravel and M. Newville, *Journal of Synchrotron Radiation*, 2005, **12**, 537-541.

214. J. Rodriguez-Carvajal, *Physica B*, 1993, **192**, 55-69.

215. R. Kataoka, T. Mukai, A. Yoshizawa and T. Sakai, *Journal of The Electrochemical Society*, 2013, **160**, A933-A939.

216. J. M. Tarascon and M. Armand, *Nature*, 2001, **414**, 359-367.

217. J. B. Goodenough and Y. Kim, *Chemistry of Materials*, 2010, **22**.

218. B. L. Ellis, K. T. Lee and L. F. Nazar, *Chem Mater*, 2010, **22**, 691-714.

219. B. Xu, C. R. Fell, M. Chi and Y. S. Meng, *Energy & Environmental Science*, 2011, **4**.

220. L. Haodong, C. R. Fell, A. Ke, C. Lu and Y. S. Meng, *Journal of Power Sources*, 2013, **240**, 772-778.

221. B. H. Qu, C. Z. Ma, G. Ji, C. H. Xu, J. Xu, Y. S. Meng, T. H. Wang and J. Y. Lee, *Advanced Materials*, 2014, **26**, 3854-3859.

222. N. Yabuuchi, M. Kajiyama, J. Iwatate, H. Nishikawa, S. Hitomi, R. Okuyama, R. Usui, Y. Yamada and S. Komaba, *Nature Materials*, 2012, **11**, 512-517.

223. N. Yabuuchi, M. Yano, H. Yoshida, S. Kuze and S. Komaba, *Journal of the Electrochemical Society*, 2013, **160**, A3131-A3137.

224. N. Yabuuchi, M. Kajiyama, J. Iwatate, H. Nishikawa, S. Hitomi, R. Okuyama, R. Usui, Y. Yamada and S. Komaba, *Nature Materials*, 2012, **11**, 512–517.

225. D. Kim, E. Lee, M. Slater, W. Q. Lu, S. Rood and C. S. Johnson, *Electrochemistry Communications*, 2012, **18**, 66-69.

226. D. Kim, S.-H. Kang, M. Slater, S. Rood, J. T. Vaughey, N. Karan, M. Balasubramanian and C. S. Johnson, *Advanced Energy Materials*, 2011, **1**, 333-336.

227. X. F. Wang, M. Tamaru, M. Okubo and A. Yamada, *J Phys Chem C*, 2013, **117**, 15545-15551.

228. P. Barpanda, G. Liu, C. D. Ling, M. Tamaru, M. Avdeev, S.-C. Chung, Y. Yamada and A. Yamada, *Chemistry of Materials*, 2013, **25**, 3480-3487.

229. P. Barpanda, J. Lu, T. Ye, M. Kajiyama, S.-C. Chung, N. Yabuuchi, S. Komaba and A. Yamada, *Rsc Advances*, 2013, **3**, 3857-3860.

230. P. Barpanda, T. Ye, S. Nishimura, S. C. Chung, Y. Yamada, M. Okubo, H. S. Zhou and A. Yamada, *Electrochemistry Communications*, 2012, **24**, 116-119.

231. K. H. Ha, S. H. Woo, D. Mok, N. S. Choi, Y. Park, S. M. Oh, Y. Kim, J. Kim, J. Lee, L. F. Nazar and K. T. Lee, *Advanced Energy Materials*, 2013, **3**, 770-776.

232. K. Saravanan, C. W. Mason, A. Rudola, K. H. Wong and P. Balaya, *Advanced Energy Materials*, 2012.

233. J. Y. Jang, H. Kim, Y. Lee, K. T. Lee, K. Kang and N.-S. Choi, *Electrochemistry Communications*, 2014, **44**, 74-77.

234. H. Kim, Y.-U. Park, K.-Y. Park, H.-D. Lim, J. Hong and K. Kang, *Nano Energy*, 2014, **4**, 97-104.

235. Y. U. Park, D. H. Seo, H. S. Kwon, B. Kim, J. Kim, H. Kim, I. Kim, H. I. Yoo and K. Kang, *Journal of the American Chemical Society*, 2013, **135**, 13870-13878.

236. H. Kim, I. Park, S. Lee, H. Kim, K.-Y. Park, Y.-U. Park, H. Kim, J. Kim, H.-D. Lim, W.-S. Yoon and K. Kang, *Chemistry of Materials*, 2013, **25**, 3614-3622.

237. H. Kim, I. Park, D. H. Seo, S. Lee, S. W. Kim, W. J. Kwon, Y. U. Park, C. S. Kim, S. Jeon and K. Kang, *Journal of the American Chemical Society*, 2012, **134**, 10369-10372.

238. K. Saravanan, C. W. Mason, A. Rudola, K. H. Wong and P. Balaya, *Advanced Energy Materials*, 2013, **3**, 444-450.

239. H. Yoshida, N. Yabuuchi and S. Komaba, *Electrochemistry Communications*, 2013, **34**, 60-63.

240. N. Yabuuchi, R. Hara, K. Kubota, J. Paulsen, S. Kumakura and S. Komaba, *Journal of Materials Chemistry A*, 2014, **2**, 16851-16855.

241. J. Billaud, G. Singh, A. R. Armstrong, E. Gonzalo, V. Roddatis, M. Armand, T. Rojo and P. G. Bruce, *Energy & Environmental Science*, 2014, **7**, 1387-1391.

242. R. Berthelot, D. Carlier and C. Delmas, *Nat Mater*, 2011, **10**, 74-U73.

243. J. Zhao, J. Xu, D. H. Lee, N. Dimov, Y. S. Meng and S. Okada, *Journal of Power Sources*, 2014, **264**, 235-239.

244. X. H. Wua, J. H. Guo, D. W. Wang, G. M. Zhong, M. J. McDonald and Y. Yang, *Journal of Power Sources*, 2015, **281**, 18-26.

245. D. Buchholz, C. Vaalma, L. G. Chagas and S. Passerini, *Journal of Power Sources*, 2015, **282**, 581-585.

246. J. Xu, D. H. Lee and Y. S. Meng, *Funct Mater Lett*, 2013, **6**, 1330001.

247. S. Komaba, N. Yabuuchi, T. Nakayama, A. Ogata, T. Ishikawa and I. Nakai, *Inorganic Chemistry*, 2012, **51**, 6211-6220.

248. J. Xu, D. H. Lee, R. J. Clement, X. Q. Yu, M. Leskes, A. J. Pell, G. Pintacuda, X. Q. Yang, C. P. Grey and Y. S. Meng, *Chem Mater*, 2014, **26**, 1260-1269.

249. N. Yabuuchi, R. Hara, M. Kajiyama, K. Kubota, T. Ishigaki, A. Hoshikawa and S. Komaba, *Adv Energy Mater*, 2014, **4**, 1301453.

250. B. Xu, C. R. Fell, M. F. Chi and Y. S. Meng, *Energ Environ Sci*, 2011, **4**, 2223-2233.

251. H. D. Liu, C. R. Fell, K. An, L. Cai and Y. S. Meng, *Journal of Power Sources*, 2013, **240**, 772-778.